Optical Spectroscopy of Molten Fluorides: Methods, Electronic and Vibrational Data,

Structural Interpretation, and Relevance to Radiative Heat Transfer

William B. Derdeyn, Sara Mastromarino, Ruchi Gakhar, Mark H. Anderson, Mikhail A. Kats, Raluca O.

Scarlat

ABSTRACT

To help address the need for predicting radiative heat transfer (RHT) behavior of molten salts, we

conducted a comprehensive review of methods and data from infrared optical spectroscopic measurements

on molten fluoride salts. Transmittance, reflectance, and trans-reflectance experimental methods are

discussed, along with the corresponding data reduction methodology and the limitations of each technique.

Optical spectroscopy is a convenient indirect probe for changes in structural parameters with temperature

and composition. Electronic and vibrational absorption data for transition-metal, lanthanide, and actinide

solutes and vibrational absorption data for alkali and alkaline earth fluoride solvents are compiled, and the

corresponding structural interpretation is discussed and compared with other experimental and theoretical

work. We find that solvent and solute vibrational absorption can be significant in the mid-infrared, resulting

in near-infrared edges of significance to RHT. Extrapolation and averaging of existing edge data leads to

estimated gray absorption coefficient values at 700 °C of 546 m<sup>-1</sup> for FLiBe and 276 m<sup>-1</sup> for FLiNaK, both

within the range of  $1-6000 \,\mathrm{m}^{-1}$  identified to be of engineering relevance for radiative heat transfer analysis.

**Keywords:** molten salt, infrared optical spectroscopy, molecular structure, radiative heat transfer

**ACRONYMS** 

ARE Aircraft Reactor Experiment

MSRE Molten Salt Reactor Experiment

MSBR Molten Salt Breeder Reactor

MSR molten salt reactor

FHR fluoride-salt-cooled, high-temperature reactor

CN coordination number

EM electromagnetic

KK Kramers-Kronig relations

CO classical oscillator method

UV ultraviolet

NIR near infrared

1|82

MIR mid infrared

FIR far infrared

NMR nuclear magnetic resonance

ORNL Oak Ridge National Laboratory

RHT radiative heat transfer

SINAP Shanghai Institute of Applied Physics

FTS Fourier transform spectrometer

MD molecular dynamics

AIMD ab-initio molecular dynamics

XRD x-ray diffraction

EXAFS extended x-ray absorption fine structure

HT-NMR high temperature nuclear magnetic resonance

HT-PFG-NMR high temperature pulsed field gradient nuclear magnetic resonance

QC-DFT quantum-chemical density-functional-theory

### NOMENCLATURE

 $\lambda$  = wavelength

v = spectroscopic wavenumber

 $\omega$  = angular frequency

T = temperature

I = light intensity

R = reflectance

T = transmittance

Abs = absorptivity

 $\epsilon$  = emissivity

 $\tilde{r}$  = complex EM-field reflectance

r = magnitude of EM-field reflectance

 $\tilde{n}_i$  = complex refractive index of medium i

n = real part of the complex refractive index, i.e., the refractive index

k = imaginary part of the complex refractive index, i.e., the extinction coefficient

 $\kappa_{\lambda}$  = spectral linear absorption coefficient

 $\kappa$  = gray linear absorption coefficient

s = distance traveled by light

A = absorbance

```
\varepsilon = molar absorptivity
```

c = molar concentration

 $\bar{\theta}$  = frequency-dependent phase shift of reflected EM wave

 $\tilde{\epsilon}_r$ = complex relative permittivity

 $\epsilon_r'$  = real component of the complex permittivity

 $\epsilon_r^{\prime\prime}$  = imaginary component of complex permittivity

 $\epsilon_{r,\infty}$  = high-frequency limit of permittivity

 $v_i$  = wavenumber of the *j*th resonance

 $4\pi\rho_i$  = strength of the *j*th resonance

 $\gamma_i$  = damping factor of the *j*th resonance

 $\mu_r$  = magnetic permeability

 $\theta$  = angle of light propagation

h =salt height (related to the trans-reflectance method)

### 1. Introduction

Molten-fluoride salts are currently under investigation in support of several proposed molten salt nuclear reactor (MSR) designs [1]. Historically, molten fluorides saw considerable use in the Aircraft Reactor Experiment (ARE) and Molten Salt Reactor Experiment (MSRE), two test reactors built and operated at Oak Ridge National Laboratory (ORNL) during the 1950s and 60s. The ARE used NaF-ZrF<sub>4</sub>-UF<sub>4</sub> (53-41-6 mol%) fuel salt at steady state temperatures up to 860 °C and ran at up to 2.5 MWth for a total of 241 hours [2]. Following successful operation of the ARE, the MSRE ran at up to 8 MWth for over 15,000 hours and used LiF-BeF<sub>2</sub>-ZrF<sub>4</sub>-UF<sub>4</sub> (65-29-5-1 mol%) fuel salt at steady state temperatures up to 650 °C, along with 2LiF-BeF<sub>2</sub> (FLiBe) as secondary coolant [3][4]. The Molten Salt Breeder Reactor (MSBR), the larger scale follow-up to the MSRE, proposed to run at 1000 MWe and use LiF-BeF<sub>2</sub>-ThF<sub>4</sub>-UF<sub>4</sub> (72-16-12-0.4 mol%) fuel salt, along with NaF-NaBF<sub>4</sub> (8-92 mol%) secondary coolant [5]. Unfortunately, the MSBR program was cut short before the reactor could be built. However, there has been renewed interest in the commercialization of MSRs and the sub-class fluoride-salt-cooled, high-temperature reactors (FHRs) [6][7] and the use of fluorides for fusion reactors and concentrated solar power [8].

MSRs and FHRs are typically designed to operate between 500 and 700 °C; hence, reactor designers must consider RHT for prediction of steady state and transient reactor performance. Participating medium effects, wherein the fluid absorbs and re-emits radiant energy in exchange with itself and any surrounding surfaces, often govern the relative contribution of RHT to the total heat transfer in the reactor. These effects have been investigated through several computational fluid dynamics simulations [9][10] and RHT models

[11][12]. The degree to which overall heat transfer is enhanced was found highly sensitive to the gray linear absorption coefficient,  $\kappa$ , which determines the amount of light absorbed and re-emitted along a given direction per unit length (m<sup>-1</sup> units). RHT is significant when the nondimensional product of pipe diameter and  $\kappa$  is in the range of 0.1 to 60 [10]. For example, for a one-centimeter heat-exchanger tube diameter,  $\kappa$  of 10 to 6000 m<sup>-1</sup> would lead to significant RHT effects; for a ten-centimeter heat-exchanger tube diameter,  $\kappa$  of 1 to 600 m<sup>-1</sup> would lead to significant RHT effects.

Molten salt heat transfer models that capture RHT typically use gray  $\kappa$ , meaning that  $\kappa$  is assumed to be constant over all wavelengths, to avoid the high computational cost of spectrally resolved calculations [13]. In reality, the linear absorption coefficient has a spectral dependence,  $\kappa_{\lambda}(\lambda)$ , which introduces the challenge of picking a single or banded gray  $\kappa$  that adequately captures the RHT behavior. There is limited  $\kappa_{\lambda}$  data for proposed molten-fluoride coolants and fuel (e.g., FLiBe, FLiNaK) or for solute species that could be introduced via corrosion or fuel leakage or are part of the fuel in the case of MSRs, thus it is difficult to ascertain if the use of gray  $\kappa$  is acceptable for RHT-modeling in fluoride salts.

At the expected temperature ranges of MSRs and FHRs, absorption in the near-infrared (NIR) and midinfrared (MIR) ranges will be most important, as shown in Figure 1. We predict RHT-relevance by plotting the Planck distribution in wavelength (Figure 1), here calculated for a temperature of 700 °C and showing a peak at 3 µm. The distribution increases in intensity and shifts to shorter wavelengths as temperature increases.

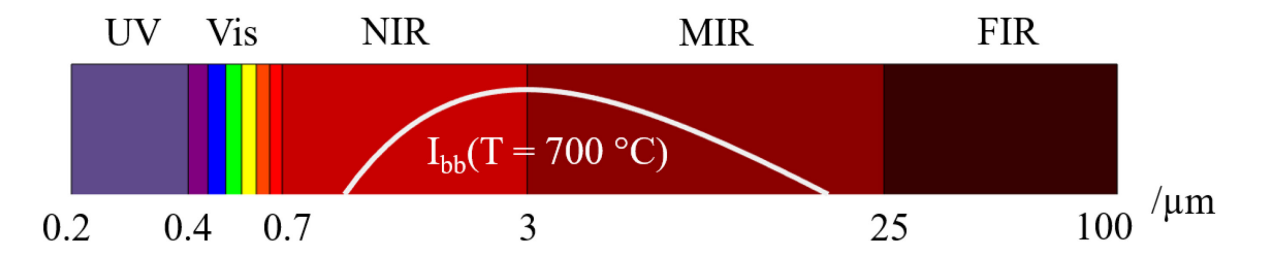


Figure 1. Portion of electromagnetic spectrum covered by studies in this review. The following regions are defined: ultraviolet (UV), visible (Vis), near-infrared (NIR), mid-infrared (MIR), and far-infrared (FIR). Planck distribution in wavelength at  $T = 700^{\circ}$ C is plotted in white on a logarithmic wavelength scale. The lower limit of the y-axis scale has been chosen such that the displayed portion of the Planck distribution makes up 97% of the total blackbody power at  $T = 700^{\circ}$ C.

We refer to measurement of absorption spectra within the overall range depicted in Figure 1 as optical absorption spectroscopy. In the ultra-violet (UV), visible, and NIR, absorption mostly occurs due to excitation of valence electrons, referred to as electronic absorption. In the NIR, MIR and far-infrared (FIR), absorption may also occur due to excitation of molecular vibrations, referred to as vibrational absorption. The various available electronic and vibrational energy levels will result in a unique spectrum for a given

solute-solvent combination. Spectroscopists typically compare results with complementary methods to infer structural information, such as the coordination number (CN) [14]. Despite offering this useful information, optical absorption spectroscopy has been somewhat overlooked in molten-salt chemistry in recent years. Rollet and Salanne comprehensively reviewed molten halide structure, focusing on several computational and experimental methods, but rarely mention optical absorption spectroscopy (though we note that Raman spectroscopy receives considerable attention) [15].

We determined that a review of molten-fluoride optical absorption spectroscopy could encourage investigation by providing a database of methods and results and offering a discussion of structural interpretations. Several excellent reviews exist for the broader field of molten-salt optical spectroscopy [16][17][18], mostly involving nitrates and chlorides. These articles are useful for general best-practices and theoretical background of spectroscopic methods, but there is limited information regarding fluorides. The closest to a molten-fluoride review is Toth's ORNL report, 'Containers for Molten Fluoride Spectroscopy' [19]. Toth concluded that for 'optically pure' fluorides, SiO<sub>2</sub> would be an acceptable container, but that a metal cell with diamond windows would be the most robust. The report rarely mentions reflectance setups, and there is no summary or discussion of absorption data.

As such, we conducted a comprehensive search of molten-fluoride methods and data. After providing a brief background on the relevant optics concepts, we present and discuss the spectroscopy methods, dividing them by transmittance (3.1) and reflectance techniques (3.2). Detailed information on the methods is compiled in Table 1 (transmittance) and Table 4 (reflectance), and we give each setup an index (T# for transmittance, R# for reflectance) that we use to refer to throughout the text. We then present the data as a collection of digitized spectra, given in Figure 4, and give each plot an index (A#) that we refer to throughout the text. Each spectra is given an index (V# for vibrational, E# for electronic), and we summarize in Table 5 (solvent vibrational edge), Table 6 (solvent and solute vibrational resonance), Table 7 (lighter solute electronic), and Table 8 (heavier solute electronic), listing the various peak locations and intensities and deduced speciation. Next, we discuss the structural interpretation of the data and compare with more recent data from complementary methods, dividing into vibrational (5.1) and electronic (5.2) absorption. Lastly, we summarize our discussion of structural interpretation from the available spectra of solvents and solutes and point out consequences of the NIR data on RHT, identifying the relatively small set of compositions that have been studied, and highlighting key gaps in speciation in molten fluorides that could potentially be closed with further measurements. Due to the experimental difficulty of optical absorption spectroscopy measurements on high-temperature melts, the in-depth description and discussion of the experimental set-ups describe the state of the art of what has been achieved thus far, and highlight the more promising directions for experimental set-ups.

#### 2. OPTICS BACKGROUND AND TERMINOLOGY

#### 2.1. Measurable Parameters

We define the following measurable optical parameters: transmittance,  $T(\lambda,T) = I_t(\lambda,T)/I_i(\lambda,T)$ , reflectance,  $R(\lambda,T) = I_r(\lambda,T)/I_i(\lambda,T)$ , absorptivity,  $Abs(\lambda,T) = I_a(\lambda,T)/I_i(\lambda,T)$ , and emissivity,  $\epsilon(\lambda,T) = I_e(\lambda,T)/I_{bb}(\lambda,T)$  of a molten salt sample at temperature T. I is the light intensity. The subscript i refers to light incident on the sample, the subscript t refers to light transmitted by the sample, the subscript t refers to light absorbed by the sample, the subscript t refers to light emitted by the sample, and the subscript t refers to a blackbody at temperature t. In this manuscript we assume non-scattering surfaces and media because, in the studies we found, salt-gas and salt-window interfaces could be assumed to be optically flat, and the presence of suspended particles was avoided.

For a semi-transparent sample,  $1 = R(\lambda, T) + \mathcal{T}(\lambda, T) + Abs(\lambda, T)$ , and for an opaque sample,  $1 = R(\lambda, T) + Abs(\lambda, T)$ . For a reciprocal sample at thermal equilibrium,  $\epsilon(\lambda, T) = Abs(\lambda, T)$ , and through substitution the previous equations become  $1 = R(\lambda, T) + \mathcal{T}(\lambda, T) + \epsilon(\lambda, T)$  and  $1 = R(\lambda, T) + \epsilon(\lambda, T)$ .

# 2.2. Optical Properties of Materials

We define the complex refractive index of a given medium,  $\tilde{n}$ .

$$\tilde{n} = n + ik$$

The real component, n, sometimes simply referred to as the refractive index, determines the speed at which electromagnetic (EM) waves propagate through the material. The imaginary component, k, also known as the extinction coefficient, determines the rate at which the EM fields lose strength due to absorption. The spectral linear absorption coefficient, which captures the loss of optical intensity as light propagates, is  $\kappa_{\lambda} = 4\pi k/\lambda$ . We note that our notation for  $\kappa_{\lambda}$  follows that of RHT literature, rather than in optics (where it would be the extinction coefficient).

At the interface between two media with complex refractive indices,  $\tilde{n}_1$  and  $\tilde{n}_2$ , the reflectance at normal incidence is given by:

$$R = \left| \frac{\tilde{n}_1 - \tilde{n}_2}{\tilde{n}_1 + \tilde{n}_2} \right|^2$$

Within a given medium, the transmittance of light across a distance s is given by:

$$T = e^{-\kappa_{\lambda} s}$$

Equations 2 and 3 are the basis of methods for obtaining  $\kappa_{\lambda}$  from measurement of R or T of a molten fluoride sample.

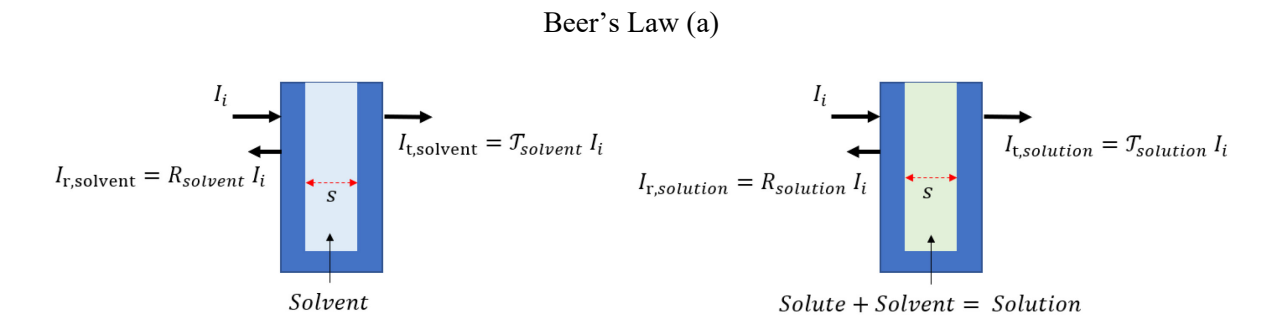
#### 3. EXPERIMENTAL METHODS

Here, we compile and summarize the experimental setups for molten fluoride transmittance and reflectance measurements. We discuss the advantages and disadvantages of the various setups and provide recommendations for future designs. Molten fluoride transmittance and reflectance setups are relatively distinct in design; hence, they are treated separately in sections 3.1 (transmittance method) and 3.2 (reflectance method).

### 3.1. Transmittance

# 3.1.1. Background

First, we outline two techniques that are used to extract  $\kappa_{\lambda}$  or the molar absorptivity,  $\varepsilon$ , via measurement of transmittance. We describe Beer's Law in section 3.1.1.1, typically used to obtain  $\varepsilon$  of a solute species. In section 3.1.1.2, we describe a method wherein transmittance measurements are performed at two or more path lengths, typically used to obtain  $\kappa_{\lambda}$  of a solvent species.



Double-path-length method (b)

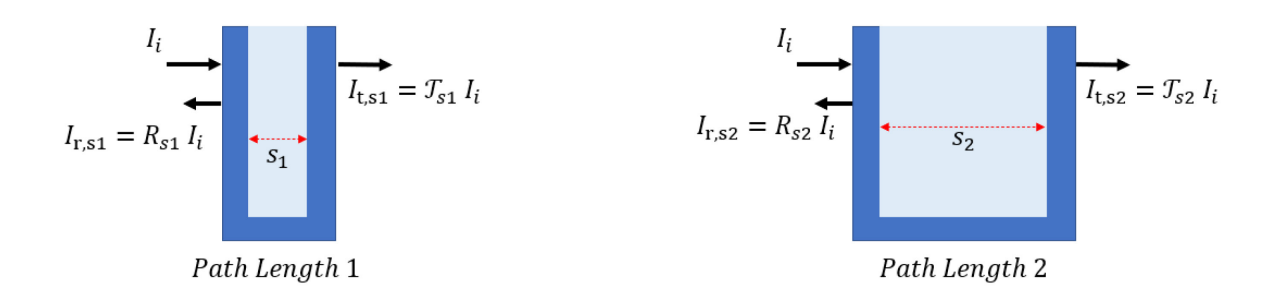


Figure 2. Schematics for (a) Beer's Law and (b) double-path-length transmittance measurement methods.

#### 3.1.1.1. Beer's Law

We give Beer's Law in equation 4.

$$A_i = \varepsilon_i c_i s$$

Here, A is the absorbance,  $\varepsilon$  is the molar absorptivity (units of M<sup>-1</sup>cm<sup>-1</sup>), c is the concentration (units of M), and s is the distance traveled by light, a.k.a. the path length (units of cm). The subscript i refers to species i. Beer's law shows that in the dilute concentration limit, the absorbance of a species will increase linearly with its concentration; however, deviations from linearity occur at higher concentrations and for highly absorbing species [20]. The spectral linear absorption coefficient,  $\kappa_{\lambda}$ , is related to molar absorptivity,  $\varepsilon$ , by:  $\kappa_{\lambda} = \varepsilon c \ln(10)$ . Absorbance, A, is related to transmittance, T, by:  $A = -\log_{10} T$ . The overall absorbance of a solution consisting of a solvent and a single solute is given by:  $A_{solution} = A_{solvent} + A_{solute}$ . Here,  $A_{solution}$  is the absorbance of the solution consisting of a single solute within a solvent,  $A_{solvent}$  is the absorbance of just the solvent, and  $A_{solute}$  is the absorbance of just the solute. Hence, to obtain the molar absorptivity of a given solute,  $\varepsilon_{solute}$ , one must measure  $A_{solvent}$ ,  $A_{solute}$ , and the solute concentration  $c_{solute}$ . Typically, this procedure is performed over a range of concentrations to show that the measurements are within the dilute limit.

Almost all the molten-fluoride transmittance (T1-13, T15-17) and several reflectance (R5, R7) studies we review used the Beer's law method.

### 3.1.1.2. Double-Path-Length Method

The standard approach for measuring  $\kappa_{\lambda}$  of a solvent species is to perform two transmittance measurements with different path lengths [21][22], a method we refer to as the double-path-length method. The ratios of the transmittances are used to calculate  $\kappa_{\lambda}$  via equations 5 and 6.

$$\frac{T_{S1}}{T_{S2}} = \frac{I_{t,S1}}{I_{t,S2}}$$

$$\kappa_{\lambda} = \frac{1}{s2 - s1} \ln \left[ \frac{T_{s1}}{T_{s2}} \right]$$

Where, s1 and s2 are the path lengths of the two measurements. The path lengths can either be measured individually or the path length difference can be measured.

Only one molten-fluoride transmittance setup (T14) has used the double-path-length method, but we also include a molten-glass reflectance setup (R6) that would be compatible with molten fluorides. We note that Coyle adapted a chloride and nitrate setup for fluorides by replacing the concentric quartz cuvettes with Inconel tubes capped by diamond windows, however the setup has not been tested with fluorides yet [13].

# 3.1.2. Compilation of transmittance setups

Table 1 lists the transmittance setups covered in this review. For clarity, the setups have been defined by each unique combination of cell, furnace and optical path. In the first column, we include the setup index (T#), primary author and reference, year of publication, and data-processing method (i.e., Beer's Law or double-path-length method). The second column provides schematics and equipment details (i.e., furnace, cell, optical path, cover gas). The third column lists parameters such as wavelength range, maximum  $\kappa_{\lambda}$  measured, maximum temperature, path length, optical window used, amount of salt required, and reported uncertainty. The next columns provide details on the studies performed, such as the salt compositions used, and provides references to relevant plots (A#) and spectra indices (E#/V#).

Table 1. Experimental setups for measurement of  $\kappa_{\lambda}$  via transmittance. If unspecified, sample size was estimated using dimensions from the schematics and assuming the optical path to be completely filled with salt.

Experimental Set-up	Schematic and Equipment Details	Parameters	Studies Performed		
			Salt (	Composition	D (
			Solute	Solvent	Data
T1 Young [23] 1959 Beer's Law	Furnace: Pt-wrapped quartz plates in Lavite block, contained in Cu assembly Cell: Pt pendent drop (shown in bottom image) Optics: Cary 14M grating spectrometer, sample compartment Cover gas: Ar Reprinted with permission from [23]. Copyright 1959 American Chemical Society.	Wavelength: $0.3-1.4  \mu m$ $\kappa_{\lambda}$ :NR  Path Length: $\sim 8-10  mm$ Temperature: $780  ^{\circ}C$ Window: None  Uncertainty: NR  Sample Size: $\sim 0.7  \mathrm{g}$	CoF <sub>2</sub> CrF <sub>3</sub> PrF <sub>3</sub> UF <sub>4</sub> UO <sub>2</sub> F <sub>2</sub>	FLiNaK	A2 E1 A3 E2 A4 E30 A5 E31 A6 E32 [24]

T2 Young [23] 1959 Beer's Law	Furnace: T1 Cell: MgO cuvette (shown in schematic) Optics: Cary 14M grating spectrometer, sample compartment Cover gas: Ar Reprinted with permission from [23]. Copyright 1959 American Chemical Society.	Wavelength: $0.3-0.7  \mu m$ $\kappa_{\lambda}$ : NR  Path Length: 5 mm  Temperature: $780  ^{\circ}\text{C}$ Window: MgO  Uncertainty: NR  Sample size: $\sim 1.4  \text{g}$	NiF2	FLiNaK	A1 E3 [24]
T3 Young [25] 1964 Beer's Law	Furnace: T1 Cell: Windowless Cu or Pt tube (cross sectional schematic above, and image below) Optics: Cary 14M grating spectrometer, sample compartment Cover gas: Ar Reprinted with permission from [25]. Copyright 1964 American Chemical Society.	Wavelength: $0.3-2~\mu m$ $\kappa_{\lambda}$ : NR  Path Length: $\sim 8~mm$ Temperature: $525~^{\circ}C$ Window: None  Uncertainty: $10\%$ Sample size: $\sim 1.5~g$	NiF2	FLiNaK	A7 E4 [26]

Young [27][28]  1967  Beer's Law  Furnace: Vacuum-tight inverted Ni tee inside of Ni block with 12 heater rods, contained within sealed assembly (shown in image) Cell: T3, 0.25" OD Cu and graphite (w/o keeper holes) Optics: Cary 14M grating spectrometer, sample compartment Cover gas: He Copyright of US government.		UF4 UF3 NiF2 FeF2 CrF2 CrF3	FLiBe, FLiNaK	A8 E33 A9 E33 A10 E34-35 A11 E34-35 [27] A13 E5 A14 E6 A15 E7 A16 E8 [29]
---	--	--	---------------	--

T5 Young [30] 1969 Beer's Law	Furnace: T4 Cell: T3, Cu (size not specified) Optics: Cary 14H grating spectrometer inside of hot cell with optical feedthroughts (Shown in schematic) Cover gas: He Copyright of US government.	Wavelength: $0.2-2.1~\mu m$ $\kappa_{\lambda}$ : NR  Path Length: NR  Temperature: $575~^{\circ}C$ Window: None  Uncertainty: $10\%$	PaF <sub>4</sub>	Solvent: LiF-BeF <sub>2</sub> -ThF <sub>4</sub> (72-16-12 mol%)	A17 E37 A18 E37 [31]
T6 Young [33] 1972 Beer's Law	Furnace: Heating-wire-wrapped BN tube contained within sealed metal tube (shown in right of image) Cell: Ni body with Au-sealed LaF3 windows (shown in left of image) Optics: no details given Cover gas: Ar or vacuum Copyright of US government.	Wavelength: $2.6-3.8$ $\kappa_{\lambda}$ : NR  Path Length: NR  Temperature: $450^{\circ}\text{C}$ Window: $\text{LaF}_3$ Uncertainty: NR  Sample size: NR	$D_3BO_3$	NaBF4	[34]

T7 Whiting [35] 1973 Beer's Law	Furnace: T4 Cell: Modified 0.375" OD hard carbon, graphite, or Ni windowless (T3) with electrodes inserted through BN plugs at bottom or lowered directly through beam path Optics: Cary 14M grating spectrometer, sample compartment Cover gas: He	Wavelength: $0.2-2~\mu m$ $\kappa_{\lambda}$ : NR Path Length: NR Temperature: $540~^{\circ}C$ Window: None Uncertainty: NR Sample size: $\sim 4~g$	UF4 UF3 MnF3 MnF2 CuF2	LiF-BeF <sub>2</sub> -ZrF <sub>4</sub> (66:29:5 mol%)	A12 E36 [36] A23 E14 A24 E15 A25 E16 [35]
T8 Bamberger [37] 1968 Beer's Law	Furnace: T4 Cell: silica tube Optics: Cary 14M grating spectrometer, sample compartment Cover gas: SiF4	Wavelength: 0.64, 1.09 μm  κ <sub>λ</sub> : NR  Path Length: NR  Temperature: 698 °C  Window: Silica  Uncertainty: 5%  Sample size: NR	UF4	FLiBe	E38-41 [37]

		1	1	1	,
T9 Bamberger [38] 1974 Beer's Law	Furnace: T4 Cell: 10 mm ID silica tube Optics: Cary 14M grating spectrometer, sample compartment Cover gas: NR	Wavelength: $0.25-0.7  \mu m$ $\kappa_{\lambda}$ : NR  Path length: 10 mm  Temperature: $600  ^{\circ}\text{C}$ Window: Silica  Uncertainty: NR  Sample size: $^{\sim}3  \text{g}$ Wavelength:	Te <sub>2</sub> LiTe <sub>3</sub> Li <sub>2</sub> Te + oxidants	FLiBe	A20 E9-10 [38]
T10 Whiting [39] 1972 Beer's Law	Furnace: T4 Cell: 10 mm path length rectangular quartz cell Optics: Cary 14M grating spectrometer, sample compartment Cover gas: He	Wavelength: $0.2 - 2 \mu m$ $\kappa_{\lambda}$ : NR Path length: 10 mm Temperature: 500 °C Window: Quartz Uncertainty: NR Sample size: 4 g	NaO <sub>2</sub> K <sub>2</sub> CrO <sub>4</sub> KNO <sub>2</sub>	FLiNaK	A21 E11 A22 E12 E13 [40][39]
T11 Bates [41] 1972 Beer's Law	Furnace: T4 Cell: 2mm path length silica cell Optics: Perkin-Elmer model 621 grating spectrometer, sample compartment Cover gas: NR	Wavelength: $\sim 3.72  \mu m$ $\kappa_{\lambda}$ : NR  Path length: 2 mm  Temperature: $425  ^{\circ}\text{C}$ Window: Silica  Uncertainty: NR  Sample size: NR	D <sub>3</sub> BO <sub>3</sub>	NaBF4	A26 V69 [41]

T12 Toth [42] 1969 Beer's Law	Furnace: T4 Cell: Type ATJ graphite body with un-sealed diamond windows Optics: Cary 14H grating spectrometer, sample compartment Cover gas: He Reprinted with permission from [42]. Copyright 1969 American Chemical Society.	Wavelength: $0.2 - 2.5 \mu m$ $\kappa_{\lambda}$ : NR Path Length: $6.35 \text{ mm}$ Temperature: $690 ^{\circ}\text{C}$ Window: Diamond Type IIa Uncertainty: NR Sample size: $\sim 2 \text{ g}$	NiF2 UF4 UF4 UF4 UF3	FLiBe  FLiNaK FLiBe LiF-BeF2 (48-52 mol%)	A27 E17 A28 E43 [42] A29 E44 A30 E45-46 A31 E47-48 [14]
T13 Toth [44] [45] 1973 Beer's Law	Furnace: Cylindrical inconel block with ring of heater rods, contained within sealed Cu assembly (schematic shown above from [45]) Cell: T12, modififed to include either Pt stirring loop [44] or Pt-10%Rh sparger tube [46] could be inserted into cell Optics: Cary 14H grating spectrometer, sample compartment Cover gas: He Reprinted with permission from [44]. Copyright 1973 American Chemical Society.	Wavelength: $0.3-2.5  \mu m$ $\kappa_{\lambda}$ : NR  Path Length: $6.35  mm$ Temperature: $800  ^{\circ}C$ Window: Diamond Type Iia  Uncertainty: NR  Sample size: $0.6  g$	UF4 UF3 NbF4 K2NbF7 UF4 UF3 HF H2	FLiBe LiF-BeF2 (48-52 mol%)  FLiBe LiF-BeF2 (48-52 mol%)  FLiBe LiF-BeF2 (48-52 mol%) LiF-BeF2 (57-43 mol%) LiF-BeF2-ThF4 (72-16-12 mol%)  FLiBe	A32 E49 A33 E49 A34 E50-52 [44]  A35 E18 [47]  E53 [46]

T14 Varlamov [49] 1989 Double-path-length method	Furnace: no details given Cell: windowless Pt plates or sapphire windows Optics: (1) Radiation source; (2) modulator; (3) rotating and focusing mirrors; (4) high temperature adapter windows; (5) holder with samples; (6) monochromator prism; (7) radiation detector Cover gas: Ar or He	Wavelength: $4-14 \mu m$ $\kappa_{\lambda}$ : $10-2000 \text{ m}^{-1}$ Path Length: NR  Temperature: $1527 \text{ K}$ Window: sapphire  Uncertainty: $10\%$ $(100-1000 \text{ m}^{-1})$ $20\%$ $(10 \text{ m}^{-1} > )$ Sample size: NR		LiF CaF <sub>2</sub> BaF <sub>2</sub>	A36 V1-6 A37 V7-15 A38 V16-23 [49]
T15 S. Liu [50] 2017 Beer's Law	Furnace: Aluminum oxide oven with beam path drilled out. Schematic shown above (a) Cell: Hastelloy C inverted tee with graphite-sealed windows. Schematics shown above (b,c) – BT: bolt, WP: window, EGR: graphite o-ring Optics: Perkin Elmer spectrometer (unspecified type) sample compartment Cover gas: Ar	Wavelength: $0.83 - 20  \mu m$ $\kappa_{\lambda}$ : NR  Path Length: $10  mm$ Temperature: $600  ^{\circ}C$ Window: Diamond, SiC  Uncertainty: NR  Sample size: $\sim 2.3  g$	LiOH	FLiBe	A39 V24, V70 A40 V24, V70 A41 V71 [50]

T16 H. Liu [51] 2018 Beer's Law	Furnace: Aluminum oxide oven with beam ports, directly coupled to glovebox with cell hoist assembly. Shown in schematic below Cell: T15, modified to include hole for gas sparging tube. Shown in schematic above Optics: QE Pro 65 grating spectrometer (Ocean Optics Co.) Deuterium-Tungsten lamp, DT-2000 (Hangzhou SPL Photonics Co.), focusing optics, and fiber optic cable. Shown in schematic below Cover gas: Ar	Wavelength: $0.2-1.0  \mu m$ $\kappa_{\lambda}$ : NR  Path Length: 10 mm  Temperature: 800 °C  Window: Diamond, SiC, Quartz, Sapphire, CaF <sub>2</sub> Uncertainty: NR  Sample size: ~2.3 g	UF <sub>4</sub>	FLiBe	A42 E54 [51]
T17 Y. Liu [52] 2020 Beer's Law	Furnace: T16 Cell: quartz cuvette Optics: T16, with Deuterium-Tungsten lamp, iDH2000 (ideaoptics) Cover gas: Ar	Wavelength: $0.2-0.9  \mu m$ $\kappa_{\lambda}$ : $250  m^{-1}$ Path Length: $10  mm$ Temperature: $600  ^{\circ}C$ Window: Quartz Uncertainty: NR Sample size: $3  g$	CrF <sub>2</sub> CrF <sub>3</sub>	FLiBe FLiNaK LiF-BeF <sub>2</sub> (69-31 mol%)	A43 E20-21 A44 E21-23 A45 E24-25 [52]

NR indicates the parameter was not reported

# 3.1.3. Discussion

# 3.1.3.1. Furnaces

Resistively heated furnaces have been ubiquitously used to reach the desired measurement 17|82

temperatures for molten fluoride transmittance setups. The first ORNL furnace consisted of a Lavite block with beam ports and a sample cavity heated by Pt-wound fused-silica plates (T1). The furnace was not vacuum-tight, and it was found that significant out-gassing would occur from the insulation or quartz heaters, which was detrimental to air-sensitive samples. Later ORNL furnaces (T4, T13) used metal blocks (typically Ni) with a cavity drilled out for the optical cell and light path, and several smaller holes drilled out for heater rods (i.e., cartridge heaters). The metal block was then situated within a larger, vacuum-tight metal enclosure with suitable optical windows and feedthroughs for the optical cell and heater. These vacuum-tight furnaces exhibited excellent spatial temperature uniformity, minimized contamination due to insulating materials and heater out-gassing, and could be held under vacuum or flushed with inert gas during operation. This was particularly important because the ORNL optical cells were not vacuum tight. Sealed quartz tubes or metal containers were used to transport samples from a glovebox to the furnace. After transport, vacuum was typically pulled on the furnace, followed by flushing of Ar or He.

Varlamov also used a vacuum-tight furnace (T14), though did not describe the heating element. Reports of SINAP setups (T15-17) did not give details on the heating element construction; thus, it is likely that commercial ceramic (aluminum oxide) ovens were used and modified to allow for beam ports and a hoist assembly for the optical cell. In the more recent studies (T16, T17), the oven was placed inside of a glovebox well with optical windows, eliminating the need to design a vacuum-tight furnace or cell.

### 3.1.3.2. Cells

The overall uncertainty of  $\kappa_{\lambda}$  derived from transmittance measurements is primarily determined by the uncertainty in the path-length measurement. Several optical cells were used by ORNL researchers, with increasing accuracy and repeatability of path length measurement with successive iterations. The first cell developed was the Pt pendent drop (T2), consisting of an open horizontal tube which would be dipped into the salt, for which the authors stated that the results should be considered qualitative because the path length was not well-repeatable between reference and sample measurements. The windowless cell (T3-5, T7), consisting of a vertical capsule with small holes drilled through horizontally, enabled much more repeatable measurements, resulting in an overall uncertainty of 10%. For the diamond-windowed graphite cell (T12-13), uncertainty was not reported; however, it can be assumed to have similar uncertainty as the silica cell setup of Bamberger (T8), which was reported to be 5%. Indeed, Toth reported UF<sub>4</sub> (in FLiBe) features in the 2  $\mu$ m region (Plot A28, E43) which had been previously unresolvable with the windowless cell (Plot A10, E33). This improved resolution enabled Toth to perform remarkable studies leading to better understanding of the coordination behavior of U<sup>4+</sup> complexes and detailed equilibria data for the U<sup>3+</sup>/U<sup>4+</sup> redox couple (further discussed in 5.2.3.2).

Varlamov used windowless Pt plates or sapphire windows to contain liquid fluoride samples, but

did not give further details or schematics (T14). SINAP researchers adapted Toth's diamond-windowed graphite cell, using instead a Hastelloy body sealed by elastic graphite gaskets (T15-16). Single-crystal SiC windows were used, in addition to diamond. The authors did not discuss their reasoning as to choosing Hastelloy versus graphite. Hastelloy has superior mechanical properties at high temperature, so it may have been chosen for better durability. Graphite is more chemically inert, but for a purified salt sample, Hastelloy (or other Ni-based alloys) would likely be acceptable. It might have been chosen for greater ease in achieving a vacuum-tight seal. Toth reported that molten fluorides do not wet to graphite or diamond; thus, a tight seal was not necessary to prevent leakage. Although not used for transmittance studies, Andersen's trans-reflectance cell design (R5) could be adapted to build a cell with a Ni or Au-lined Ni body with Ausealed diamond windows (further discussed in 3.2.3.2).

An intriguing possibility is the use of oxide (e.g., silica, MgO, sapphire, etc.) windows, which are more economical than diamond and have good durability at high temperature. ORNL researchers used silica or quartz cells in contact with telluride compounds in FLiBe (T9), several oxygen-containing species in FLiNaK (T10), and D<sub>3</sub>BO<sub>3</sub> in NaBF<sub>4</sub> (T11). Young used a MgO cell for NiF<sub>2</sub> in FLiNaK (T1), but reported incompatibility if UF<sub>4</sub> or ZrF<sub>4</sub> were present. Bamberger (T8) provided evidence for the stability of silica against attack by UF<sub>4</sub> in FLiBe by introducing highly toxic SiF<sub>4</sub> cover gas to limit this reaction (eq. 7).

$$UF_4 + SiO_2 \leftrightarrow UO_2 + SiF_4$$

Toth analyzed similar reactions of LiF and BeF<sub>2</sub> with various oxide windows (SiO<sub>2</sub>, Al<sub>2</sub>O<sub>3</sub>, and MgO) and found that most reactions were unfavorable. They hypothesized that dissolved oxides could attack silica to form silicates via the following reactions:

$$Li_2O + SiO_2 \leftrightarrow Li_2SiO_3$$

$$Li_2O + 2SiO_2 \leftrightarrow Li_2Si_2O_5$$

Experimentally, Toth reported a successful 5-hour corrosion test of FLiBe in quartz at 500 °C In conclusion, Toth stated that 'optically pure' (i.e. 'freed of alkali oxide, HF, H<sub>2</sub>O, and then filtered to remove suspended particles') fluoride melts 'behave surprisingly well in quartz under an atmosphere of helium' [19]. Liu et al provide some validation of this statement in their measurements of CrF<sub>2</sub> and CrF<sub>3</sub> in FLiBe and FLiNaK using quartz cuvettes (T17). The measurements were performed using pre-vacuum-dried, hydro-fluorinated solvents [53] (no mention of filtration) inside of a purified Ar glovebox (H<sub>2</sub>O and O<sub>2</sub> below 2 ppm). In summary, the use of oxide windows, in particular SiO<sub>2</sub>, is certainly possible, but more work is needed to understand their limitations.

We list the various window materials that have been used successfully with molten fluorides in Table 2. The usable wavelength ranges of each window have been estimated using either transmittance data directly from literature or by performing calculations using available optical property data. For the 19|82

$$\mathcal{T}_{overall} = (1 - R)^2 \cdot \mathcal{T}_{internal},$$

where, R is calculated using equation 2 and  $T_{internal}$  is calculated using equation 3. We take the cutoff wavelengths to be the value at which  $T_{overall}$  drops to about 0.65. Unless noted, the window thickness used to derive these ranges was 1 mm.

Table 2. Optical windows for use with molten fluorides.

Window material		Chemical compatibility with	Waveleng	th range (μm)
		molten fluorides	Minimum	Maximum
	Single-crystal		0.25	
	type IIa	No reports of corrosion	(0.5 mm thick)	>500 <sup>1,2</sup>
Diamond	турс на	[19][42] [50][51][54]	[55]	(0.490 mm thick)
Po	Polycrystalline	[17][42] [30][31][34]	0.35	[55]
	1 oryerystamme		[55]	
Single	e-crystal SiC	Limited use, but no reports of	0.4	5.0
Siligit	z-crystar Sic	corrosion [50][51]	[51]	[50]
Fu	sed SiO <sub>2</sub>	Inert if salt is purified, but	0.16*	4.0*
T u	3cd 510 <sub>2</sub>	susceptible to corrosion in the	[56]	[56]
S	apphire	presence of moisture [19][51][52]	0.16*	5.5*
	арринс	presence of moisture [17][31][32]	[57][58]	[59][60]
	MgO	Inert towards FLiNaK,[24]	0.23*	8.0*
	wigo	Corroded by FLiBe [19]	[61]	[61]

<sup>&</sup>lt;sup>1</sup>Strong absorption peaks located between 2.5-7 μm

### 3.1.3.3. Spectrometer and external optics

Almost all setups were designed to fit the furnace within a spectrometer sample compartment, requiring little to no modification of the optical path. A setup of particular interest which required substantial engineering of the optical path was the hot-cell-embedded Cary 14H grating spectrometer (T5). Varlamov's setup (T14) used a single-beam prism spectrometer, and an optical path schematic was given, but it is not clear if the furnace fit in the sample compartment or required external optics. The first SINAP setup (T15) fit in the sample compartment of a Perkin-Elmer spectrometer (unspecified type), but the second two (T16-17) involved the use of the fiber-optic cables, focusing optics, and modular light sources

<sup>&</sup>lt;sup>2</sup>Extended FIR transmittance presumed to be the same for polycrystalline and single-crystal specimens

<sup>\*</sup>Wavelength cutoff was calculated using equation 10

and grating spectrometers. The use of external optics is attractive because it allows for more flexibility in furnace and cell design.

High-temperature thermal radiation can disrupt visible-NIR measurements by saturating the detector, but the degree of severity is determined by the type of spectrometer and details of the optical path (e.g., numerical aperture, etc.). For a typical grating spectrometer, thermal radiation from the sample reaches the detector, but only at the narrow wavelength band selected by the grating. This effect can be accounted for by measuring a spectrum without the source, and then subtracting this intensity from the signal with the source on, as described by Liu [51]. This procedure is of course dependent on the grating being located between the sample and detector. For further discussion please see [16]. For a Fourier-transform spectrometer (FTS), the saturation effect can be much more severe. FTS are more relevant in the discussion of reflection setups, which operate in the MIR, and will be discussed in section 0.

### 3.1.4. Summary

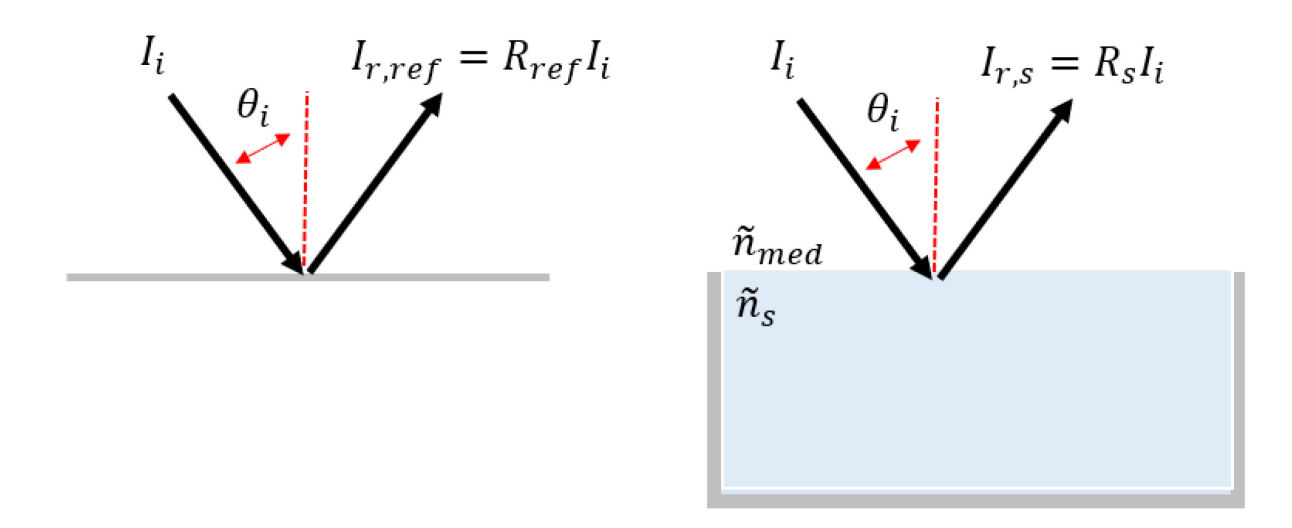
For the purposes of quantitative visible/NIR absorption measurements, we recommend the transmittance method due to simple, repeatable path-length measurement and the relative ease of coupling a spectrometer to a transmittance cell as well as potentially coupling to beam lines and/or electrochemical probes [62]. Three material combinations for transmittance cells have been well-demonstrated: graphite body with unsealed diamond windows, Hastelloy C body with graphite-sealed diamond and single-crystal SiC windows, and Au-lined Ni body with Au-sealed diamond windows. Silica or MgO cuvettes have been used in several studies, but their chemical incompatibility and failure modes are not fully understood.

Looking ahead toward future measurements, it would be of interest to develop a molten fluoride setup capable of measuring multiple path lengths. As mentioned in section 3.1.1.2, construction of such a setup (concentric, movable Inconel tubes with graphite-sealed diamond windows) has been completed, though testing with molten fluorides is yet to be done [13]. An alternative design is suggested in [16], consisting of an array of heater rods lining a machined stainless-steel block, surrounded by insulation and contained within a water-cooled brass housing. Several different sample cavities could be used, capable of holding quartz cuvettes of 2, 5 or 10 cm path length. This furnace was not included in the review because it was not used to conduct fluoride studies; however, a similar furnace could be built and used with fluoride-compatible cuvettes. In addition to increasing the range of sensitivity for measurement and detection of  $\kappa_{\lambda}$  and  $\epsilon$  of solute species, it would enable the use of the double-path-length method, enabling measurement of transparent/semi-transparent range  $\kappa_{\lambda}$  and optical properties of solvents.

# 3.2. Reflectance & Trans-reflectance

# 3.2.1. Background

Here we outline techniques used to extract  $\kappa_{\lambda}$  (and in some cases  $\tilde{n}$ ) via reflectance measurements. In section 3.2.1.1 and Figure 3a, we describe optical fitting methods to extract  $\tilde{n}$  in the opaque region (typically MIR/FIR). In section 0 and Figure 3b, we describe a framework for extracting  $\kappa_{\lambda}$  in the semi-transparent region (typically NIR), which we refer to as the trans-reflectance method.



# Semi-transparent (b)

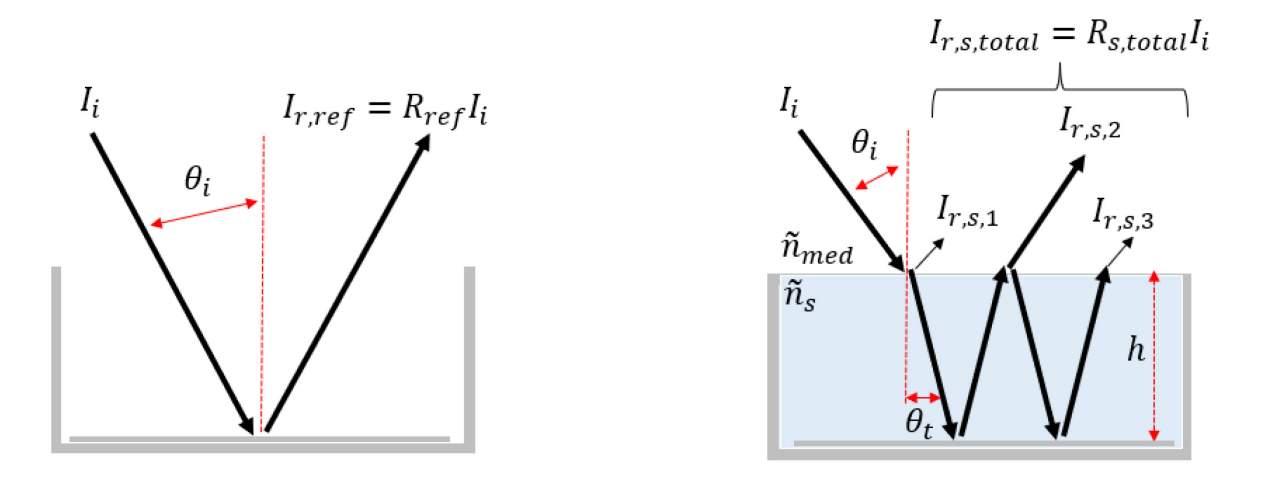


Figure 3. Schematics of reflectance for (a) opaque and (b) semi-transparent samples.

# 3.2.1.1. Opaque region

The following equation gives the sample reflectance,  $R_s$ :

$$R_{s} = R_{\text{ref}} \cdot \frac{I_{r,s}}{I_{r,ref}}$$

Here,  $R_{\text{ref}}$  is the known reflectance of a reference sample,  $I_{r,s}$  is the light intensity reflected from the

sample, and  $I_{r,ref}$  is the light intensity reflected from the reference sample.

An alternative method is to measure the sample emission to obtain,  $\epsilon_s$ , and apply Kirchoff's law:  $R_s = 1 - \epsilon_s$ . We note that this application of Kirchoff's law is only valid for an opaque sample. The following equation gives  $\epsilon_s$ :

$$\epsilon_s = \epsilon_{\text{ref}} \cdot \frac{I_{\text{e,s}}}{I_{\text{e,ref}}}$$

We note that equation 12 is only valid if background emission is negligible [63]. The emission method is preferred for samples with high emissivity, whereas the reflectance method is preferred for samples with low emissivity. For samples within an intermediate range (~0.2-0.8), we recommend both methods as a comparison. Note that for complete agreement, the numerical aperture and the angle of measurement should be the same.

If  $R_s$  is measured at near-normal incidence and  $\tilde{n}_{med}$  is known (as is generally the case in air or inert gas media), then  $\tilde{n}_s$  is the only unknown in equation 2 (here we substitute  $\tilde{n}_s$  and  $\tilde{n}_{med}$  for  $\tilde{n}_1$  and  $\tilde{n}_2$ ); however, both real and imaginary components of  $\tilde{n}_s$  must be considered. Therefore, two degrees of freedom remain to be solved for, rendering a single measurement insufficient. Here we outline optical fitting methods used by molten-fluoride spectroscopists to extract  $\tilde{n}_s$  from a single, near-normal reflectance measurement.

### Direct Kramers-Kronig

The first method involves the direct application of the Kramers-Kronig (KK) relations, which we refer to as the direct KK method [64]. The first step is to define the complex EM field reflectance,  $\tilde{r}$ , which depends on the magnitude, r, and phase shift,  $\bar{\theta}$ , as shown in the following equation.

$$\tilde{r} = re^{i\overline{\theta}}$$

The measured reflectance is related by  $R = |\tilde{r}|^2 = r^2$ . Following the formulation by Bowlden and Wilmshurst [64], r and  $\bar{\theta}$  are defined as functions of  $\omega$ , the angular frequency.  $\omega$  is related to wavelength as:  $\omega = 2\pi c/\lambda$ . Eventually, the following expression is reached, relating r to  $\bar{\theta}$ .

$$\bar{\theta}(\omega) = -\frac{1}{\pi} \int_0^\infty \frac{d[\ln r(\omega')]}{d\omega'} \ln \left| \frac{\omega' - \omega}{\omega' + \omega} \right| d\omega'$$

 $r(\omega)$  can be obtained via measurement of R; thus,  $\bar{\theta}(\omega)$  can be obtained through computation of the integral in equation 14. n and k are obtained from the following equations.

$$n = \frac{1 - r^2}{1 - 2r\cos\bar{\theta} + r^2}$$

$$k = \frac{-2r\cos\bar{\theta}}{1 - 2r\cos\bar{\theta} + r^2}$$

In practice, the integration limits of 0 and  $\infty$  are not reachable, which induces some error in this approach. Bowlden and Wilmshurst quantified this error by applying the KK method to synthetic  $\tilde{n}$  data, for the cases of an oscillator with one or two resonances. They found that if the resonances were fully captured by the integration bounds, errors near the resonance would be surprisingly small. They attributed this due to a canceling of error terms for  $\bar{\theta}$  (equation 14) that occurs when  $\omega'/\omega_{min} \approx \omega_{max}/\omega'$ . Outside of the resonance region, they observed larger error and obviously unphysical behavior, such as negative values for k (seen in Figure 5c and Figure 7a), but this was deemed acceptable for absorption spectroscopy, in which the peak location and intensity are of greater interest. They did not evaluate error in n, but the error in the product (nk) at the resonance tended to be larger than that for k alone.

We note that several reflectance studies (using R1 and R2) in this review used the KK method.

### Oscillator Model

To reduce the errors of the KK method, additional constraints must be placed on  $\tilde{n}$ . Here we present a widely used KK-consistent model wherein it is assumed that charges within the material behave as driven, damped, harmonic oscillators in response to an oscillating electromagnetic wave. For each resonance, a set of parameters (see Table 3) are defined that govern the spectral behavior of  $\tilde{\epsilon}_r$ , the relative electric permittivity.  $\tilde{\epsilon}_r$  is a complex quantity, and the equations for the real and imaginary parts are given in equations 18 and 19. Following the notation of Jasperse [65] and Mead [66], the spectroscopic wavenumber,  $\nu = 1/\lambda$ , is used here as the spectral variable.

$$\tilde{\epsilon}_r = \epsilon_r' + i\epsilon_r'' \tag{17}$$

$$\epsilon_{r'} = \epsilon_{r,\infty} + \sum_{j} \frac{4\pi \rho_{j} v_{j}^{2} (v_{j}^{2} - v^{2})}{(v_{j}^{2} - v^{2})^{2} + (\gamma_{j} v)^{2}}$$
18

$$\epsilon_{r}^{"} = \sum_{j} \frac{4\pi \rho_{j} v_{j}^{2} (\gamma_{j} v)}{(v_{j}^{2} - v^{2})^{2} + (\gamma_{j} v)^{2}}$$

Table 3. List of fitting parameters for oscillator model

$\nu_j$	Frequency of <i>jth</i> resonance
$4\pi\rho_j$	Strength of jth resonance
$\gamma_j$	Damping factor of jth resonance
$\epsilon_{r,\infty}$	Permittivity in the high-frequency limit

Under the assumption that the relative magnetic permeability  $(\mu_r)$  is equal to 1, as is the case for all known

materials across the wavelengths of interest in this review, the following equation may be used to obtain  $\tilde{n}$ .

$$\tilde{n} = \sqrt{\tilde{\epsilon_r}}$$

Then,  $\tilde{n}$  is used to calculate R, compared with the experimental R, and iterated until an acceptable fit is reached.

We note that a single molten-fluoride reflectance study (using R4) used the oscillator method. However, Jasperse [65] used the oscillator method to extract temperature-dependent (nearly up to melting point) n and k of crystalline LiF.

# Raman Spectroscopy

We note that Raman spectroscopy, which uses a high-powered laser to probe weak inelastic scattering, provides complementary vibrational information to absorption spectroscopy and can be more convenient experimentally because data is obtained from a single salt sample without the need of a reference, and thus is less impacted by defocusing effects. Vibrational modes of a given species are infrared-active, Raman-active, or both, depending on the molecular symmetry [17]. Together, Raman spectroscopy and infrared absorption spectroscopy can be used to fully characterize the accessible vibrational modes of a given species (e.g., in analysis of BeF<sub>4</sub><sup>2-</sup> [67] and Be<sub>2</sub>F<sub>7</sub><sup>3-</sup> [68] in FLiBe), but Raman data is not directly useful for RHT analysis; hence, we focus on absorption spectroscopy in this review.

# 3.2.1.2. Semi-transparent region

Use of a reflectance setup in the semi-transparent region of the salt leads to a method known as trans-reflectance. This method has found use in molten-salt optical spectroscopy because it does not require an optical window to be in direct contact with the salt sample. A representative schematic of the trans-reflectance method is given in Figure 4b. One possible setup consists of a crucible with a mirror placed at the bottom, referred to as the immersed mirror method. Another option is to suspend the mirror in the salt, referred to as the suspended mirror method. The salt layer above the mirror has a thickness of h and the path length, s, is determined in equation 21 via h and the transmitted angle,  $\theta_t$ .  $\theta_t$  is calculated using Snell's law (eq. 22), where  $\tilde{n}_{med}$  is the complex refractive index of the surrounding medium,  $\theta_i$  is the angle of incidence, and  $\tilde{n}_s$  is the complex refractive index of the salt.

$$s = \frac{h}{\cos \theta_t}$$
 21

$$\tilde{n}_{med} sin\theta_i = \tilde{n}_s sin\theta_t$$
 22

Here, we present the formulation by Barker (R3) used in an immersed mirror setup. The reflectance of the salt-vapor interface is  $R_{s,front}$  and the transmittance is  $1 - R_{s,front}$ . The reflectance of the salt-mirror interface, or back surface, is assumed to be equal to  $R_{ref}$ , the reflectance of the reference mirror in

air or inert cover gas. The transmittance of the salt layer is  $\mathcal{T}_s = \exp(-\kappa_{\lambda} s)$ . The total reflected light intensity,  $I_{r,s,total}$ , can then be divided into several components. The first,  $I_{r,1}$ , is reflected by the front surface. The second,  $I_{r,2}$ , transmits through the front surface, reflects from the back surface, then transmits again through the front surface.  $R_{ref}$  is typically near 1; hence, multiple reflections may occur, depending on the magnitudes of  $R_{s,front}$  and  $\mathcal{T}_s$ .

$$I_{r,s,total} = R_{s,total}I_{i} = I_{r,1} + I_{r,2} + I_{r,3} + \dots + I_{r,n} + \dots = \sum_{i=1}^{\infty} I_{r,i}$$
23

$$R_{s,total} = R_{s,front} + R_{ref} \left(1 - R_{s,front}\right)^2 \mathcal{T}_s^2 \left(1 + R_{s,front}R_{ref}\mathcal{T}_s^2\right)$$
24

The equation for  $R_{s,total}$  (eq. 24) is given by Barker [69], and only accounts for  $I_{r,i}$  up to i=3. This was deemed acceptable because higher order terms would include  $R_{s,front}$  raised to the second power or higher, and  $R_{s,front}$  had been determined to be on the order of a few percent. In Barker's experiment,  $R_{s,front}$  was measured independently by replacing the mirror with a sandblasted substrate, which effectively reduced  $R_{ref}$  to near zero.

Khokhryakov (R7) presents a simplified immersed-mirror approach wherein  $R_{s,front}$  is assumed to be 0, resulting in  $R_{s,total} = R_{ref} \mathcal{T}_s^2$  [70]. Beer's Law is then employed to obtain  $\mathcal{T}_{solute}$  (reported as  $A_{solute}$ ).

Zhang (R6) presents yet another approach using the suspended mirror method [71]. By hanging a mirror within the melt at a slight angle, they were able to spatially separate the various reflected components, and selectively measure  $I_{r,2} = R_{ref} (1 - R_{s,front})^2 T_s^2 I_i$ . The mirror could then be lowered or raised to perform subsequent measurements at different path lengths, enabling the use of the double-path-length method.

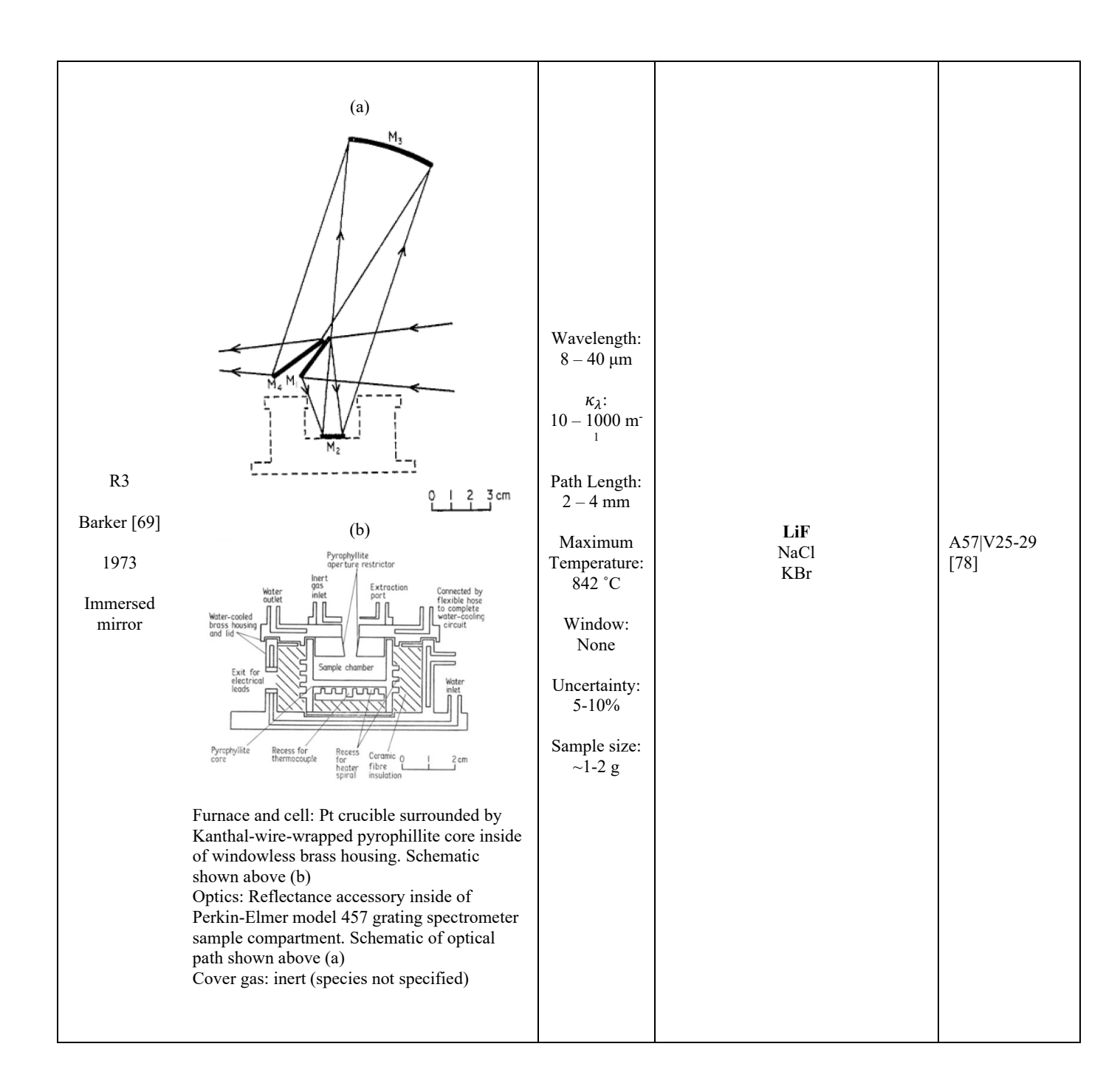
### 3.2.2. Compilation of reflectance setups

Table 4 lists the reflectance setups covered in this review. For clarity, the setups have been defined by each unique combination of cell, furnace, and optical path. In the first column, we give the setup index (R#), primary author and reference, year of publication, and data-processing method (i.e., Direct KK, oscillator model, immersed mirror, suspended mirror). The second column provides schematics and equipment details (i.e., furnace, cell, optical path, cover gas). The third column gives parameters such as wavelength range, maximum or range of  $\kappa_{\lambda}$  measured, maximum temperature, optical window used, amount of salt required, and reported uncertainty. The next columns give details on the studies performed, such as the salt compositions used, and provides references to relevant plots (A#) and spectra indices (E#/V#).

Table 4. Experimental reflectance and trans-reflectance setups for measurement of  $\kappa_{\lambda}$  via extraction of optical properties using optical theory or via various trans-reflectance techniques. If unspecified, sample size was estimated using dimensions of crucible and assuming to be 2/3 full and using an approximate salt liquid density of 2 g/cm<sup>3</sup>.

Experimental	Schematic and Equipment Details	Parameters		d	
Set-up		rarameters	Salt Con	Salt Composition	
			Solute	Solvent	Data
R1 Wilmshurst [72] [73] 1963 Direct KK	Furnace: no details given Cell: Ni crucible Optics: Perkin-Elmer Model 12C spectrometer (NaCl, KBr, CsI prisms) Schematic of optical path [73]: S – light source; OB – optical bench; F1, F2 – spherical mirrors; M1, M2 – mirrors; M1 – standard mirror; J – monochromator slit Cover gas: Argon Reprinted from [73], with the permission of AIP Publishing.	Wavelength: $10 - 50  \mu m$ Max $\kappa_{\lambda}$ : $7.6E+05  m^{-1}$ Max  Temperature: $850  ^{\circ}C$ Window: None  Uncertainty: $2\%$ repeatability  a  Sample size: NR	Range of co LiF-K (37.5-37.5 NaF-K	-KF ompositions F-ZrF <sub>4</sub> -25 mol%) F-ZrF <sub>4</sub> ompositions	A46 V35-39 A47 V37, V40 A48 V41-45 [74]
R2 Fordyce [75] [76] 1965 Direct KK	Furnace: R1 Cell: Ni or Pt crucible held inside of sealed, windowed inconel container Schematic of optical cell: A – Ar inlet; B – Ar outlet; C – cooling coil; D-thermocouple sleeve; E – Ni crucible; F – windows; G – teflon wipers; H – wiper manipulator Optics: Perkin-Elmer 221 double-beam spectrometer (CsBr prism) for λ < 40 μm Perkin-Elmer 12C (CsI prism) for λ > 38 μm	Wavelength: $10-50~\mu m$ Max $\kappa_{\lambda}$ : $5.6E+05~m^{-1}$ Max Temperature: $750~^{\circ}C$ Window: KBr b, Csl b  Uncertainty: $5\%$ precision $10\%$ ( $\lambda > 20$ $\mu m$ ) due to $H_2O$ vapor fine absorption  Sample size: $\sim 50~g$	$TaF_5$ $NbF_5$ $TaF_5 + H_2O$	LiF-KF LiF- NaF equimolar LiF-KF equimolar LiF-KF equimolar	A49 V46-48 A50 V49-50 A51 V47-48 A52 V50 [75] A53 V51-52 A54 V52 [76] A55 V53-54 A56 V55-57

Same optical path as R1 Cover gas: Argon		
Reprinted from [76], with the permission of AIP Publishing.		
All I dollshing.		



		Wavelength:			A 501V/50
R4  Mead [66]  1973  Oscillator model	Furnace and cell: R3 Optics: Perkin-Elmer model 457 grating spectrometer for $\lambda < 40~\mu m$ Fourier Transform Spectrometer (FTS) for $\lambda > 40$ National Physical Laboratory Michelsen type interferometer (Grubb-Parsons Ltd) Melinex beamsplitters quartz-windowed Golay detector Cover gas: inert (species not specified)	Max κ <sub>λ</sub> : 7.0E+05 m <sup>-1</sup> Maximum Temperature: 1023 °C  Window: none  Uncertainty: 2% fit error a 2% repeatability a 2% background emission a 0.5% spectrometer noise a	L		A58 V58 A59 V30-33 [66]
		Sample size: ~0.1-6 g	C	sF	A60 V59-61 [79]
R5 Andersen [54] 1999 Immersed mirror / Beer's Law	Furnace: Aluminum-bronze core with four heater rods Cell: Au-lined Ni cylinder with Au-sealed diamond windows Schematic of optical cell shown above A: screws; B: top lid; C: Ni ball; D: Au gasket; E: Au lining; F: thermocouple well; G: sample chamber; H: Ni body; I: Au piston; J: diamond window; K: bottom lid Optics: Bomen DA3.026 FTS Globar source, KBr beamsplitter, MCT detector Cover gas: Ar Reprinted with permission from [55]. Copyright 1999 American Chemical Society.	Wavelength: $7-22 \mu m$ $\kappa_{\lambda}$ : NR  Path Length: $\sim 0-2 mm$ Temperature: $750 ^{\circ}\text{C}$ Window: Diamond  Uncertainty: NR  Sample size: $\sim 80  \text{mg}$	K2NbF7 Na2O	FLiNaK	A61 V65-68 [54]

			I		<del>                                     </del>
R6 Zhang [71] 2001 Suspended mirror / double-path- length method	Furnace: Details not given.  Cell: Pt crucible with Pt suspended mirror Optics: Mattson Galaxy FTS  Tungsten filament source, MCT or Si detector Schematic of optical path F1-5: flat mirrors; S1-2: spherical mirrors; I1- 2: irises (aperture) Cover gas: NS Reprinted by permission of the publisher (Taylor & Francis Ltd).	Wavelength: $0.8-3.33$ $\mu m$ $\kappa_{\lambda}$ : $10-250$ m <sup>-1</sup> Path Length: $4-10$ mm  Temperature: $1300$ °C  Window: None  Uncertainty: $<10\%$ Sample size: NR	Si, Ca, Al, E	3 oxide glass	[71]
	1 2 3 10 8 7 4 9		CeF <sub>3</sub> Ce <sub>2</sub> O <sub>3</sub>	LiF-NaF LiF-NaF-ZrF4	A62 E55-56 [81]°
R7 Khokhryakov	6 11	Wavelength: $0.25 - 1.67$ $\kappa_{\lambda}$ : NR  Path Length: $\sim 2.0$ mm	CoF <sub>2</sub> FeF <sub>3</sub>	CaF2 BeF2 NaF	A63 E26 A64 E27 A65 E28 A66 E29 [80]
[80] 2014  Immersed mirror / Beer's Law	Furnace: Mo-wrapped alumina rod inside of sealed assembly Cell: Pt-Rh crucible with immersed Pt-Rh mirror Optics: UV-Vis \$150-2048/250 grating	Temperature: 1377 °C  Window: Sapphireb  Uncertainty: NR  Sample size: ~0.6 g	PrF <sub>3</sub> Pr <sub>2</sub> O <sub>3</sub>	FLiNaK LiF NaF KF CsF	A67 E57-60 A68 E61 A69 E62 A70 E63 [82]
	spectrometer, 10140-1108 CCD matrix detector S150-250-IR spectrometer, InGaAs linear photodiode matrix (G9201-256S) Schematic of optical path shown abvove 1: optical fiber transmitting light from source; 2: collimator; 3: mirror; 4: 50-50 beamsplitter; 5: melt sample; 6: sapphire window; 7: collimator; 8: optical fiber transmitting light to detector; 9: shutter; 10: Pt-Rh reference sample;		GdF <sub>3</sub>	LiF NaF KF CsF NaF-CsF	A71 E64-69 [83]

11: optical trap; 12: water-cooled cell body; 13:	
heater; 14: Pt-Rh container; 15: Pt-Rh mirror;	
16: Pt-Rh thermocouple; 17: gas port	
Cover gas: He	
Reprinted by permission from: Springer	
Nature, Russian Metallurgy, Spectral-	
analytical system for recording the electronic	
spectra of high-temperature melts and its	
technical frontier, Khokhryakov et al., [81],	
(2014).	

<sup>&</sup>lt;sup>a</sup>Uncertainty values are provided are with respect to R

### 3.2.3. Discussion

### 3.2.3.1. Furnaces

As with the transmittance method, the reviewed molten-fluoride reflectance setups have all used resistively heated furnaces. Wilmshurst (R1) and Zhang (R6) give schematic views showing uncovered, cylindrical ovens holding a crucible filled with molten salt (or glass), but provide no details of construction; thus, it is likely that commercial ceramic ovens were used with minimal modification. Wilmshurst reported that Ar was flushed across the melt surface. Barker designed a smaller furnace that consisted of a Kanthal-wire-wrapped pyrophyllite core, surrounded by insulation and contained within a water-cooled brass assembly (R3). A beam slit was introduced above and inert gas was flushed across. Andersen reports the use of an aluminum-bronze metal core with four heater rods (R5), without further details or a schematic. Khokhryakov's furnace (R7) consisted of a Mo-wrapped alumina rod contained within a vacuum-tight enclosure and used He flush gas.

### 3.2.3.2. Cells

In general, reflectance cells are much simpler than transmittance cells and, in some cases, consist of simply a crucible. For the trans-reflectance method, a mirror must be immersed or suspended. Pt (R3-4 and R6), Au (R5), Pt-Rh (R7), and Ir (R7 [81]) have been demonstrated as suitable crucible and salt-immersed mirror materials. Defocusing issues can arise due to meniscus formation in smaller crucibles (Barker used 25 mm diameter, but recommended 40 mm to completely remove this effect [69]). Khokhryakov (R7) reports the use of 20 mm diameter without mention of defocusing; however, they reported crucible warping due to melt surface tension at very high temperature (~1400 °C). Wilmshurst and Zhang did not report crucible diameter.

Two of the more complex cell designs are described by Fordyce (R2) and Andersen (R5). Based on Fordyce's schematic (R2), their crucible appears to be about 40 mm diameter. Their cell was designed for use with high vapor pressure melts, which required holding the crucible in a sealed Inconel container

<sup>&</sup>lt;sup>b</sup>Window not in contact with liquid salt

<sup>&</sup>lt;sup>c</sup>Older version of setup used [84]

with optical windows. The optical windows were flushed with Ar gas and included movable Teflon<sup>TM</sup> wipers to remove deposits. Andersen designed another unique reflectance cell (R5) consisting of a Au-lined Ni cylinder sealed with Au gaskets against a Ni ball at one end and against a diamond window at the other. The cell was held inverted, such that the salt would rest directly on the diamond window. For short pathlength measurements, an Au piston was inserted to press the salt onto the window. This is the sole transreflectance design in which a salt-facing window was used; thus, it is relevant also for transmittance cell design.

When performing trans-reflectance measurements, another challenge for smaller crucibles is the path-length measurement. Typically, it is difficult to access the salt during optical measurements and insertion of a cold depth probe would remove frozen salt after the measurement. Barker laboriously measured the salt depth using a Pt electrically heated contact probe combined with visual access and a vertically moving stage to determine the locations of the crucible bottom and salt surface, reporting an uncertainty of 5-10%. Depth could also be calculated by using the measured sample mass and cup dimensions, along with the salt's temperature-dependent density. Use of a larger crucible by Zhang enabled the suspended mirror approach (R6), which consisted of a Pt mirror suspended by three Pt rods. The mirror was aligned to the optical path, and the furnace was mounted below on a translation stage. After melting the sample, the furnace would be raised until the mirror became immersed, and measurements would take place at multiple path lengths, enabling the double path length method to be used. Uncertainty was reported to be less than 10%.

### 3.2.3.3. Spectrometer and external optics

All the reflectance setups required reflective external optics to direct light onto the melt and collect the reflected light. The simplest case was the reflectance accessory designed by Barker (R3), which fit in a Perkin-Elmer model 457 grating spectrometer sample compartment. Likewise, Andersen (R5) reports that their furnace fit inside of a Bomen FTS sample compartment, but does not give details regarding reflective optics. Due to their larger furnaces, Wilmshurst (R1) and Zhang (R6) used considerably external optics consisting mostly of reflective optics (preferred for MIR measurements). Likewise, Khokhryakov's large furnace required significant external optics (R7); however, their setup consisted of fiber optics and lenses.

A challenge faced by high-temperature reflection measurements in the MIR is detector saturation due to sample thermal emission. As mentioned in 3.1.3.3, the problem is present for both FTS and grating spectrometers, but is more severe for the former. Zhang (R6) briefly described the problem and outlined a mitigation strategy: increasing the power of the light source and reducing the solid angle of the light leaving the sample to keep the detector in the un-saturated regime. This saturation issue and a similar attenuation strategy is discussed in detail in [85]. Another example of optics design aimed at maximization of source

intensity and throughput can be found in Appendix A of [86]. In addition to these mitigation strategies, the direct emission can be used to improve measurement reliability by performing a complementary emissivity measurement, as shown by Mead (R4).

# 3.2.4. Summary

Reflectance setups can be more complex than transmittance because they require at a minimum a reflective optical accessory (R3) and at most extensive optical components external to the spectrometer (R1, R6). That said, fluoride salts are highly absorptive in the MIR through the FIR, making reflectance measurements better suited for quantitative determination of  $\kappa_{\lambda}$  in this region. This is generally done via R measurement over a wide spectral range, followed by application of optical fitting (direct KK or oscillator model) to determine n and k. A challenge related to MIR measurements are that optical fibers are less commercially available, requiring bulkier reflective optics. FTSs are typically used in this region and tend to be more expensive than grating spectrometers and are more susceptible to saturation. For qualitative visible-NIR measurements, the trans-reflectance method, as demonstrated by Khokhryakov (R6), has advantages over transmittance due to simpler optical cell design, typically consisting of a Pt crucible with a Pt (or Pt-Rh) immersed mirror.

If the challenge of building a MIR reflection setup is taken on, the results could be quite fruitful. We recommend the suspended mirror approach (R6), enabling quantitative trans-reflectance measurements in the visible-NIR. Following that, reflectance measurements could be made in the MIR-FIR along with optical fitting to obtain n and k. Such a wide spectral range can be relatively easily accomplished via a FTS using appropriate combinations of sources, beamsplitters, and detectors. Of course, great care must be taken to maximize the power and throughput of the source in combination with attenuation, collimation, and solid-angle reduction to avoid saturation due to direct emission by the sample. Through optical fitting via an oscillator model or KK, this setup would enable complete optical property characterization. To improve the optical fitting accuracy, the setup could be modified to allow for measurements at varying incident angles and varying polarization. Addition of an external MIR detector would allow for complementary emission measurements, increasing the measurement reliability.

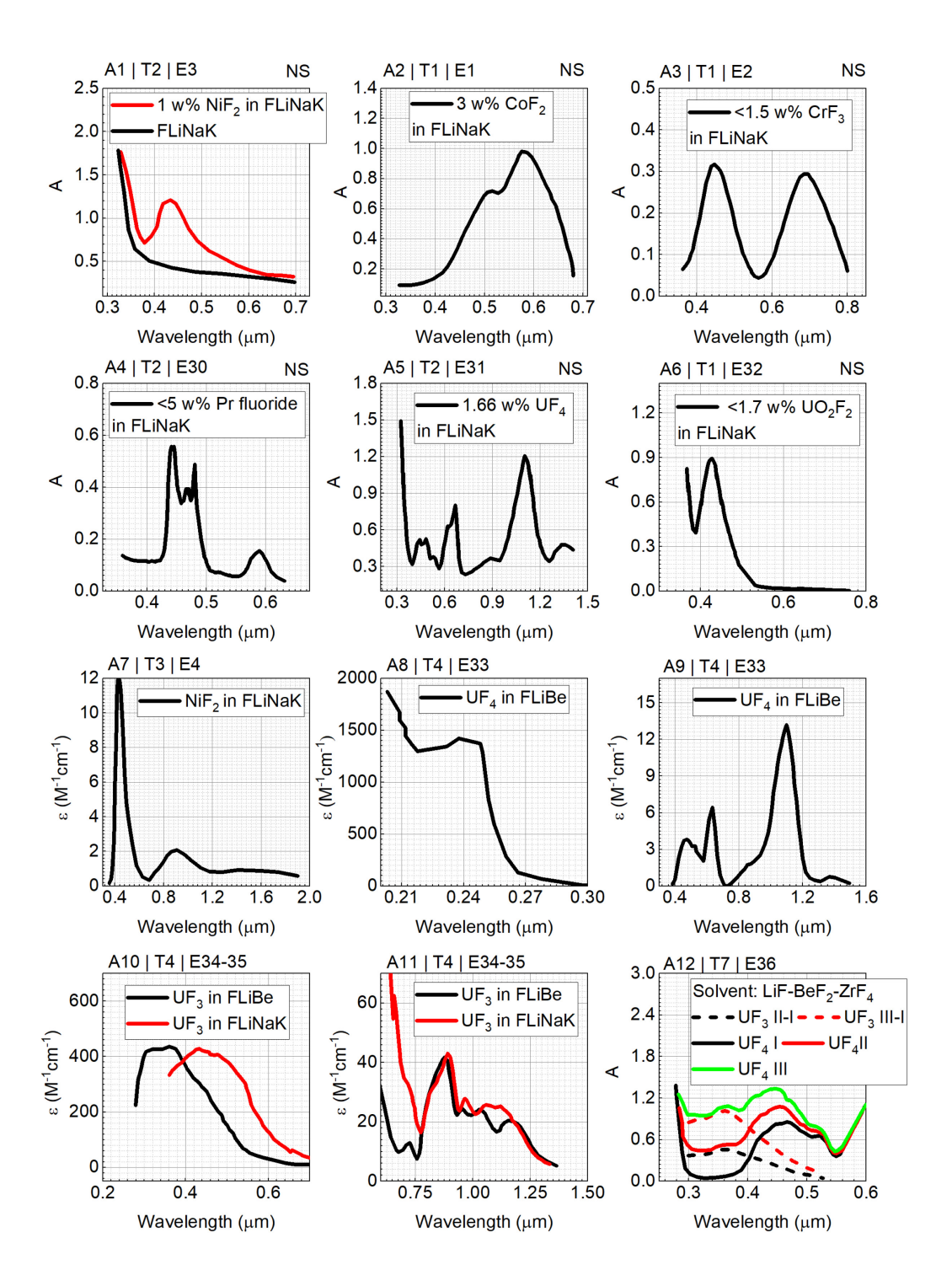
#### 4. EXPERIMENTAL DATA

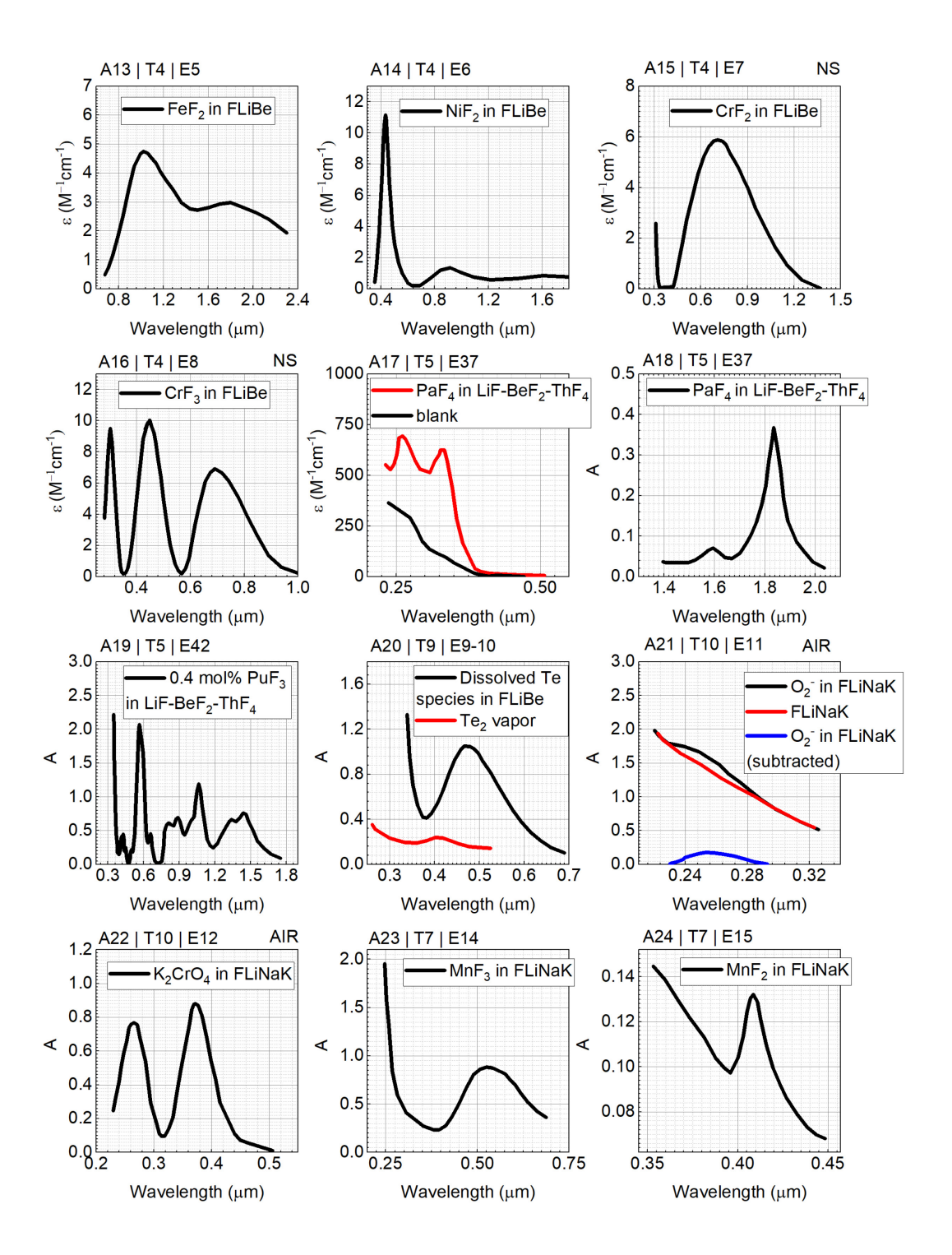
Here, we provide the molten-fluoride optical absorption data compiled from our search. We present spectral data in Figure 4, which consists of 71 plots generated from data digitized from graphs using the Origin<sup>TM</sup> 2016 v.93E and 2020 software. We provide the data in digital format with the supplemental materials. The molecular structure of the salt dictates the observed optical resonances. The wavelength of the resonances, in turn influences their impact on RHT. The two types of resonances that are found in the

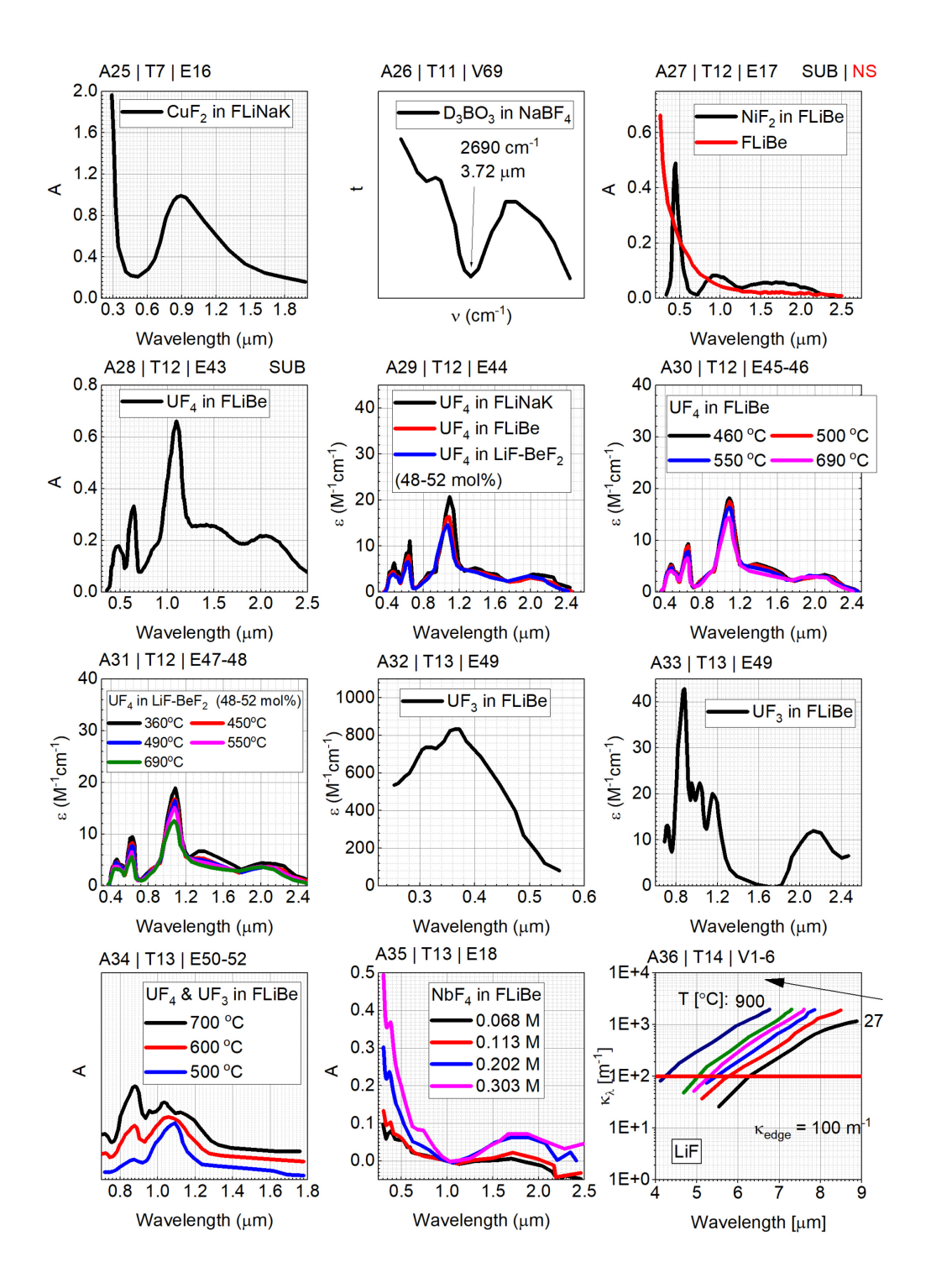
wavelength range relevant to RHT are electronic and vibrational. We summarize solvent vibrational edge absorption data in Table 5 and solvent and solute vibrational resonance absorption data in Table 6, listing the peak locations and intensities. We summarize solute electronic absorption data in Table 7 (lighter elements) and Table 8 (heavier elements).

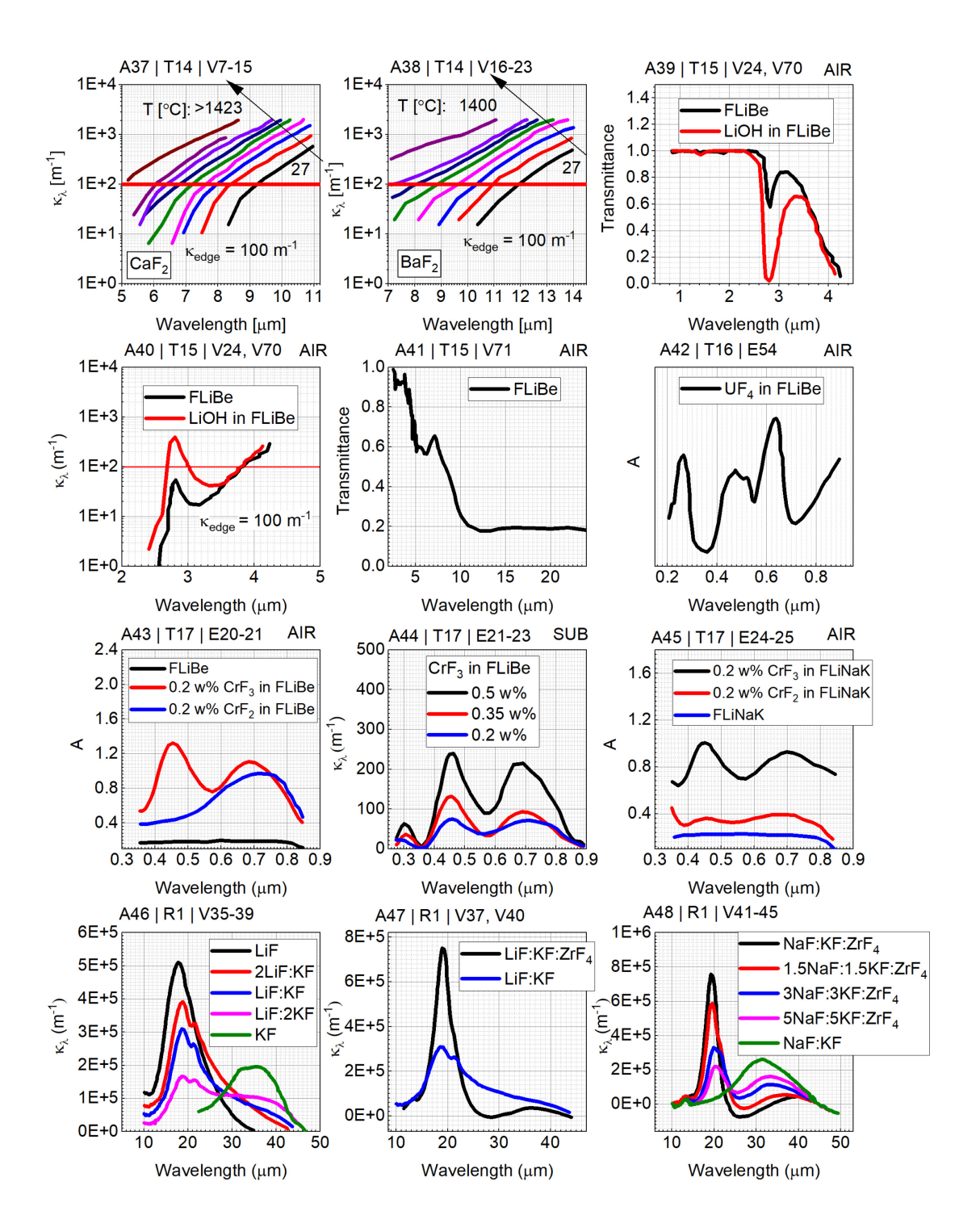
# 4.1. Compilation of Spectra

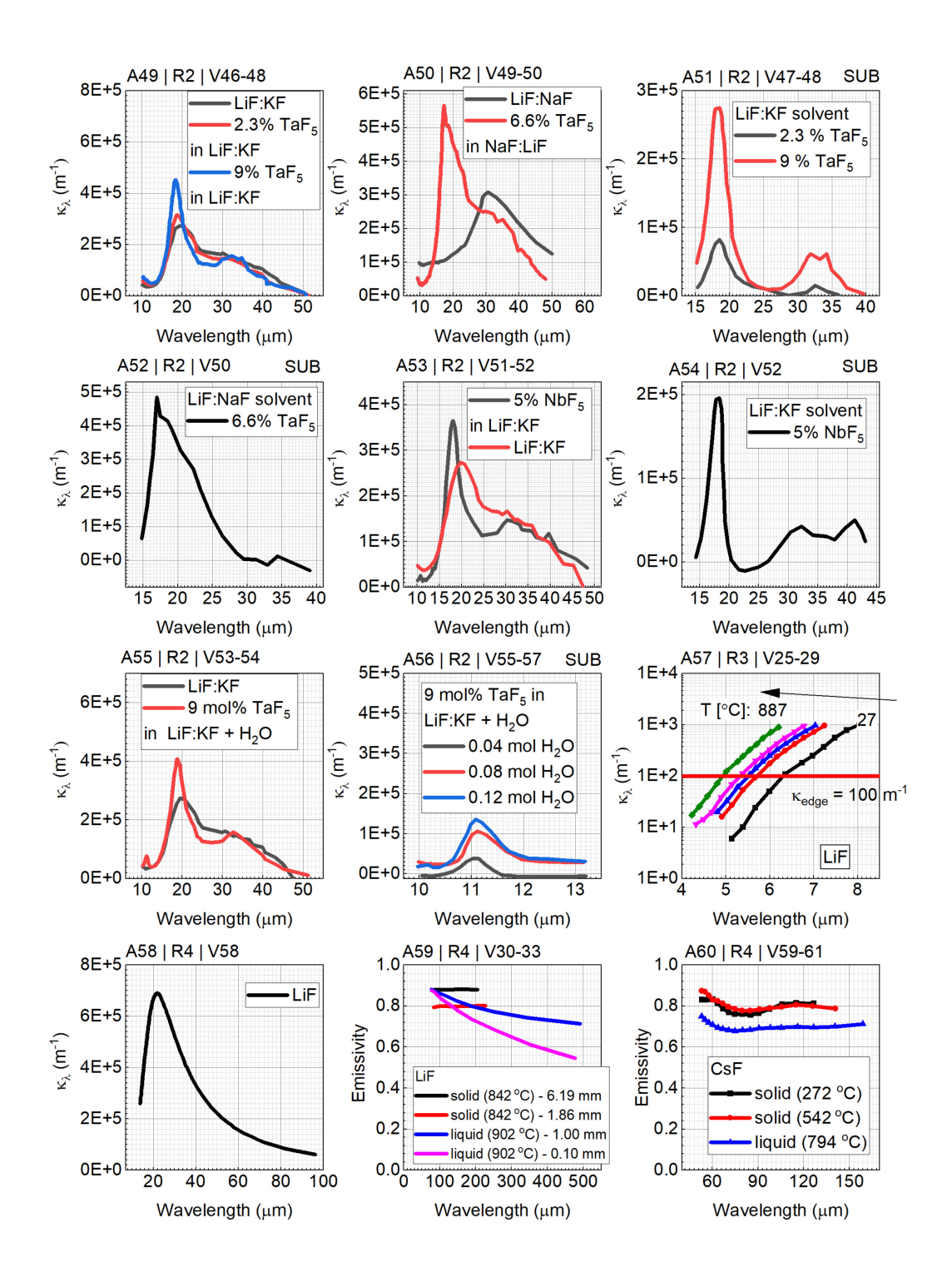
Figure 4. Compilation of optical spectra for molten fluoride salts in the visible and infrared range, following the order in which the corresponding setups are introduced in Table 1 and Table 4. Each plot is identified at the top left corner by plot index | setup index | spectra index; details on the spectra can be found by looking up the spectra index (e.g., E#, V#) in Table 5, Table 6, Table 7, and Table 8; details on the setup used can be found by looking up the setup index (e.g., T#, R#) in Table 1 and Table 4. Vertical-axis variables: A absorbance,  $\kappa_{\lambda}$  spectral linear absorption coefficient,  $\epsilon$  molar absorptivity, transmittance, emissivity, and R reflectance. Horizontal axis: wavelength. The  $\mu$ m unit was selected because of its relevance to RHT analysis. When possible, we report the reference spectra used (except for  $\epsilon$ ): 'NS' neutral density screen reference, 'AIR' air reference, 'SUB' solvent-subtracted. Data files for all plots are provided as supplemental material.

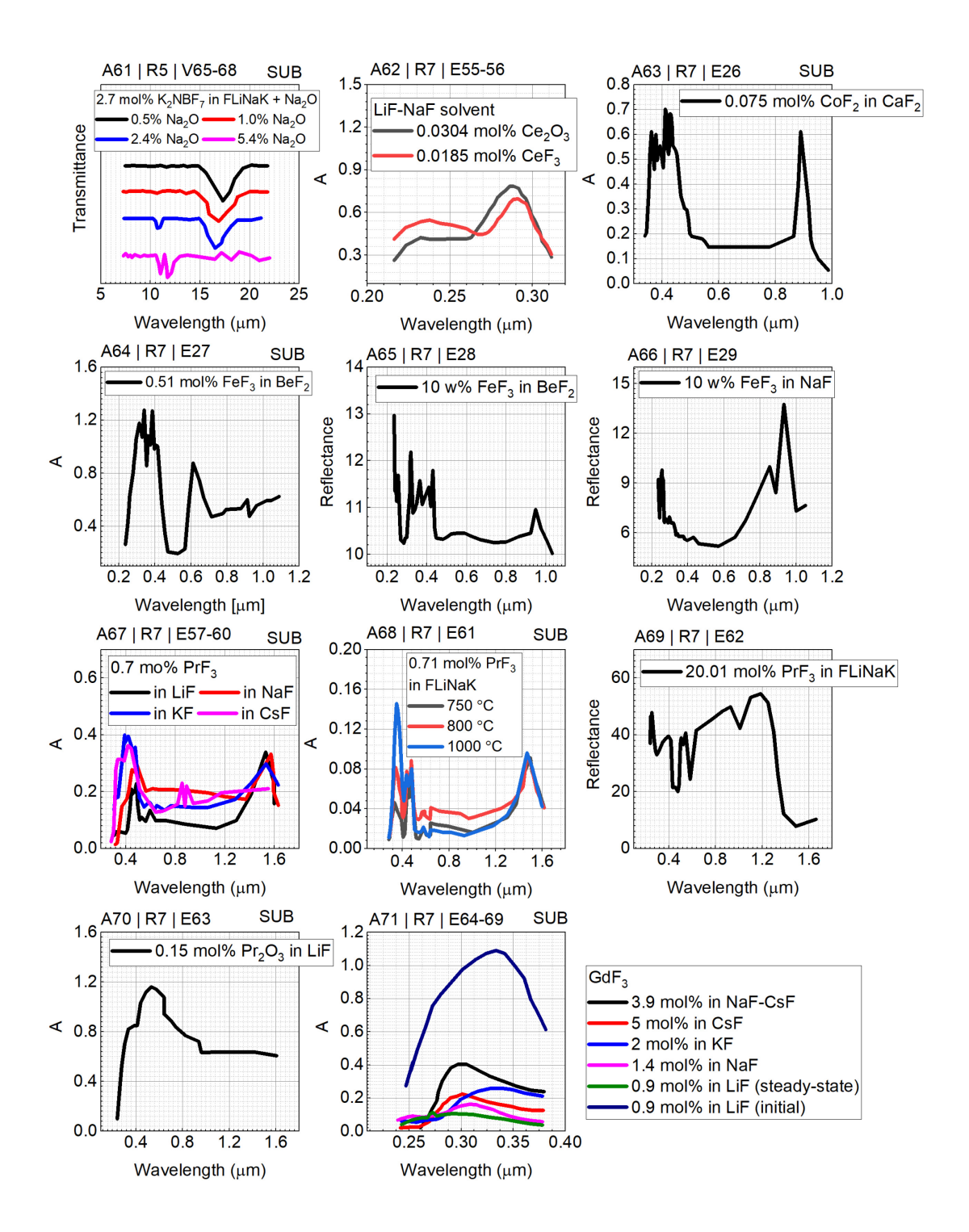












## 4.2. Tabulation of Vibrational Absorption Data

Table 5. Measurements of infrared absorption edge data in molten fluoride salts. The edge location is defined as the wavelength at which  $\kappa_{\lambda_{min}} = 100 \text{ m}^{-1}$  is reached. Details on the setup used can be found by looking up the setup index (e.g., T#, R#) in Table 1 and Table 4. Plots can be found in Figure 4.

Spectrum#	Plot #	Method	Temperature (°C)	Composition	Path Length (mm)	Edge location (µm)
V1 V2 V3 V4	A36		27 227 427 627	LiF		6.3 5.8 5.5 5.3
V5 V6 V7	-		752 900 (liquid)	-		5.1 4.2 9.2
V7 V8 V9 V10		T14	27 227 427 627			8.4 8 7.6
V11 V12 V13	A37	Setup and study: Varlamov [49]  Wavelength: 4 – 14 μm	827 1027 1227	CaF <sub>2</sub>	NR	7.2 6.8 6.4
V14 V15 V16			1352 >1423 (liquid) 27			6.1 ~5 11.9
V10 V17 V18 V19 V20	A38		227 427 627 827	BaF <sub>2</sub>		10.9 10.3 9.6 8.9
V20 V21 V22 V23			1027 1227 1400 (liquid)			8.9 8.1 7.2 <7
V24	A39 A40	T15 Setup and study: S. Liu [50] Wavelength: 0.8 – 4.7 µm	600	FLiBe	10	4.2
V25 V26 V27 V28	A57	R3 Setup: Barker [69] Study: Barker [78]	27 432 562 702	LiF	1-2	6.3 5.7 5.5 5.3
V29 V30 V31		Wavelength: 4 – 8 μm  R4 Setup: Barker [69]	890 (liquid) 842		6.19 1.86	4.9
V32 V33	A59	Study: Mead [66] Wavelength: 100 – 500 μm	902 (liquid)	LiF	0.10	NR
V34	N/A	Study: Chaleff [9]  Wavelength: 4 – 10 µm	700	FLiNaK	NR	7.2

Table 6. Measurements of vibrational resonance absorption in molten fluoride solvents and solutes. Details on the setup used can be found by looking up the setup index (e.g., T#, R#) in Table 1 and Table 4. Plots can be found in Figure 4.

Spectrum	Plot			(mole rat	osition tio / mole cent)		Peaks					
#	#	Method	Temp (°C)			Speciation	NIR/MIR:	< 20 μm	MIR: 20-2	5 μm	FIR: >25 µ	ım
				Solute	Solvent		Location	Intensity	Location	Intensity	Location	Intensity
							(µm)	(m <sup>-1</sup> )	(µm)	(m <sup>-1</sup> )	(µm)	(m <sup>-1</sup> )
V35	A46				iF		17.75	5.1E+05	20.25sh	4.0E+05 <sup>sh</sup>		
V36	11.0			2LiI	F-KF		18.75	3.9E+05	21.5	3.25E+05		
V37	A46 A47	R1		LiF	-KF		18.75	3.1E+05	21.25	2.65E+05		
V38		Setup:		LiF-	-2KF	-	18.75	1.75E+05	21.5	1.55E+05	31.5 <sup>sh</sup>	1.1E+05 <sup>sh</sup>
V39	A46	Wilmshurst [72]		K	XF.						33 <sup>sh</sup> 36.75	1.9E+05 <sup>sh</sup> 1.95E+05
V40	A47			LiF-K	F-ZrF <sub>4</sub>	-	19	7.5E+05	21.5sh	3.7E+05 <sup>sh</sup>	36.5	3.5E+04
V41		Study:	NR	NaF-K	F-ZrF <sub>4</sub>	NR	19.2	7.6E+05			40	4.0E+04
V42		Wilmshurst		1.5NaF	-1.5KF-	-	19.5	5.0E±05	21.5sh	3.5E+05 <sup>sh</sup>	35 <sup>sh</sup>	5.0 E+04
V42		[74]		Zr	rF <sub>4</sub>		19.5	5.9E+05	21.5	3.5E+05***	37	6.0E+04
V43				3NaF-3	KF-ZrF <sub>4</sub>				20	3.3E+05	33	1.2E+05
V 43	A48	Wavelength:		31 <b>\a</b> 1 -3.	KI -ZII 4				21.5sh	2.1E+05 <sup>sh</sup>	36 <sup>sh</sup>	1.1E+05
V44		10 - 50		5NaF-5	KF-ZrF <sub>4</sub>				20.5	2.2E+05	33	1.6E+05
					· ·						36 <sup>sh</sup>	1.4E+05
V45				NaF	-KF						31.5	2.6E+05
											36 <sup>sh</sup>	2.0E+05
V46	A49	R2 Setup:		LiF	-KF	NR	19.5	2.7E+05			30.5	1.7E+05
V47	A49	Fordyce		TaF <sub>5</sub>			19	32E+05			31	1.5E+05
<b>V T</b> /	A51	[75]		2.3%	LiF-KF	TaF <sub>7</sub> <sup>2-</sup>	18.5*	8.20E+04*			33*	1.5E+04*
V48	A49			TaF <sub>5</sub>	Lii iti	Tui /	18.5	4.5+05			32	1.6E+05
V 40	A51	Study:	680 - 750	9%			18.5*	2.75E+05*	-		32.5*	6.0E+04*
V49	A50	Fordyce [75]		NaF	-LiF	NR					30.5	3.1E+05
	A50	[,3]		TF	NE	T. F.	17.5	5.65E+05			30	2.5E+05
V50	A52	Wavelength: 10 - 50		TaF <sub>5</sub> 6.6%	NaF- LiF	TaF <sub>6</sub> - TaF <sub>7</sub> <sup>2</sup> -	19*	4.8E+05*			34.5*	1.0E+04*
V51	A53	R2 Setup: Fordyce	700	LiF	-KF		19	2.75E+05			31	1.65E+05
V52	A53	[75]		NbF <sub>5</sub>	LiF-KF	NbF <sub>7</sub> <sup>2-</sup>	18.5	3.65E+05			31	1.45E+05

				5%							41	1.1E+05
		Study: Fordyce									32*	4.0E+04*
		[76]										
	A54						18.5*	1.95E+05*			42*	5.0E+04*
		Wavelength: 10 - 50										
V53		10 30			LiF-KF	NR	20	2.7E+05			34 <sup>sh</sup>	1.4E+05
	_			Solute:		112		21,2100				1112100
V54	A55			TaF <sub>5</sub>			19	4.1E+05			32	1.6E+05
V 34				9% +			11	8.0E+04			32	1.0E+03
	1	R2		H <sub>2</sub> O TaF <sub>5</sub>								
		Setup: Fordyce		9% +								
V55		[75]		0.04			11*	3.8E+04*				
				mol H <sub>2</sub> O								
		Study: Fordyce	720	TaF <sub>5</sub>	LiF-KF	TaOF <sub>6</sub> <sup>3-</sup>						
		[77]		9% +								
V56	A56			0.08 mol			11*	1.0E+05*				
		Wavelength: 10 - 50		H <sub>2</sub> O								
		10 - 30		TaF <sub>5</sub>								
****				9%+				1.45.05*				
V57				0.12 mol			11*	1.4E+05*				
				H <sub>2</sub> O								
		R4			ľ							
		Setup: Barker [69]										
		[00]										
V58	A58	Study:	902	LiF (	liquid)	NR			21.5	6.9E+05		
		Mead [66]										
		Wavelength:										
		10 – 100										
V59		R4 Setup:	272									
V60		Barker [69]	542									
	1										50	
	A60	Study: Mead [79]		C	'sF	NR					72	NR
V61		111044 [//]	794 (liquid)									
		Wavelength:										
		50 – 160										

V62	N/A	Setup &	-265				20 <sup>sh</sup>	9.0E+05	31	7.6E+06		
V63	N/A	Study: Jasperse	147				20 <sup>sh</sup>	9.0E+05	32	2.5E+06		
V64	N/A	[65] Wavelength: 10 – 100	787	LiF (	solid)	NR	20 <sup>sh</sup>	9.0E+05	32	1.3E+06		
V65				K <sub>2</sub> NbF <sub>7</sub> 2.7% + Na <sub>2</sub> O 0.5%		NbF <sub>7</sub> <sup>2-</sup>	17.25	NR				
V66	A61	R5 Setup & Study: Andersen	600	K <sub>2</sub> NbF <sub>7</sub> 2.7% + Na <sub>2</sub> O 1.0%	FLiNaK	NbOF <sub>5</sub> <sup>2-</sup>	10.75 16.75	NR				
V67		[54] Wavelength: 7 - 22		K <sub>2</sub> NbF <sub>7</sub> 2.7% + Na <sub>2</sub> O 2.4%		NbOF <sub>5</sub> <sup>2-</sup>	10.75 16.75	NR				
V68				K <sub>2</sub> NbF <sub>7</sub> 2.7% + Na <sub>2</sub> O 5.4%		NbO <sub>2</sub> F <sub>4</sub> <sup>3</sup> -	11 12	NR				
V69	A26	T11 Furnace: Young [27] Cell and Study: Bates [41] Wavelength: NR	425	D <sub>3</sub> BO <sub>3</sub>	NaBF <sub>4</sub>	BF <sub>3</sub> OD	3.72	NR				
V70	A39 A40	T15 Setup &		LiOH	FLiBe	OH-	2.78	170				
V71	A41	study: Liu [50]  Wavelength: 0.83 - 25	600	FL	iBe	BeF <sub>4</sub> <sup>2</sup> -	6.25 12.5	NR				
V72	N/A	Setup & study: Quist [67]	Room temperature		(Li-7) lid)	BeF <sub>4</sub> <sup>2-</sup>	11.6 12.4 12.9	NR	20 21.6 23 24.7	NR	26.9 27.8 30	NR

V73	N/A			FLiBe (Li-6) (solid)	BeF <sub>4</sub> <sup>2-</sup>	11.6 12.4 13	NR	19.2 20.6 21.9 24	NR	26.3 27.7 29.4	NR
-----	-----	--	--	-------------------------	--------------------------------	--------------------	----	----------------------------	----	----------------------	----

sh indicates a shoulder rather than a sharp peak

NR indicates the parameter was not reported

<sup>\*</sup>indicates signal has been subtracted from solvent background

# 4.3. Tabulation of Electronic Absorption Data

Table 7. Measurements of electronic absorption for transition-metal elements and tellurium. Details on the setup used can be found by looking up the Setup Number (e.g., T#, R#) in Table 1 and Table 4. Plots can be found in Figure 4.

Su satu				Comp	osition	Speci ation	Path Length (cm)	Visible (<0.8			rared Peaks >0.8μm)
Spectr um #	Plot #	Method	Temp (°C)	Solute	Solvent			Peak Location (μm)	Peak intensity $\kappa_{\lambda}$ (m <sup>-1</sup> ) or $\varepsilon$ (M <sup>-1</sup> cm <sup>-1</sup> )	Peak Location (μm)	Peak intensity $\kappa_{\lambda} \ (\text{m}^{-1}) \text{ or } \varepsilon$ $(\text{M}^{-1}\text{cm}^{-1})$
E1	A2	T1 Furnace and cell: Young [23]	500	CoF <sub>2</sub> 3 w%		NR	1	0.515 0.575	NR	NR	NR
E2	A3	Study: Young [24] Wavelength: 0.3 – 1.3 µm	650	CrF <sub>3</sub> 1.5 w%	FLiNaK	NR	1	0.45 0.69	NR	NR	NR
E3	Al	T2 Furnace and cell: Young [23] Study: Young [24] Wavelength: 0.3 – 1.3 μm	500	NiF <sub>2</sub> 1 w%	FLiNaK	NR	0.5	0.35 0.44	NR	NR	NR
E4	A7	T3 Furnace: Young [23]  Cell: Young [25]  Study: Young [26]  Wavelength: 0.3 – 2 µm	525	NiF <sub>2</sub> 0.2 - 1.0 w%	FLiNaK	NiF <sub>6</sub> <sup>4-</sup>	NR	0.43	ε = 12	0.9	$ \epsilon = 2.1 \\ 0.9 $
E5	A13	T4 Furnace:	540	FeF <sub>2</sub>		FeF <sub>6</sub> <sup>4</sup> -		NR	NR	1.04 1.72	$ \begin{aligned} \varepsilon &= \\ 4.8 \\ 3.0 \end{aligned} $
E6	A14	Young [27] Cell: Young [25]		NiF <sub>2</sub>	FLiBe	NiF <sub>6</sub> <sup>4-</sup>	NR	0.44	ε = 11.2	0.92 1.62	$ \epsilon = 1.3 \\ 0.8 $
E7	A15	Study: Young [29]	550	CrF <sub>2</sub>	rlibe	CrF <sub>6</sub> <sup>4-</sup>	NK	0.71	ε = 5.9	NR	NR
E8	A16	Wavelength: 0.3 – 2.3 μm		CrF <sub>3</sub>		CrF <sub>6</sub> <sup>3-</sup>		0.3 0.45 0.69		NR	NR
E9		T9 Furnace: Young [27]	525	$Te_2(g)$		NR		0.41	NR	NR	NR
E10	A20	Cell and study: Bamberger [38]  Wavelength: 0.25 – 0.7 µm	600	LiTe <sub>3</sub> Li <sub>2</sub> Te +oxidants	FLiBe	Te <sub>3</sub> -	1	0.478	NR	NR	NR

E11	A21	T10 Furnace:		NaO <sub>2</sub>		$O_2$		0.254	NR	NR	NR
E12	A22	Young [27] Cell and study: Whiting [39]	500	K <sub>2</sub> CrO <sub>4</sub> ∼13 wppm	FLiNaK	CrO <sub>4</sub> <sup>2-</sup> (Cr <sup>6+</sup> valen ce state)	1	0.265 0.372	$ \begin{aligned} \varepsilon &= \\ 2940 \\ 3970 \end{aligned} $	NR	NR
E13	N/A	Wavelength: 0.2 – 0.5 μm		KNO <sub>2</sub>		NO <sub>2</sub>		0.365	NR	NR	NR
E14	A23	T7 Furnace: Young [27]		MnF <sub>3</sub>		MnF <sub>6</sub> <sup>3</sup>		0.525	NR	NR	NR
E15	A24	Cell and study: Whiting [35]	500	MnF <sub>2</sub> ~5.6 w%	FLiNaK	MnF <sub>6</sub> <sup>4</sup>	NR	0.408	$\varepsilon = 0.11$	NR	NR
E16	A25	Wavelength: 0.2 – 2 μm		CuF <sub>2</sub> ~0.5 w%		CuF <sub>6</sub> <sup>4</sup> -		NR	NR	0.88	ε = 11
E17	A27	T12 Furnace: Young [27] Cell and study: Toth [42] Wavelength: 0.3 – 2.5 μm	550	NiF <sub>2</sub>	FLiBe	NR	0.635	0.45	NR	0.92 1.72	NR NR
E18	A35	T13 Furnace: Toth [44]  Cell: Toth [42]  Study: Toth [47]  Wavelength: 0.25 – 3.4 µm	550	NbF <sub>4</sub> 0.068 M 0.113 M 0.202 M 0.303 M	FLiBe	NbF <sub>7</sub> <sup>3</sup>	NR	0.38 0.51 0.74	NR	1.82	NR
E19	N/A	T13 Furnace: Toth [44] Cell: Toth [42] Study: Toth [48]	550 − 600 °C	Li <sub>2</sub> Te +oxidants	FLiBe	Te <sup>-</sup> (or likely same specie s as E10)	.635	0.478	ε = 3370	NR	NR
E20	A43	T17 Furnace:		CrF <sub>2</sub> 0.2 w%		NR		0.75	NR		
E21	A43 A44	H. Liu [51]  Cell and study: Y. Liu [52]	NR	CrF <sub>3</sub> 0.2 w%	FLiBe	NR	10	0.31 0.45	$\kappa_{\lambda} = 20^{*}$ $75^{*}$ $70^{*}$	NR	NR
E22	A44	Wavelength: 0.35 – 0.85 μm		CrF3 0.35 w%		NR		0.43	$\kappa_{\lambda} = 35^{*} \\ 132^{*} \\ 92^{*}$		

E23				CrF <sub>3</sub> 0.5 w%		NR			$\kappa_{\lambda} = 62^{*} \\ 240^{*} \\ 215^{*}$		
E24	A45			CrF <sub>2</sub> 0.2 w%	- FLiNaK	NR		0.45 0.7 0.75	NR	- NR	NR
E25	A43			CrF <sub>3</sub> 0.2 w%	FLINAK	NR		0.45 0.7	NR	INK	INK
E26	A63		1377	CoF <sub>2</sub> 0.075 mol%	CaF <sub>2</sub>	CoF <sub>6</sub> <sup>3-</sup>		0.36 0.38 0.39 0.41 0.43 0.49 0.53	NR	0.89	NR
E27	A64	R7	1027	FeF <sub>3</sub> 0.51 mol%	BeF <sub>2</sub>			0.31 0.34 0.36 0.38 0.41 0.61	NR	0.92	NR
E28	A65	Setup and study: Khokhryakov [80] Wavelength: 0.23 – 1.03 µm	827	FeF <sub>3</sub> 10 w%	BeF <sub>2</sub> <sup>R</sup>	FeF <sub>6</sub> <sup>3-</sup>	NR	0.24 0.26 0.29 0.32 0.35 0.36 0.38 0.41 0.43 0.56	NR	0.95	NR
E29	A66		727		NaF <sup>R</sup>			0.26 0.30 0.41	NR	0.85 0.93	NR

<sup>\*</sup> the solvent background has been subtracted from the solute NR indicates the parameter was not reported

Table 8. Measurements of electronic absorption for lanthanides and actinides. Details on the setup used can be found by looking up the Setup Number (e.g., T#, R#) in Table 1 and Table 4. Plots can be found in the supplemental material.

				Composition			2.1		le Peaks .8 μm)		red Peaks 0.8µm)
Spectrum #	Plot #	Method	Temp (°C)	Solute	Solvent	Speciat ion	Path Length (cm)	Peak Location (µm)	Peak intensity $\kappa_{\lambda}$ (m <sup>-1</sup> ) or $\varepsilon$ (M <sup>-1</sup> cm <sup>-1</sup> )	Peak Locatio n (μm)	Peak intensity $\kappa_{\lambda}$ (m <sup>-1</sup> ) or $\varepsilon$ (M <sup>-1</sup> cm <sup>-1</sup> )
E30	A4	T1 Furnace and cell: Young [23]	550	Pr fluoride <5 w%	EL N. V.	NR	0.8	0.44 0.47 0.48 0.58	NR	NR	NR
E31	A5	Study: Young [24] Wavelength: 0.3 – 1.3 µm	570	UF <sub>4</sub> 1.66 w%	FLiNaK	NR	NR	0.44 0.48 0.55 0.62 0.69	NR	0.89 1.1 1.34	NR

<sup>&</sup>lt;sup>R</sup> indicates reflectance was measured and correlated to absorbance

E32	A6		575	UO <sub>2</sub> F <sub>2</sub> <1.7 w%		NR	NR	0.43	NR	NR	NR
E33	A8 A9	T4 Furnace and study:	50	UF <sub>4</sub>	FLiBe			0.24 0.49 0.52 0.61 0.64	$\varepsilon = 1400$ 3.8 3.2 <sup>sh</sup> 5.2 <sup>sh</sup> 6.4	0.86 1.1 1.38	$ \begin{aligned} \varepsilon &= \\ 1.8^{\text{sh}} \\ 13 \\ 0.7 \end{aligned} $
E34	A10	Young [27] Cell: Young [25]	30	UF <sub>3</sub>		UF <sub>8</sub> <sup>4-</sup> UF <sub>9</sub> <sup>5-</sup>	0.7	0.36 0.73 0.82	$ \begin{aligned} \varepsilon &= \\ 430 \\ 12 \\ 32^{\text{sh}} \end{aligned} $	0.87 0.96 1.03 1.16	$\varepsilon = 42$ 24 24 21
E35	All	Wavelength: 0.2 – 1.4 µm	525	UF <sub>3</sub>	FLiNaK			0.44 0.72	$ \varepsilon = 420 $ $ 32sh $	0.83 0.89 0.97 1.06 1.16	$\varepsilon = 31^{sh}$ 43 28 26 25
E36	A12	T7 Furnace: Young [27] Cell: Whiting [35] Study: Young [36] Wavelength: 0.3 – 0.6 µm	540	UF <sub>3</sub>	LiF- BeF <sub>2</sub> - ZrF <sub>4</sub> (66- 29-5 mol%) + 2 w% UF <sub>4</sub>	NR	NR	0.36	NR	NR	NR
E37	A17 A18	T5 Furnace: Young [27] [30] Cell: Young [25] Study: Young [31] Wavelength:	570	PaF <sub>4</sub>	LiF- BeF <sub>2</sub> - ThF <sub>4</sub> (72-16- 12 mol%)	PaF <sub>7</sub> <sup>4-</sup>	NR	0.26 0.33	ε = 694 624	1.58 1.83	NR
E38		0.3 – 2.3 μm T8 Furnace:	498						ε = 16.4		$\varepsilon = 8.0$
E39		Young [27] Cell and study:	560						ε = 14.4		$\varepsilon = 7.3$
E40	N/A	Bamberger [37]	650	UF <sub>4</sub>	FLiBe	NR	NR	0.64	ε = 13.8	1.09	ε = 6.2
E41		Wavelength: 0.64, 1.09 μm	698						ε = 12.9		ε = 5.7
E42	A19	T5 Furnace: Young [27] [30] Cell: Young [25] Study: Bamberger [32] Wavelength:	575	PuF <sub>3</sub> 0.4 mol%	LiF- BeF <sub>2</sub> - ThF <sub>4</sub> (72-16- 12 mol%)	NR	NR	0.42 0.43 0.45 0.5 0.56 0.66	NR	0.81 0.89 1.06 1.34 1.44	NR

		0.4 – 1.8 μm									
E43	A28	T12 Furnace: Young [27] Cell and study: Toth [42] Wavelength: 0.3 – 2.5 μm	550	UF <sub>4</sub>	FLiBe	NR	0.635	0.53 0.6 0.65	NR	0.85 1.1 1.42 2.03	NR
E44	A29		550	UF <sub>4</sub>	FLiNaK	UF <sub>8</sub> <sup>4-</sup>		0.43 0.44 0.47 0.53 0.61 0.66	$\varepsilon = 4.4^{sh}$ $4.5^{sh}$ $6.2$ $4.4$ $8.5^{sh}$ $11$	1.1 1.41 1.61 2.13	$\varepsilon = 20.8$ 5.2 3.8sh 3.8
E45	A30	T12 Furnace: Young [27] Cell: Toth	460	UF <sub>4</sub>	FLiBe	UF <sub>8</sub> <sup>4-</sup>		0.43 0.44 0.47 0.53 0.61 0.66	$\varepsilon = 3.6^{sh}$ $4.6^{sh}$ $5.2$ $3.9$ $6.2^{sh}$ $9.2$	1.1 1.41 1.61 2.13	$\varepsilon = 18.2$ 5.2 4.2sh 3.4
E46		[42] Study: Toth	690	UF <sub>4</sub>		UF <sub>7</sub> <sup>3-</sup>	0.63	0.44 0.49 0.52 0.63	$\varepsilon = 3.8^{sh}$ 4.1 3.2 <sup>sh</sup> 6.6	1.08 2.02	$ \varepsilon = 14.4^{+} $ $ 2.8^{+} $
E47	A31	Wavelength: 0.4 – 2.5 μm	360	UF <sub>4</sub>	LiF- BeF <sub>2</sub> (48-52	UF <sub>8</sub> <sup>4-</sup>		0.43 0.44 0.47 0.53 0.61 0.66	$\varepsilon = 3.6^{\text{sh}}$ $4.6^{\text{sh}}$ $5.2$ $4.1$ $7.2^{\text{sh}}$ $9.5$	1.1 1.41 1.61 2.13	$\varepsilon = 18.9 \\ 6.7 \\ 5.0$ <sup>sh</sup> $4.4$
E48			690	UF <sub>4</sub>	mol%)	UF <sub>7</sub> <sup>3-</sup>		0.44 0.49 0.52 0.63	$\varepsilon = 3.2^{\text{sh}}$ 3 2.6 <sup>sh</sup> 5.6	1.08 2.02	$ \epsilon = 12.4 \\ 3.7 $
E49	A32 A33	T13 Furnace and	NR	UF <sub>3</sub>				0.32 0.36 0.43 0.71	$\varepsilon = 740$ 840 600 <sup>sh</sup>	0.87 0.96 1.04 1.14 2.14	$\varepsilon = 43$ 22 22 20 12
E50		study: Toth [44]	500					NR	NR	0.88 1.09	NR
E51	A34	Cell: Toth [42]	600	UF <sub>3</sub> UF <sub>4</sub>	FLiBe	NR	0.63	0.71	NR	1.6 0.88 0.96 1.04 1.09 1.14	NR
E52		μш	700					0.71	NR	0.88 0.96 1.04 1.14	NR

					EI :D						
E53	N/A	T13 Furnace: Toth [44]  Cell: Toth [42]  Study: Gilpatrick [46]	500 - 800	UF <sub>3</sub>	FLiBe  LiF- BeF2 (48-52 mol%)  LiF- BeF2 (57-43 mol%)  LiF- BeF2- ThF4 (72-16-12 mol%)	NR	NR	0.36	$\varepsilon = 11,001$	NR	NR
E54	A42	T16 Furnace and study: H. Liu [51] Cell: S. Liu [50] Wavelength: 0.2 – 1.0 µm	600	UF <sub>4</sub> 0.5 w%	FLiBe	NR	10	0.27 0.45 0.48 0.52 0.64	NR	NR	NR
E55	A62	R7 <sup>a</sup> Setup: Khokhryako v [84][80]	667	CeF <sub>3</sub> 0.0304 mol%	LENE	CeF <sub>6</sub> <sup>3-</sup>	1	0.23 0.26 0.29	NR	NR	NR
E56	A02	Study: Khokhryako v [81] Wavelength: 0.21 – 0.33	007	Ce <sub>2</sub> O <sub>3</sub> 0.0185 mol%	LiF-NaF	CeOF <sub>5</sub> <sup>4</sup>	1	0.23 0.25 0.29	NR	NR	NR
E57		R7 Setup:			LiF	D T 3		0.34 0.44 <sup>b</sup> 0.47 0.48 0.55 0.59	NR	1.53	NR
E58	A67	Khokhryako v [80] Study: Khokhryako v [82]	1000	PrF <sub>3</sub> 0.7 mol%	NaF	PrF <sub>6</sub> <sup>3-</sup>	NR	0.38 0.45 0.48 0.59	NR	1.5	NR
E59		Wavelength: 0.24 – 1.67 μm			KF	PrF <sub>6</sub> <sup>3-</sup> PrOF <sub>5</sub> <sup>4-</sup>		0.33 0.38 0.48 0.58	NR	1.52	NR

E60					CsF			0.35 0.41 <sup>b</sup>	NR	0.85 0.89 1.52	NR
E61	A68		750 800 1000	PrF <sub>3</sub> 0.71 mol%	FLiNaK	- PrF <sub>6</sub> <sup>3</sup> -	NR	0.33 0.44 0.47 0.48 0.59 0.64	NR	1.53	NR
E62	A69		500	PrF <sub>3</sub> 20.01 mol%	FLiNaK R		NR	0.27 0.40 0.50 0.54 0.64	NR	0.95 1.18	NR
E63	A70		1000	Pr <sub>2</sub> O <sub>3</sub> 0.15 mol%	LiF	PrOF <sub>5</sub> <sup>4-</sup>	NR	0.34 0.54 0.8	NR	1.24	NR
E64	A71	R7 Setup: Khokhryako v [80] Study: Khokhryako v [83] Wavelength: 0.24 – 0.38	1000	GdF <sub>3</sub> 0.9 mol% initial	- LiF	GdF <sub>6</sub> <sup>3</sup> -	NR	0.26 0.28 0.34	NR	NR	NR
E65				GdF <sub>3</sub> 0.9 mol% steady			NR	0.27 0.3	NR	NR	NR
E66				GdF <sub>3</sub> 1.4 mol%	NaF		NR	0.25 0.27 0.31	NR	NR	NR
E67				GdF <sub>3</sub> 2 mol%	KF		NR	0.32	NR	NR	NR
E68				GdF <sub>3</sub> 5 mol%	CsF		NR	0.3	NR	NR	NR

E69		GdF <sub>3</sub> 3.9 mol%	NaF-CsF	NR	0.3	NR	NR	NR

shindicates a shoulder rather than a sharp peak

#### 5. STRUCTURAL INTERPRETATION

Here we summarize and discuss absorption data from prior optical spectroscopy studies (mostly in the infrared and visible range) on fluoride salts. The data has been divided into two sections based on the physics of the resonance causing absorption to occur at a particular wavelength. First, we summarize and discuss vibrational data, starting with solvents in section 5.1.2 and followed by solutes in 5.1.3. Then, we summarize and discuss electronic data of solutes, starting with lighter elements (mostly transition metals) in section 5.2.2 followed by heavier (lanthanides and actinides) in section 5.2.3.

## 5.1. Vibrational Absorption – NIR/MIR/FIR

## 5.1.1. Background

Vibrational resonance occur when atoms bound by a restoring force, such as an ionic or covalent bond, are excited by an incoming photon with a frequency that matches the natural vibrational frequencies of the bond. Within a molten fluoride environment, ionic interactions are expected to dominate due to the large electronegativity differences between F and the alkali and alkaline earth metals that typically make up a solvent mixture. These interactions typically occur between a single cation surrounded by multiple anions, a structure referred to as the ion's first coordination shell. The coordination number (CN) is the number of ions within the first coordination shell, typically defined relative to a specific cation. This structure leads to collective vibration similar to that seen in the solid-state, but of shorter range, leading some authors to refer to the melt structure as a 'quasilattice' [66][74].

It is useful to classify these ionic interactions or 'bonds' by their lifetime, as the melt structure is clearly dynamic. Alkali fluoride mixtures exhibit bonding at a sub-picosecond time interval (though intermediate range ordering has been observed at slightly longer time-scales) [87], and we refer to them as consisting of dissociated ions.

A longer time scale on the order of 10-100 ps is expected for bonding in alkaline-earth (or other multi-valent) fluorides, as predicted via molecular dynamics (MD) modeling of FLiBe [88][89]. These species will be referred to as associated monomers (e.g., BeF<sub>4</sub><sup>2-</sup>) and oligomers (e.g., Be<sub>2</sub>F<sub>7</sub><sup>3-</sup>, etc.). As the concentration of alkaline earth (or other multi-valent ions) ions is increased, formation of F- bridging

NR indicates the parameter was not reported

<sup>\*</sup> the solvent background has been subtracted from the solute

<sup>&</sup>lt;sup>R</sup> indicates reflectance was measured and correlated to absorbance

between two metal cations is increasingly favored, leading to oligomer formation and in some cases large chains or networks of ions [88][90].

#### 5.1.2. Solvents

#### 5.1.2.1. Resonance data

We refer to the region of peak absorption as the vibrational absorption resonance region. Vibrational absorption resonance data is available for the mixtures LiF-KF, LiF-NaF, LiF-KF-ZrF<sub>4</sub>, LiF-NaF-ZrF<sub>4</sub>, FLiBe, and compounds LiF and CsF. In Table 6 we compile the available data, providing an index (V#) for each spectrum, and reference the plot (A#) and setup indices (T# or R#). For each spectrum, we give the measurement temperature, salt composition, deduced speciation, and list the location and intensity of the various peaks or shoulders.

#### Dissociated melts

Mead studied the vibrational absorption of LiF and compared with high temperature crystalline spectra [66], shown in Figure 5a. Crystalline LiF displays a relatively sharp, high-intensity peak at 32  $\mu$ m and a shoulder at 20  $\mu$ m (Table 6, V64) [65], whereas Mead's data for liquid LiF displays a much broader, lower-intensity peak at 21.5  $\mu$ m. Using an oscillator model, Mead attributed the peak broadening and intensity reduction upon melting to be due to increased damping caused by loss of long-range order [66]. We note the discrepancy with Wilmshurst's liquid LiF data [74] which shows a sharper, lower-intensity peak at 17.75  $\mu$ m. Mead thought this to be due to KK integration error or temperature differences, as Wilmshurst's wavelength range was much shorter, and the measurement temperature was not reported.

In addition to LiF, Wilmshurst studied LiF-KF mixtures over various compositions [74], shown in Figure 5b. The spectra of the mixtures are approximately a superposition of the peaks for the pure components; however, the LiF peak shifts slightly from 17.75 μm to 18.75 μm, does not diminish proportionally as the LiF concentration decreases, and a secondary peak appears at about 21.5 μm. Wilmshurst explained the apparent preference for Li-F vibrations as 'typical of the spectra of highly associated liquids exhibiting quasilatticelike behavior', without giving much further discussion, and the 'doublet' nature of the LiF peak was attributed to 'anharmonicity'. Superposition behavior is also seen in Raman spectra LiF-KF and LiF-CsF mixtures [91] and an additional peak was observed and attributed to an intermediate-range (LiF<sub>x</sub>)K or (LiF<sub>x</sub>)Cs species having short lifetimes (between 0.1 and 1 ps). LiF-KF exhibits a type II Chemla Effect, meaning that the ionic mobilities of both the smaller and larger cations decrease with increasing concentration. Ribiero used rigid-ion MD to investigate this, revealing the presence of intermediate-range Li species [87], and Salanne confirmed the result using polarizable-ion MD [92]. High-temperature pulsed-field-gradient NMR spectroscopy (HT-PFG-NMR) was performed on LiF-

KF mixtures, and it was concluded that the melt was completely dissociated and no direct evidence of intermediate structures was found; however, their presence couldn't be ruled out, since the NMR characteristic time is long relative to the short-lived species [93]. It is possible that the behavior observed by Wilmshurst is evidence of intermediate-range Li species, and further experimental and theoretical work in this area would be quite interesting.

FLiNaK or LiF-NaF-KF (46.5-11.5-42 mol%) is an example of a mixture expected to consist of dissociated ions. Its structure has been fairly well documented by MD [94], x-ray diffraction (XRD) [95], and a combined MD and neutron diffraction approach [96]. The XRD-determined cation-anion average bond distances and CN found in molten FLiNaK are near the values obtained for the single-component melts, a result consistent with the vibrational data of alkali fluoride mixtures discussed above. The results of the two computational approaches agree with experimental for average cation-anion bond distances, but the computational-derived CNs are slightly higher than the experimental values. This discrepancy could be due to differences in how CN is calculated, or other methodological differences. Raman measurement of FLiNaK has also been performed and the melt was interpreted as being completely dissociated [52]. There is no infrared vibrational absorption data for FLiNaK, but Wilmshurst's LiF-KF data (Figure 5b) suggests that the ternary mixture FLiNaK would appear as a superposition of the individual constituent peaks, with a weighting towards the LiF peak.

Infrared resonance data for alkali fluoride melts are consistent with results from other techniques, which suggest that absorption is due short-lifetime bonds between cations and anions in the first-coordination shell. Further study would be of interest to understand the potential contribution of intermediate-range Li species.

#### Associated melts

Wilmshurst also studied mixtures of ZrF<sub>4</sub> with LiF-KF (Figure 4, Plot A47, V40) and various compositions with NaF-KF [74], shown in Figure 5c. At the highest ZrF<sub>4</sub> concentration (NaF-KF-ZrF<sub>4</sub>), a sharp, high-intensity peak is displayed at 19.2 μm. As ZrF<sub>4</sub> concentration decreases, this peak reduces intensity and shifts slightly to 19-20 μm as a secondary peak or shoulder appears at 21.5 μm. At the lowest ZrF<sub>4</sub> concentration (5NaF-5KF-ZrF<sub>4</sub>), only one peak at 20.5 μm remains. Wilmshurst attributed this peak transition (from about 19 to 21 μm) to the breakdown of a Zr<sup>4+</sup> polymeric lattice into Zr<sup>4+</sup> monomers, suggesting either ZrF<sub>6</sub><sup>2-</sup> or ZrF<sub>5</sub><sup>-</sup> monomeric species. Recently, a combined study using MD, high-temperature NMR (HT-NMR), and extended x-ray absorption fine structure (EXAFS) was performed of LiF-ZrF<sub>4</sub> mixtures [97]. NMR spectra reveal a relatively sharp transition in the <sup>19</sup>F chemical environment going from dilute ZrF<sub>4</sub> to about 33 mol% followed by a slower transition going to 50 mol%, which correlates well with the MD-determined amount of bridging F. EXAFS and MD-determined CN's are a

mixture of 6, 7 and 8. The similarity with Wilmshurst's conclusions regarding degree of bridging (i.e. oligomer formation) suggests that ZrF<sub>4</sub> may behave similarly in mixtures of varying alkali fluoride composition. We note that Wilmshurst chose to avoid mixtures of LiF and ZrF<sub>4</sub> due to peak overlap.

FLiBe is an example of a melt which consists of dissociated ions in the form of Li<sup>+</sup>, associated monomers in the form of BeF<sub>4</sub><sup>2-</sup>, and associated oligomers present as chains of tetrahedral BeF<sub>4</sub><sup>2-</sup>. The structure of FLiBe has been studied by several MD approaches [88][89][98] and experimentally via Raman spectroscopy [67][68] and XRD [99]. BeF<sub>4</sub><sup>2-</sup> and larger (e.g., Be<sub>2</sub>F<sub>7</sub><sup>3-</sup>, etc.) structures have been found in broad agreement across the various approaches. There is no quantitative vibrational absorption resonance data for FLiBe, but qualitative transmittance spectra are available of a thin melt [50], shown in Figure 5d. The dominant peak appears at about 12.5 μm, and was attributed to BeF<sub>4</sub><sup>2-</sup> via quantum-chemical density-functional-theory (QC-DFT). This peak is also observed as an infrared-active Raman band in molten FLiBe and the infrared spectra of crystalline FLiBe powder (Table 6, V72-73) [67]. The crystalline data suggest that another resonance would be found at about 22 μm, corresponding to vibration between Li<sup>+</sup> and BeF<sub>4</sub><sup>2-</sup> ions. Another small peak at 6.25 μm was observed by Liu and attributed as an overtone, but it could be due to larger Be<sup>2+</sup> oligomers, such as Be<sub>2</sub>F<sub>7</sub><sup>3-</sup>, as a similar infrared-active peak was observed in a Raman study of molten FLiBe[68].

Infrared resonance data for ZrF<sub>4</sub>-containg salt indicates a transition from monomers to an oligomer network as ZrF<sub>4</sub> concentration increases, in agreement with other techniques. More infrared resonance data for FLiBe or other associated fluoride melts (e.g., cryolite) would be useful to probe network-forming behavior.

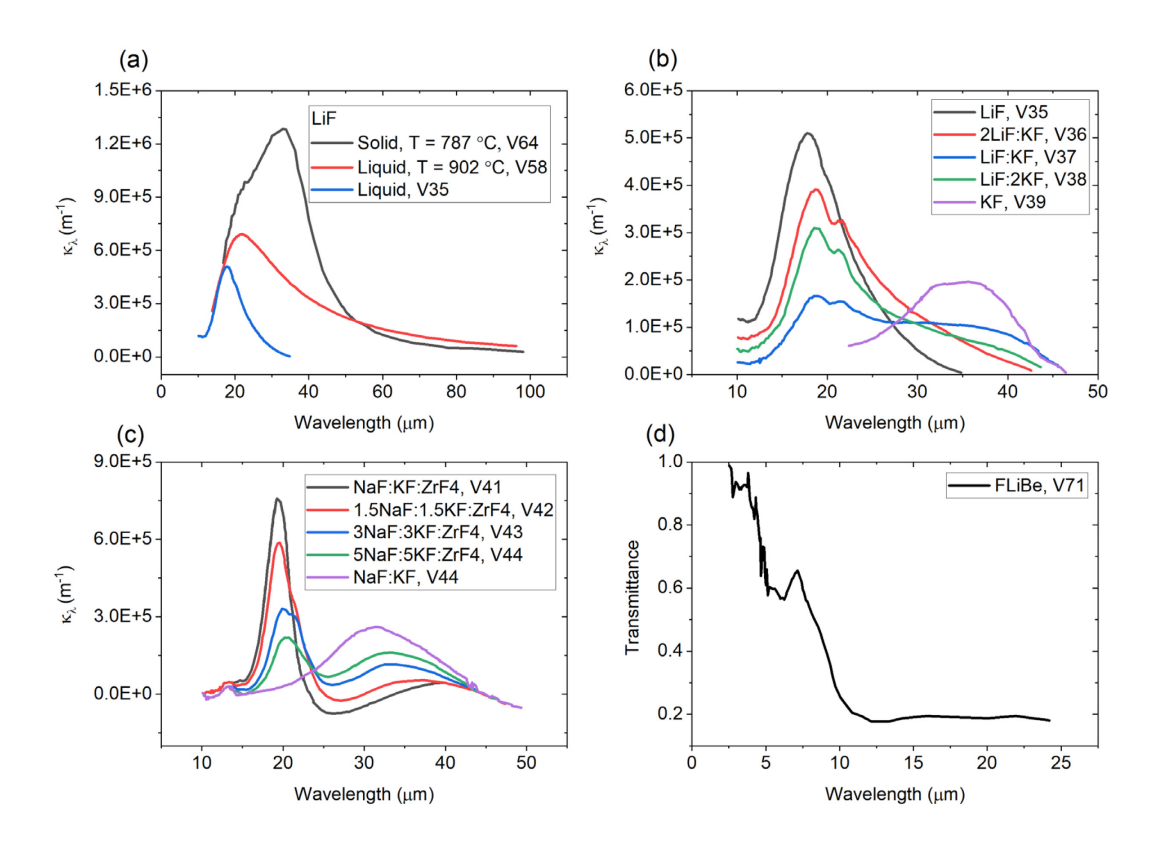


Figure 5. Vibrational absorption resonance spectra of molten fluoride solvents: (a) LiF, (b) LiF:KF mixtures, (c) NaF:KF:ZrF4 mixtures, (d) FLiBe. We give the spectrum index (V#) for each curve, for reference in Table 6. The negative values seen for k in (c) are due to KK integration errors, which we discuss in section 3.2.1.1.

### 5.1.2.2. Edge Data

The infrared absorption edge region for a given species occurs as the resonance region is approached and consists of rapidly rising  $\kappa_{\lambda}$  values. NIR edge data is available for LiF, CaF<sub>2</sub>, BaF<sub>2</sub>, and FLiBe. FIR edge data is also available for LiF. The NIR edge of FLiNaK has not been measured, but Chaleff predicted  $\kappa_{\lambda}$  (V34) by averaging high-temperature crystalline data for LiF and NaF, neglecting KF [9]. For each of the spectra, we define the edge location as the wavelength at which  $\kappa_{edge} = 100 \text{ m}^{-1}$ . In Table 5 we compile the available edge data, providing an index (V#) for each spectrum, and reference the plot (A#) and setup indices (T# or R#). For each spectrum, we give the measurement temperature, salt composition, path length, and edge location.

Varlamov noted that the edge of CaF<sub>2</sub>, BaF<sub>2</sub>, and LiF shifts to shorter wavelengths with increasing temperature and with the solid-to-liquid phase transition [49], but did not comment further on the behavior. Barker noted a similar shift with LiF, shown in Figure 6a, and interpreted it as peak broadening due to increased lattice disorder with increasing temperature [78]. This NIR shifting is expected to cause the

absorption edge of liquid alkali fluorides and alkali fluoride mixtures to approach the region of RHT significance, especially if LiF is a major constituent. More data is needed to characterize the degree to which peak broadening continues as temperature increases further into the liquid state.

Liu measured the NIR edge transmittance of FLiBe (Figure 4, Plot A39, V24) [50], and using the reported path length we present it as  $\kappa_{\lambda}$ , shown in Figure 6b. We note that the large peak about 2.8  $\mu$ m is due to OH<sup>-</sup> absorption and discuss this in section 5.1.3. More NIR edge measurements of both FLiBe and FLiNaK over a larger wavelength range are needed to quantify the degree of shifting which occurs with varying temperature in these solvents.

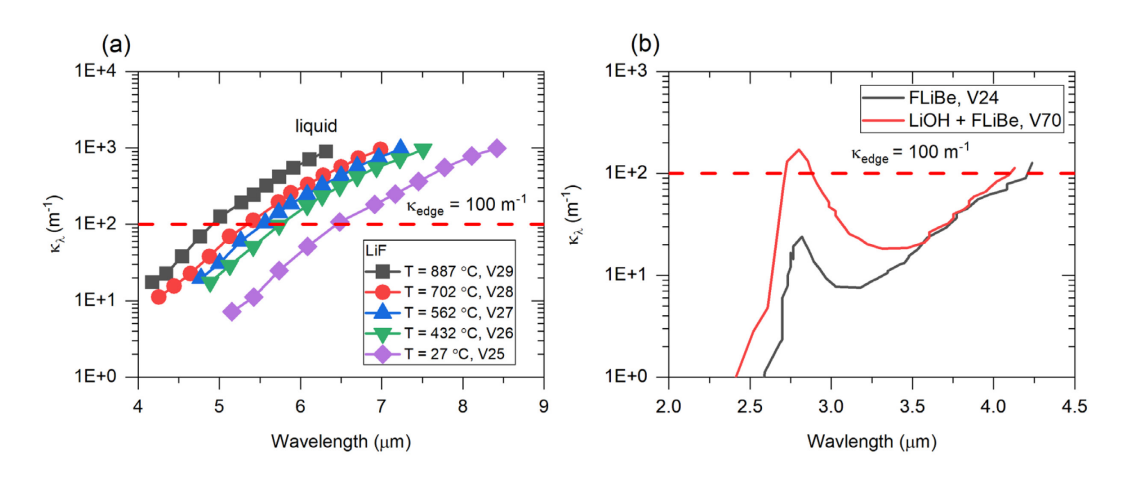


Figure 6. Vibrational absorption edge spectra of molten fluoride solvents: (a) LiF, (b) FLiBe. We give the spectrum index (V#) for each curve, for reference in Table 5. We note that (b) also contains solute vibrational absorption resonance data for LiOH in FLiBe solvent, which is referenced in Table 6.

#### 5.1.3. Solutes

Vibrational absorption resonance data is available for the solutes OH<sup>-</sup> in FLiBe, OD<sup>-</sup> in NaBF<sub>4</sub>, Ta<sup>5+</sup> in LiF-KF and LiF-NaF, and Nb<sup>5+</sup> in LiF-KF and FLiNaK. In Table 6 we compile the available data, providing an index (V#) for each spectrum, and reference the plot (A#) and setup indices (T# or R#). For each spectrum, we give the measurement temperature, salt composition, deduced speciation, and list the location and intensity of the various peaks or shoulders.

Addition of LiOH to FLiBe resulted in a large peak at about 2.8 μm (Figure 6b), suggesting the presence of O-H bonding. Similarly, the addition of D<sub>3</sub>BO<sub>3</sub> to NaBF<sub>4</sub> resulted in a peak at about 3.7 μm (Figure 4, Plot A26, V69), indicating the presence of O-D bonding. These results suggest that NIR/MIR measurements could be used to detect OH<sup>-</sup> and OD<sup>-</sup> contaminants.

Via comparison with crystalline  $K_2TaF_7$  and  $CsTaF_6$ [75], Fordyce theorized that  $Ta^{5+}$  existed as  $TaF_7^{2-}$  in LiF-KF, and a mixture of  $TaF_6^-$  and  $TaF_7^-$  in LiF-NaF [75], shown in Figure 7a. With the addition of  $H_2O$  in LiF-KF [77],  $Ta^{5+}$  was theorized to exist as  $TaOF_6^{3-}$  due to similarity with  $TaF_7^{2-}$  and the presence **60**|82

of a peak at about 11  $\mu$ m attributed to a Ta=O bond [100], also shown in Figure 7a. These interpretations have been partially validated by Raman results [101], in which the authors concluded that TaF<sub>5</sub> existed as TaF<sub>7</sub><sup>2-</sup> in FLiNaK. With some Na<sub>2</sub>O addition, TaOF<sub>5</sub><sup>2-</sup> was proposed to exist; larger Na<sub>2</sub>O additions resulted in a new species, presumed to be TaO<sub>2</sub>F<sub>4</sub><sup>3-</sup>. Another Raman and QC-DFT study inferred the presence of TaF<sub>7</sub><sup>2-</sup> and TaF<sub>8</sub><sup>3-</sup> in FLiNaK, and subsequently TaOF<sub>5</sub><sup>2-</sup>, TaOF<sub>6</sub><sup>3-</sup>, TaO<sub>2</sub>F<sub>2</sub><sup>-</sup>, and TaO<sub>2</sub>F<sub>3</sub><sup>2-</sup> as Li<sub>2</sub>O was added [102]. More investigation in this area is needed to resolve these discrepancies.

From comparison with crystalline spectra [76] and complementary Raman [103], NbF<sub>5</sub> was inferred to exist as NbF<sub>7</sub><sup>2-</sup> in LiF-KF (Figure 4, Plot A54, V52) [76] and FLiNaK [54], shown in Figure 7b. With the addition of Na<sub>2</sub>O to NbF<sub>5</sub> in FLiNaK, the species NbOF<sub>5</sub><sup>2-</sup> and subsequently NbO<sub>2</sub>F<sub>4</sub><sup>4-</sup> were inferred (Figure 4, Plot A67, V66-68). These results are in agreement with Raman measurements of Nb<sup>5+</sup> in FLiNaK with varying Na<sub>2</sub>O [103]. The formation of new species with addition of O<sup>2-</sup> to the melt indicates that both NbF<sub>5</sub> and TaF<sub>5</sub> could be used as marker species to detect the presence of O<sup>2-</sup>, as could several lanthanide fluorides (e.g., CeF<sub>3</sub>, PrF<sub>3</sub>, etc.).

Infrared resonance data for solutes in fluoride melts have been used to propose structures that are mostly in agreement with other techniques. The data has also shown the ability to distinguish vibrations related to O (e.g., OH<sup>-</sup>, Ta=O, oxy-fluoride species).

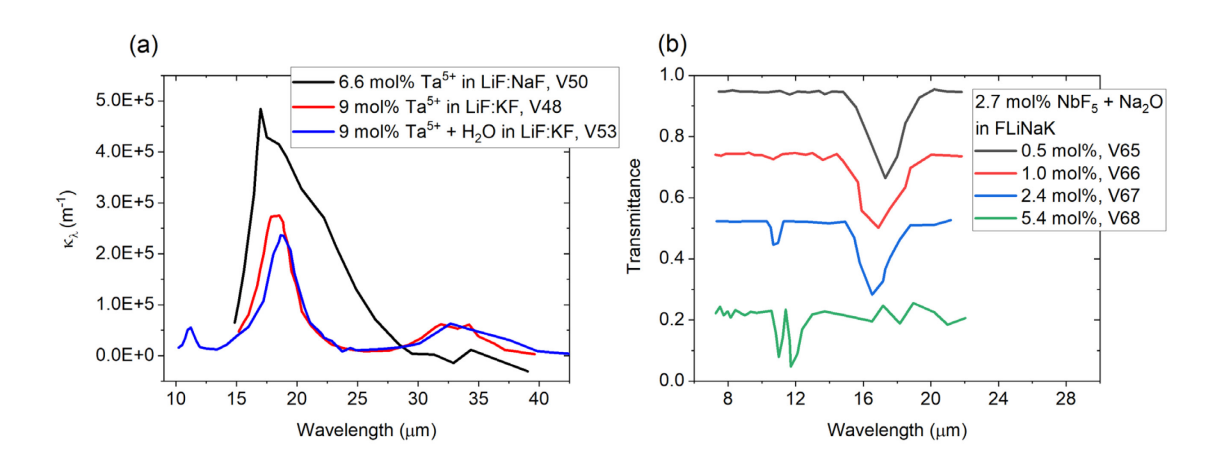


Figure 7. Vibrational absorption resonance spectra of solutes in molten fluoride solvents: (a) 6.6 mol%  $Ta^{5+}$  in LiF:NaF, 9 mol%  $Ta^{5+}$  in LiF:KF, and 9 mol%  $Ta^{5+}$  + H<sub>2</sub>O in LiF:KF (b) 2.7 mol% Nb<sup>5+</sup> in FLiNaK + varying amounts of Na<sub>2</sub>O. We give the spectrum index (V#) for each curve, for reference in Table 6. We performed a subtraction procedure (following the method presented by Fordyce [75]) to obtain the 9 mol%  $Ta^{5+}$  + H<sub>2</sub>O in LiF:KF curve in (a), but the data tabulated for entry V53 is un-subtracted. The negative values seen for k in (a) are due to KK integration errors, which we discuss in section 3.2.1.1.

## 5.1.4. Summary

Inferences from solvent vibrational absorption data are consistent with the distinction between melts of dissociated ions (fluorobasic) and associated monomers and oligomers (fluoroacidic). Intermediate 61|82

structure in Li-containing alkali fluoride mixtures could be an interpretation to 'doublet' peak behavior. Solvent and solute vibrational absorption data exhibit strong MIR resonances, resulting in NIR edges of significance to RHT in participating media. Inferences from solute vibrational absorption data are mostly consistent with more recent results and have been useful in identifying vibrations associated with oxygen.

## 5.2. Electronic Absorption – UV-Vis/NIR

## 5.2.1. Background

Molten fluoride salts consist of positively and negatively charged ions, each defined by a unique electronic configuration. Electronic resonance occurs when valence electrons (from the highest occupied energy orbital) are excited by an incoming photon with an energy that is equal to the difference in electronic energy levels between the valence orbital (ground state) and higher energy orbitals (excited states). In general, lighter elements (e.g., Li<sup>+</sup>, Be<sup>2+</sup>; both 1s<sup>2</sup>) have access to s and p orbitals which are separated by relatively large energies, requiring higher energy photons to excite and resulting in higher-energy electronic absorption bands in the UV and transparency in the visible spectrum. For example, Plot A1 shows the visible transparency of FLiNaK (UV cutoff attributed to the MgO cell) and Plots A39 and A43 show the NIR and visible transparency of FLiBe.

On the other hand, heavier elements have access to filled and unfilled d orbitals that are much closer in energy, resulting in lower energy absorption bands in the visible and NIR. For instance, the transition metal Cr<sup>3+</sup> (3d<sup>3</sup>) in FLiNaK and FLiBe has three peaks in the range of 0.30 to 0.69 um (Figure 4, Plot A3, E2; Plot A16, E8). As atomic weight increases, f orbitals can be accessed, further increasing the number of peaks, and the wavelength range expands through the NIR. For instance, in U<sup>4+</sup> (5f<sup>2</sup>) in FLiBe displays 10 peaks from 0.43 to 2.13 µm (Figure 4, Plot A30, E45-46).

## 5.2.2. Transition metals and Tellurium

Electronic absorption data is available for transition metals  $Ni^{2+}$ ,  $Cr^{2+}$ ,  $Cr^{3+}$ ,  $Fe^{2+}$ ,  $Fe^{3+}$ ,  $Co^{2+}$ ,  $Mn^{2+}$ ,  $Mn^{3+}$ ,  $Cu^{2+}$ , and  $Nb^{4+}$  in molten fluoride media<sup>1</sup>. Using crystal-field theory [104] and comparison with crystalline and aqueous spectra, interpretation of the solvation structure of the tabulated cations in various fluoride solvents was CN = 6 in all cases except for  $Nb^{4+}$ , which was CN = 7. In Table 7 we compile the available data, providing an index (E#) for each spectrum, and reference the plot (A#) and setup indices (T# or R#). For each spectrum, we give the measurement temperature, salt composition, deduced speciation, path length, and list the location and intensity of the various peaks or shoulders.

No complementary structural data from other experimental or modeling techniques were found,

<sup>&</sup>lt;sup>1</sup>Tl<sup>+</sup>, Pb<sup>2+</sup>, and Bi<sup>3+</sup> in FLiNaK were measured in the UV [128]. In this review, the focus has been on compiling data in the visible and infrared ranges due to their increased RHT relevance.

62|82

except for the  $Cr^{2+}$  and  $Cr^{3+}$  solute species which we further discuss in section 5.2.2.1. We then discuss the deduction of anionic Te speciation in section 5.2.2.2, as this is still a debated topic. At the time of publication, we found a recent study of FeF<sub>2</sub> in FLiNaK [105] which suggests intriguing dynamics, but this paper is not included in the review.

$$5.2.2.1.\ Cr^{2+}/Cr^{3+}$$

Ab initio molecular dynamics (AIMD) simulations have been performed on the  $Cr^{2+}$  and  $Cr^{3+}$  solutes in molten fluoride solvents [88][94][98]. Nam's results indicated that  $Cr^{2+}$  has CN = 5.2 in FLiBe and 4.9 in FLiNaK, and that  $Cr^{3+}$  has 5.9 in both solvents [98] Winner's results for  $Cr^{2+}$  showed predominantly CN = 4 and some CN = 5 and the results for  $Cr^{3+}$  dominantly showed CN = 6; similar coordination numbers were observed in three different solvents: FLiBe,  $3LiF-AlF_3$ , and 2KF-NaF [88]

Young measured the electronic absorption spectra of  $CrF_2$  in FLiBe (Figure 8a) and  $CrF_3$  in FLiBe (Figure 8a) and FLiNaK (Figure 4, Plot A4, E2) [29][24], and compared the various peak locations with crystal-field-theory calculations [106][107]. Due to agreement with the calculated peak locations, which had been obtained under the assumption of octahedral symmetry (i.e., CN = 6), Young concluded that  $Cr^{2+}$  and  $Cr^{3+}$  had CN = 6 in both FLiBe and FLiNaK [29]. Young also observed that the spectra of  $Cr^{2+}$  and  $Cr^{3+}$  did not exhibit spectral changes with varying LiF concentration (60-77 mol%) in LiF-BeF<sub>2</sub> mixtures. They argued that this reflected the consistency of the Cr coordination environment in solvents of varying fluoroacidity, an observation made by Winner [88] and nearly seen by Nam [98]. Furthermore, Young suggested that in FLiBe, Cr ions would be solvated by  $BeF_4^{2-}$  rather than compete with  $Be^{2+}$  for  $F^-$ , a result which was directly predicted by Winner. However, the interpretation of CN = 6 for  $Cr^{2+}$  in FLiBe disagrees with the AIMD results of both Nam and Winner. It would be valuable to revisit the interpretation of Young's spectral data using computational chemistry tools that were not available at the time of Young's study (1969). Since optical spectroscopy is an indirect indicator of CN, more direct structural data (e.g., from neutron diffraction, AIMD, etc.) would be useful to gain confidence in the structural interpretation of optical spectra and to address the discrepancies.

Liu performed a study aimed at understanding the differences in stability of Cr<sup>2+</sup> and Cr<sup>3+</sup> in FLiNaK and FLiBe, and the effect of CrF<sub>3</sub> on the corrosion of Cr metal. First, electronic absorption spectra of CrF<sub>2</sub> and CrF<sub>3</sub> in FLiBe were measured, shown in Figure 8c, both in agreement with Young's data (Figure 7a) [29]. Next, Cr metal was added to a solution containing FLiBe and CrF<sub>3</sub>, and a decrease in absorbance of the 450 nm peak and a shift from 700 to 750 nm was observed, implying the conversion of CrF<sub>3</sub> to CrF<sub>2</sub> via the following reaction.

$$3CrF_2 \leftrightarrow 2CrF_3 + Cr$$
 25

Following the investigation of FLiBe, the electronic absorption spectra of CrF<sub>2</sub> and CrF<sub>3</sub> in FLiNaK were

measured, shown in Figure 8d. The CrF<sub>3</sub> absorbance agreed with Young's data (Figure 4, Plot A3, E2) and looked similar to the FLiBe data; however, the CrF<sub>2</sub> absorbance looked markedly different from the FLiBe data, showing a peak at 450 nm in addition to a broad peak from about 600 to 750 nm. This behavior was interpreted as the conversion of CrF<sub>2</sub> to CrF<sub>3</sub> and Cr metal, further evidenced by the presence of Cr metal particles in the frozen salt after experimentation. Following the investigation of FLiNaK, CrF<sub>2</sub> was added to LiF-BeF<sub>2</sub> (2.25:1) and a similar reaction occurred. Liu concluded that CrF<sub>3</sub> becomes more favored as fluorobasicity, or dissociated F<sup>-</sup> concentration, increases.

This concept is further explored computationally for Cr<sup>0</sup>, Cr<sup>2+</sup> and Cr<sup>3+</sup> in [88], which demonstrates that besides dissociated F<sup>-</sup> and associated F<sup>-</sup>, bridging F<sup>-</sup> is also of importance, as solutes can be solvated by dissociated F<sup>-</sup> as well as by incorporation into solvent oligomers that consist of strongly-associated F<sup>-</sup> containing complex ions; it is hypothesized that steric hindrance makes the oligomer-solvation less prevalent for higher CN ions (Cr<sup>3+</sup> having a higher CN than Cr<sup>2+</sup>) [88]. This could explain the stability of Cr<sup>2+</sup> over Cr<sup>3+</sup> for fluoroacidic melts. Further study of the Cr<sup>2+</sup>, Cr<sup>3+</sup> equilibria are needed to understand more clearly how the equilibrium shifts with changes in temperature, fluoroacidity, and heterogeneous phases (e.g., Cr metal, Cr carbides, etc.). An example of such a study is provided by Toth [44], in which the equilibrium quotient of U<sup>4+</sup> and U<sup>3+</sup> with uranium carbides and graphite was measured over varying conditions, and we further discuss in section 5.2.3.2.

#### 5.2.2.2. Te<sup>-</sup>

Te was found in the MSRE as a fission product and caused embrittlement of structural alloys [108], and could pose issues due to its volatility. As opposed to the cationic transition metal ions, Te was studied in a negative oxidation state via addition of Li<sub>2</sub>Te. Bamberger [38] found that if purified Li<sub>2</sub>Te were added to pre-reduced FLiBe, there would be no absorption. If oxidants (e.g., Te<sub>2</sub>, FeF<sub>2</sub>) or the impurity LiTe<sub>3</sub> were present, a peak at 0.478 μm would appear, shown in Figure 8b. Measurement of Te<sub>2</sub> vapor resulted in a peak at about 0.41 μm, also shown in Figure 8b, ruling it out as the potential species. Moreover, Bamberger showed that the equilibrium concentration of dissolved Te<sub>2</sub> in FLiBe was immeasurable, resulting in a solubility estimate of 300 wppm at 525 °C. Thus, Bamberger concluded that Li<sub>2</sub>Te would convert to LiT<sub>3</sub> (n=1, m=5/2 in eq. 26) in oxidizing conditions.

Toth [48] criticized Bamberger's use of a SiO<sub>2</sub> cell (T9), arguing that it could act as an oxidant, and performed similar experiments with the diamond windowed cell (T12). Toth controlled the concentration of Te<sub>2</sub> in the melt with a thermal gradient furnace. The equilibrium reaction proposed by Toth is given in equation 26.

$$nLi_2Te + mTe_2 \leftrightarrow 2Te_{\left(\frac{n}{2}\right)+m}^{n-} + 2nLi^+$$

Through additions of different amounts of  $Te_2$ , Toth proposed that  $Te^-$  was present (n = 1, m =  $\frac{1}{2}$ ). Toth

reported that this behavior was consistent between fluoride and chloride solutions; however, spectral data was only given for chloride solution. Thus, more work is needed to study the tellurium solvation in fluoride salts and to provide conclusive evidence for the structure of the (-1) oxidation state of Te.

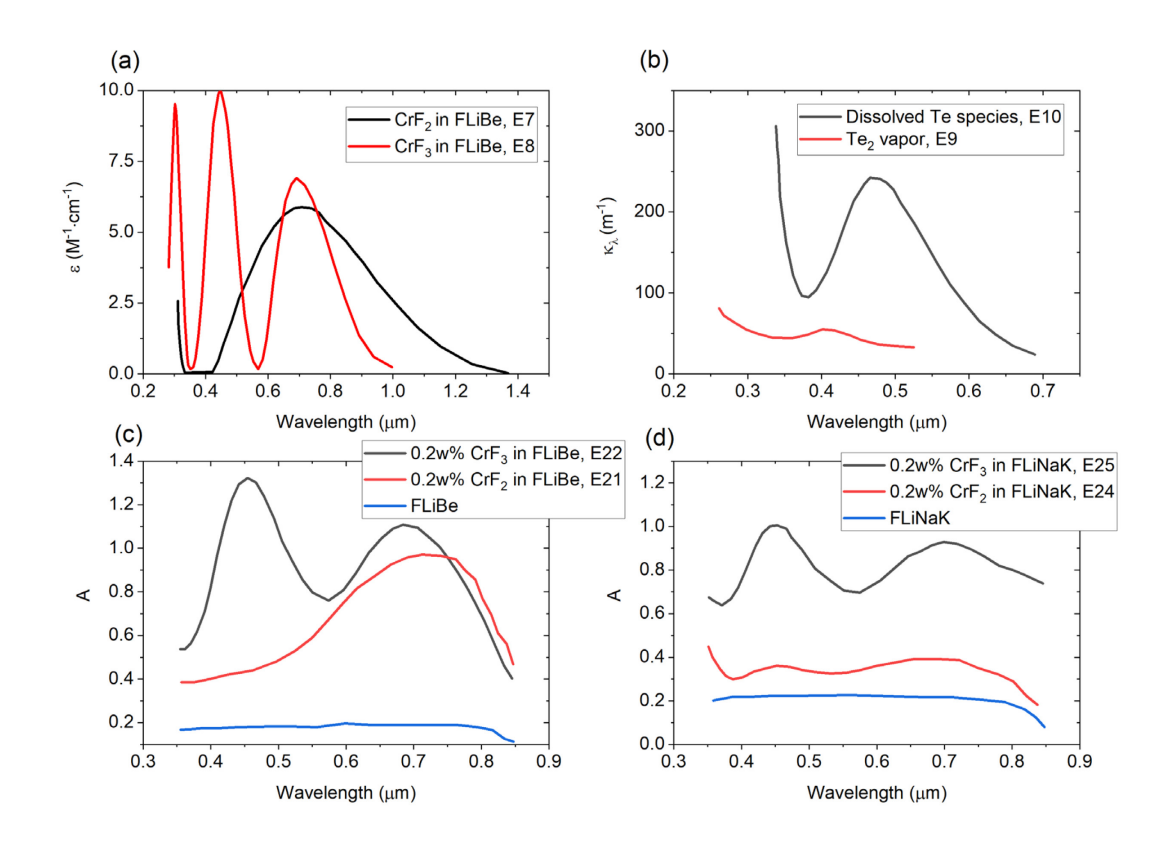


Figure 8. Electronic absorption spectra of lighter solutes in molten fluoride solvents: (a) molar absorptivity ( $\epsilon$ ) spectra of  $Cr^{2+}$  and  $Cr^{3+}$  in FLiBe, (b) linear absorption coefficient ( $\kappa_{\lambda}$ ) spectra of a dissolved Te species in FLiBe and Te<sub>2</sub> vapor, (c) absorbance resulting from additions of  $CrF_2$  and  $CrF_3$  in FLiBe, and (d) absorbance resulting from additions of  $CrF_2$  and  $CrF_3$  in FLiNaK . We give the spectrum index (E#) for each curve, for reference in Table 7.

#### 5.2.3. Lanthanides and actinides (f block)

Ce<sup>3+</sup>, Pr<sup>3+</sup>, Gd<sup>3+</sup> and Pa<sup>4+</sup>, U<sup>3+</sup>, U<sup>4+</sup>, Pu<sup>3+</sup> constitute the available lanthanide and actinide electronic absorption data in molten fluoride media. In Table 8 we compile the available data, providing an index (E#) for each spectrum, and reference the plot (A#) and setup (T# or R#). For each spectrum, we give the measurement temperature, salt composition, deduced speciation, path length, and list the location and intensity of the various peaks or shoulders.

### 5.2.3.1. Lanthanides

Using ligand field theory, Khokhryakov interpreted  $Ce^{3+}$  (Figure 4, Plot A62, E55-56) [81],  $Pr^{3+}$  (Figure 4, Plots A67-70, E57-63) [82], and  $Gd^{3+}$  (Figure 4, Plot A71, E64-69) [83] as CN = 6, consisting 65|82

of either 6 F<sup>-</sup> ions, or 5 F<sup>-</sup> and 1 O<sup>2-</sup> ions if O<sup>2-</sup> were present. This interpretation is supported by Raman results, which have shown that if the lanthanide (La, Ce, Nd, Sm, Dy, Yb, Y) mole fraction is less than 0.25, their structures tend to be undistorted octahedra (CN = 6) [109][110], a result consistent across bromides and chlorides [111][112]. High temperature nuclear magnetic resonance (HT-NMR) measurements of LaF<sub>3</sub> mixtures with alkali fluorides have agreed with the result as well [113].

Recently, some work has addressed the structure of oxy-fluoride lanthanide species, which can form when  $O^{2-}$  is present. A Raman study was performed of  $CeF_3$  in FLiNaK with and without  $Li_2O$  addition [114]. Without  $Li_2O$ , consistent spectra were observed up to 20 mol%  $CeF_3$  and were attributed to  $CeF_6^{3-}$  (CN = 6) via QC-DFT analysis. Next, 5 mol%  $Li_2O$  was added to 5 mol%  $CeF_3$  in FLiNaK, and several new peaks appeared, followed by further spectral changes as 10 mol% and 20 mol%  $Li_2O$  were added. This behavior was attributed via QC-DFT to formation of  $Ce_2O_2F_{10}^{6-}$  (CN = 6) at lower  $Li_2O$  concentration and a transition to  $Ce_2O_2F_8^{4-}$  (CN = 5) at higher concentration. Khokhryakov theorized the presence of  $CeOF_5^{4-}$  (CN = 6) with addition of about 1E-04 mole fraction of  $Ce_2O_3$  in LiF-NaF [81], which would be consistent with the results of  $Ce_3O_3$  bridging does not occur for very low  $Ce_3O_3$  concentrations and  $Ce_3O_3$  in LiF-NaF [81], which would be consistent with the results of  $Ce_3O_3$  bridging does not occur for very low  $Ce_3O_3$  concentrations and  $Ce_3O_3$  in LiF-NaF [81], which would be consistent with the results of  $Ce_3O_3$  bridging does not occur for very low  $Ce_3O_3$  concentrations and  $Ce_3O_3$  for  $Ce_3O_3$  bridged by  $Ce_3O_3$  and also found that that  $Ce_3O_3$  decreased with increasing  $Ce_3O_3$  content, from 5 to 3 or 4 [115].

## 5.2.3.2. Actinides

Through comparison with crystalline [116] and aqueous spectra [117][118], Young theorized UF<sub>3</sub> to have a CN of 8 or 9 in FLiBe and FLiNaK (Figure 4, Plots A9-10, E34-35) [27] and PaF<sub>4</sub> to have a CN of 7 within the LiF-BeF<sub>2</sub>-ThF<sub>4</sub> (72-16-12 mol%) solvent (Figure 4, Plots A17-18, E37) [31] . Bamberger measured absorption spectra of PuF<sub>3</sub> in LiF-BeF<sub>2</sub>-ThF<sub>4</sub> (72-16-12 mol%) solvent (Figure 4, Plot A19, E42) [32], but did not hypothesize on the CN. More work is needed to investigate the structure of these species via complementary experimental and modeling methods.

UF<sub>4</sub> was of particular interest due to its use as fuel in the MSRE. Toth proposed an equilibrium between the CN = 7 and CN = 8 species as the solvent and temperature were varied [14]. With decreasing LiF concentration (i.e., decreasing dissociated F) and increasing temperature, CN = 7 was favored. This was inferred through observation of subtle shifts in peak intensity and location and comparison with crystalline spectra of U<sup>4+</sup>-doped KTh<sub>2</sub>F<sub>9</sub> (CN = 9), K<sub>7</sub>Th<sub>6</sub>F<sub>31</sub> (CN = 8), and Cs<sub>3</sub>ThF<sub>7</sub> (CN = 7) [14]. Figure 9a shows the disappearance of several peaks as solvent is varied from FLiNaK, to FLiBe, to LiF-BeF<sub>2</sub> (48-52 mol%), (i.e. increasing fluoroacidity). Plots A30 and A31 in Figure 4 show similar shifts as temperature increases. Two recent studies have used a combined MD and EXAFS approach to investigate alkali fluoride mixtures with ThF<sub>4</sub> and UF<sub>4</sub> [119][120]. The results show qualitative agreement with Toth, as the average

coordination was about 8 for both species.

As part of the redox control for the MSRE fuel, for the purpose of corrosion control, a small amount of  $U^{4+}$  would be reduced to  $U^{3+}$ . There was potential for  $U^{3+}$  to react with graphite to form insoluble  $UC_2$  via the back-reaction of equation 27 [43][45][44], which would cause similar reactivity concerns as that of  $UO_2$  precipitation [4].

$$3UF_4 + UC_2 \leftrightarrow 4UF_3 + C$$
 27

As a result, the equilibrium quotient of the reaction in equation 27 was measured as a function of temperature, varying solvent composition between FLiBe and LiF-BeF<sub>2</sub> (48-52 mol%), and varying carbide stoichiometry between UC<sub>2</sub> and U<sub>2</sub>C<sub>3</sub> [44]. Figure 9b shows a decrease in the U<sup>4+</sup> peak at 1.1 μm (9147 cm<sup>-1</sup>) and an increase in the U<sup>3+</sup> peak at 0.88 μm (11,360 cm<sup>-1</sup>), as temperature increases from 500 to 700 °C. Accordingly, the equilibrium quotient increased by a factor of 10<sup>6</sup> over this temperature range. U<sub>2</sub>C<sub>3</sub> is less stable than UC<sub>2</sub>, causing an increase in the equilibrium quotient. The use of LiF-BeF<sub>2</sub> (48-52 mol%) as solvent caused the equilibrium quotient to increase as well. Using the van't Hoff equation, Toth estimated the exothermic heats of solution for UF<sub>4</sub> and UF<sub>3</sub> in FLiBe, with that of UF<sub>4</sub> having a substantially more negative value. Toth suggested that this was because 'UF<sub>4</sub> forms complexes of greater stability than does UF<sub>3</sub>' [44]. Moreover, it was suggested that fluoroacidic melts stabilize lower oxidation state cations due to dissociated 'F' deficiency;' conversely, as fluorobasicity increases, the higher oxidation state is favored.

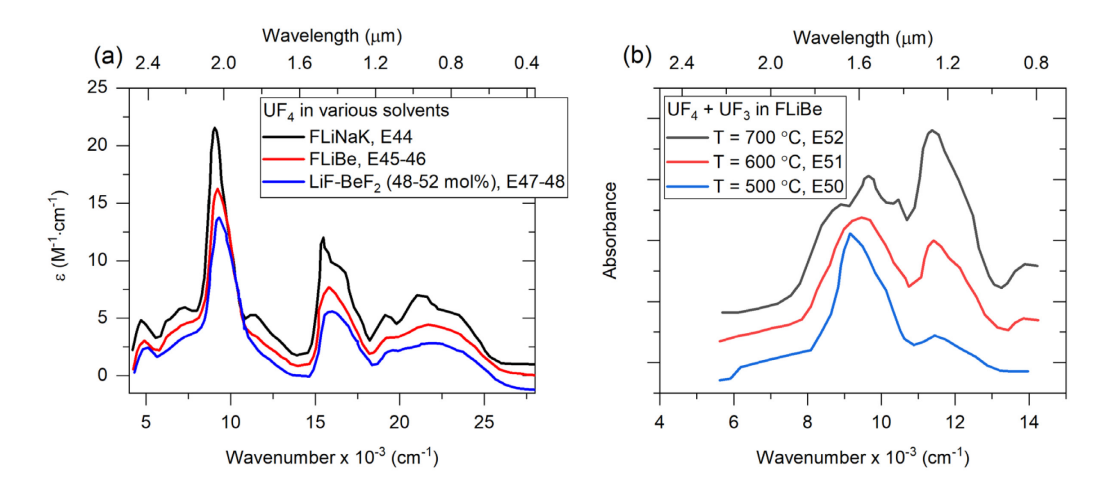


Figure 9. Electronic absorption spectra of actinide solutes in molten fluoride solvents: (a) Molar absorptivity ( $\varepsilon$ ) spectra of  $U^{4+}$  in FLiNaK, FLiBe, and LiF-BeF2 (48-52 mol%) (b) qualitative absorbance spectra of FLiBe solutions containing  $U^{3+}$  and  $U^{4+}$ . We give the spectrum index (E#) for each curve, for reference in Table 8. We note that multiple spectra indices are given in (a) because the measurement temperature of 550 °C falls between the two entries in Table 8. We plot in wavenumber (and wavelength) because the spectral changes are more easily visible. Following Toth's convention, we have separated each cruve in (a) by a single molar absorptivity unit.

## 5.2.4. Summary

Inferences from electronic absorption data are mostly consistent with octahedral symmetry (CN = 6) for transition metal and lanthanide solutes and equilibria between CN = 7, 8, and 9 for actinides, depending on solvent fluoroacidity. Measurements of redox equilibria of  $Te^{-}$ ,  $Cr^{2+}/Cr^{3+}$ , and  $U^{3+}/U^{4+}$  have been conducted. Study of disproportionation has shown that higher valent ions appear to be more stable in fluorobasic melts.

#### 6. DISCUSSION AND SUMMARY OF ABSORPTION DATA

## 6.1. Structural interpretation

## 6.1.1. Vibrational

Comparison of liquid LiF infrared vibrational edge and resonance data with crystalline data, yielded the view of the melt as a highly disordered lattice, which we consider to be analogous to vibrational resonance among a cation's first coordination shell in a melt of dissociated ions. LiF-KF mixtures were interpreted similarly; however, observed intensity changes were not monotonic as the LiF peak appeared to be favored and a secondary peak was observed. Raman [91] and MD [87][92] results suggest that this behavior could be due to the presence of intermediate range order. There is no infrared vibrational resonance data for FLiNaK. As a melt of dissociated ions, it is predicted to exhibit similar behavior as LiF-KF, consisting of a superposition of pure component peaks weighted towards LiF.

Studies of LiF-KF-ZrF<sub>4</sub> and NaF-KF-ZrF<sub>4</sub> (varying ZrF<sub>4</sub>) were interpreted as evidence of associated monomer and oligomer formation by Zr<sup>4+</sup>, in qualitative agreement with combined HT-NMR, EXAFS and MD [97]. Likewise, transmittance measurement of a thin film of FLiBe exhibited a peak at 12.5 µm, in agreement with the QC-DFT-predicted spectra for the associated monomer BeF<sub>4</sub><sup>2-</sup>, as well as with Raman [67] and MD [89]. The spectra exhibited another peak at 6.25 µm that was attributed to an overtone, but we also suggest a vibration of the oligomer Be<sub>2</sub>F<sub>7</sub><sup>3-</sup> (indicated from Raman[68]).

In crystalline alkali and alkaline earth fluorides, increasing temperature and the phase transition from solid to liquid results in peak broadening and shifting of the vibrational absorption edge to the NIR. More data is needed to quantify the degree of shifting that occurs in FLiBe and FLiNaK, and other molten-fluoride solvents.

The infrared resonance spectra of solutes  $OH^-$ ,  $OD^-$ ,  $Ta^{5+}$ , and  $Nb^{5+}$  dissolved in fluoride melts have been measured.  $Ta^{5+}$  and  $Nb^{5+}$  were hypothesized to exist as  $TaF_7^{2-}$ ,  $TaF_6^-$ , and  $NbF_7^{2-}$ , and were also found to be quite sensitive to the addition of  $O^{2-}$ , forming several different hypothesized oxy-fluoride species.

In summary, infrared spectral data can be used to probe the structural dynamics of different types of solvents (dissociated vs associated) as well as solutes species. Deduction of the coordination environment

from vibrational resonances needs to be validated by other experimental and modeling techniques. Once validated, vibrational data can be conveniently used to probe for changes in structure due to different variables such as temperature and solvation environment. We note that Raman spectroscopy has traditionally been used for this purpose among molten fluorides (e.g., [121]) and can be less challenging experimentally, and we refer the reader to section 3.2.1.1 for a brief background; however, infrared absorption spectroscopy provides complementary information necessary for more complete vibrational characterization, as well quantitative data useful for RHT, which Raman cannot provide.

#### 6.1.2. Electronic

Using various analysis techniques, the transition metal ions  $Ni^{2+}$ ,  $Cr^{2+}$ ,  $Cr^{3+}$ ,  $Fe^{2+}$ ,  $Fe^{3+}$ ,  $Co^{2+}$ ,  $Mn^{2+}$ ,  $Mn^{3+}$ ,  $Cu^{2+}$ , and  $Nb^{4+}$  have been interpreted as CN=6, with the exception of  $Nb^{4+}$  as 7. AIMD results predict CN=5 for  $Cr^{2+}$  and CN=6 for  $Cr^{3+}$ , and they are the only transition-metal ions that have been subject to extensive structural study (in the form of AIMD [98][94][88]) and optical data and AIMD suggest that these CNs are invariant to solvent fluoroacidity [29][88]. Electronic absorption data of  $Cr^{2+}$  and  $Cr^{3+}$  in FLiNaK and FLiBe [52] provide evidence that in a more fluorobasic melt (higher activity of dissociated  $F^-$ ), the higher oxidation state ion is favored. More experimental study of the structure of these solutes and AIMD modeling of the electronic spectra is needed to better correlate the optical spectra with the electronic structure and coordination of these ions.

Using ligand field theory, the lanthanide ions  $Ce^{3+}$ ,  $Pr^{3+}$ , and  $Gd^{3+}$  were interpreted as CN=6, which is consistent with the current understanding from HT-NMR [113] and Raman [109][110][111][112]. From comparison with aqueous and crystalline spectra,  $Pa^{4+}$  and  $U^{3+}$  were interpreted as CN=7 and 8 or 9. The electronic absorption spectrum of  $Pu^{3+}$  has been measured, but the CN was not theorized. An equilibrium between CN=7 and 8 for  $U^{4+}$  species was proposed, favoring higher coordination in fluorobasic melts (i.e., high concentrations of dissociated F). These CN's for  $U^{4+}$  have been partially validated by recent combined MD and EXAFS [119][120]. In addition to structural studies, the  $U^{4+}/U^{3+}$  equilibrium with  $UC_2/C$ ,  $U_2C_3/C$ , and  $H_2/HF$  was studied as a function of temperature in different solvents, finding that the lower valence  $U^{3+}$  was increasingly favored at higher temperatures and in more fluoroacidic melts, a finding similar to that of  $Cr^{2+}/Cr^{3+}$ .

As with vibrational absorption, electronic absorption data provides a unique window into the solute-solvent coordination environment and with information from complementary methods (e.g., NMR, EXAFS, modeling), structural changes can be inferred from spectral changes with temperature and composition.

## 6.2. Radiative heat transfer

Electronic absorption data for some solutes in molten fluoride solvents exhibit peaks into the NIR. 69|82

As discussed in section 5.2.2.1, Cr species are particularly important due to the prevalence of Cr in structural alloys and the relative stability of Cr species in molten fluoride solvents. In an experiment to measure the thermal conductivity of FLiNaK, Ewing found a decrease in plate-to-plate RHT correlated with increased Cr species concentration in FLiNaK [122]. To further investigate the RHT-significance of Cr species, Chaleff developed an AIMD model of Cr in FLiNaK [123]. The oxidation state of Cr used in the model was not specified, but the authors validate their results in the visible spectrum by comparison to Young's data on  $Cr^{3+}$  in FLiNaK (Figure 4, Plot A4, E2). In addition to the peaks seen in the visible, Chaleff's results predict a wide band that slowly increases from about 2 to 8  $\mu$ m. The measured  $\kappa_{\lambda}$  values for CrF<sub>3</sub> only extend to 1.0  $\mu$ m and for CrF<sub>2</sub> they extend slightly further to about 1.4  $\mu$ m, and both are decreasing with increasing wavelength at these points (Figure 8a); experimental absorption data over 2 to 8  $\mu$ m is needed to test Chaleff's prediction of an electronic peak at higher wavelengths. In addition to measurements for the absolute value of  $\kappa_{\lambda}$ , it also important to know if there are sharp absorption peaks around the peak of the Planck distribution at the temperatures of interest, in which case the gray  $\kappa$  assumption would introduce more distortion than that due to an absorption edge.

Other corrosion products such as  $Fe^{2+}$  (Figure 4, Plot A14, E5), and  $Ni^{2+}$  (Figure 4, Plot A15, E6), show absorption peaks up to 2  $\mu$ m and would therefore be good candidates to investigate for potential absorption further into the NIR and MIR. Absorption peaks for lanthanide and actinide elements tend to reach farther into the infrared (between 2-3  $\mu$ m) than transition metals. Thus, they likely would have a greater impact on RHT; MIR absorption data is needed to experimentally verify this prediction.

In addition to electronic absorption by solute species, vibrational edge absorption by solvent species may be significant. We present the extrapolated  $\kappa_{\lambda}$  of FLiBe and FLiNaK in Figure 10, which show nonnegligible overlap with the Planck distribution at 700 °C. Chaleff generated the FLiNaK prediction by performing a molar average of tabulated (by Li [124]) high-temperature  $\kappa_{\lambda}$  data for crystalline LiF and NaF [9]; KF was neglected because its NIR edge is expected to be beyond the region of significance for RHT due to its resonance being at much further wavelength than LiF and NaF [125]. We presented Liu's NIR edge data for FLiBe (Figure 6b). Then, we apply Deutch's exponential data fit (equation 28) to Liu and Chaleff's data, assuming a minimum value,  $\kappa_{\lambda,min} = 0.7 \ m^{-1}$ , for both FLiBe and FLiNaK (which is near the  $\kappa_{\lambda,min}$  measured for NaCl-KCl (50-50 w%) [126]).

$$\kappa_{\lambda} = \kappa_{\lambda,min} + A \cdot \exp\left(-\frac{B}{\lambda}\right)$$

Figure 10 plots this fit (dashed lines). The extrapolated  $\kappa_{\lambda}$  for FLiBe and FLiNaK in the NIR/MIR show values that fall in the 1 to 6000 m<sup>-1</sup> range identified by heat transfer modeling to be of engineering relevance [10]. Assuming a 1 cm pipe, and  $\kappa$  range of relevance to RHT of 10 – 6000 m<sup>-1</sup>, we calculate gray  $\kappa$  (using the Planck-mean absorption coefficient, given in equation 29) at 700 °C to be 546 m<sup>-1</sup> for

70|82

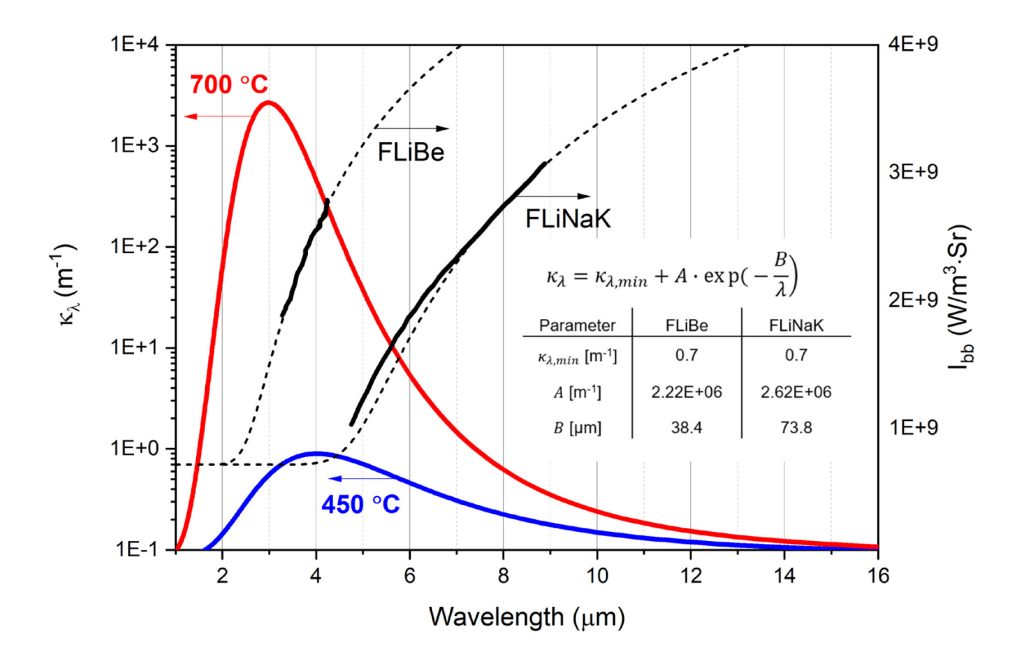


Figure 10. Extrapolated  $\kappa_{\lambda}$  of FLiBe (V24) and FLiNaK (V34). Dashed line: Deutch's equation (eq. 28) is fitted to Liu's FLiBe data (V24) [50] and Chaleff's FLiNaK molar-averaging prediction based on single component data (V34) [9]. The Planck distribution is plotted at temperatures of 450 and 700 °C, to illustrate the spectral range of interest to RHT at different temperatures. Equation 28 is also inset, along with fitting parameters for FLiBe and FLiNaK.

## 7. CONCLUSION

Advanced nuclear reactors that utilize molten salts are being designed to operate between 500 and 700 °C and reactor designers need to account for RHT in thermal-hydraulic analysis.  $\kappa_{\lambda}$  (i.e. the imaginary part of refractive index) of the molten salts in the NIR/MIR range is a necessary input for RHT modeling. We note that the real part of the refractive index should be known as well because it affects the Planck distribution, though it is not the focus of this review. As shown by the molten-fluoride studies in this review, optical-absorption spectroscopic measurements can provide this data. Furthermore, as the field currently stands, understanding of the molecular and electronic structure of the salt is not complete, and optical spectroscopy can be a convenient way to provide indirect information of this nature.

Given the need for optical absorption data on molten salts, a critical review of methods for visible and infrared spectroscopic absorption of high temperature liquid fluoride salts is provided in an attempt to spur further experimentation. To serve as a reference for researchers investigating the structure of fluoride 71|82

salts or using optical spectroscopy for other applications such as thermochemistry [44], kinetics [52], online monitoring [127], or radiative heat transfer [13], we selected 37 journal articles and summarized in several tables organizing the methods, available spectra, and structural interpretations. Experimental methods, including transmittance and reflectance, cover operating temperature ranges from 425 to 1527 °C. 17 transmittance setups and 7 reflectance setups were found, and they are summarized in Table 1 (transmittance) and Table 4 (reflectance). Electronic absorption data has been compiled for the transition metal ions  $Cr^{2+}$ ,  $Cr^{3+}$ ,  $Mn^{2+}$ ,  $Mn^{3+}$ ,  $Fe^{2+}$ ,  $Fe^{3+}$ ,  $Co^{2+}$ ,  $Ni^{2+}$ ,  $Cu^{2+}$ ,  $Nb^{4+}$ , the metalloid ion  $Te^{-}$ , the lanthanide ions  $Pr^{3+}$ ,  $Ce^{3+}$ ,  $Gd^{3+}$ , and the actinide ions  $Pa^{4+}$ ,  $U^{3+}$ ,  $U^{4+}$ , and  $Pu^{3+}$ . Vibrational absorption data has been compiled for the mixtures LiF-KF, LiF-NaF, LiF-KF-ZrF4, LiF-NaF-ZrF4, FLiBe, compounds LiF,  $CaF_2$ ,  $BaF_2$ , and CsF and the solute species  $OH^-$ ,  $OD^-$ ,  $Nb^{5+}$ , and  $Ta^{5+}$ .

From the structural perspective, more complementary theoretical and experimental studies are needed for transition metal solutes, as Cr<sup>2+</sup>/Cr<sup>3+</sup> currently have received sole attention. Electronic absorption data exists for U<sup>3+</sup>, Pa<sup>4+</sup>, and Pu<sup>3+</sup> but needs comparison with complementary methods as well. Vibrational absorption data in the resonance region is needed for both FLiBe and FLiNaK, which could elucidate bridging behavior and intermediate-range structures, respectively. While UV-vis/NIR electronic and MIR vibrational spectra are an indirect measure of coordination environment and oxidation state, once connected with a structural model they form a powerful way to probe for changes in these properties with respect to temperature or different solvation environments.

From the RHT perspective, it would be useful to investigate the electronic absorption of otherwise well-studied solutes (e.g.,  $Cr^{2+}/Cr^{3+}$ ,  $U^{4+}/U^{4+}$ ) extending from the NIR into the MIR. The measured  $\kappa_{\lambda}$  values for CrF<sub>3</sub> only extend to 1.0 µm and for CrF<sub>2</sub> they extend slightly further to about 1.4 µm, and both are decreasing with increasing wavelength at these points (Figure 8a); experimental absorption data over 2 to 8 µm is needed to test Chaleff's prediction of an electronic peak at higher wavelengths [123]. In addition to measurements for the absolute value of  $\kappa_{\lambda}$ , it also important to know if there are sharp absorption peaks around the peak of the Planck distribution at the temperatures of interest, in which case the gray  $\kappa$  assumption would introduce more distortion than that due to an absorption edge. Characterization of the NIR/MIR edge for potential reactor coolant FLiBe and its thermal-hydraulic surrogate FLiNaK and their temperature dependence is also needed for quantifying RHT effects. By fitting to experimental data for FLiBe (Figure 4, Plot A40, V24) and prediction of FLiNaK (Table 5, V35), we extrapolate  $\kappa_{\lambda}$  values over the range of RHT significance. Assuming a 1 cm pipe, and  $\kappa$  range of relevance to RHT of 10-6000 m<sup>-1</sup>, we calculate gray  $\kappa$  (using the Planck-mean absorption coefficient, given in equation) at 700 °C to be 546 m<sup>-1</sup> for FLiBe and 276 m<sup>-1</sup> for FLiBaK.

#### **DECLARATION OF COMPETING INTEREST**

At the time at which the article is published, some of the authors of this manuscript have interests in or relationships with entities that are commercializing molten salt technology. The content of this manuscript or the direction of the research presented herein was not influenced by these entities, nor by the author's relationships with these entities.

#### **ACKNOWLEDGEMENTS**

The information, data, or work presented herein was funded in part by the Department of Energy Office of Nuclear Energy's Nuclear Energy University Program, Projects NEUP-17-13232, NEUP-IRP-17-14541, and NEUP-21-24563. This work has also been supported through the US Nuclear Regulatory Commission Graduate Student Fellowship program on Grant NRC-HQ-84-15-G-0040. The views and opinions of authors expressed herein do not necessarily state or reflect those of the United States Government or any agency thereof. The authors would also like to acknowledge support by the UC Berkeley SALT Laboratory researchers and by University of Wisconsin Thermal Hydraulics Laboratory and staff. RS would like to acknowledge funding support from the Hellman Foundation. MK was partially supported by the National Science Foundation (1750341). RG would like to acknowledge funding support from U.S. Department of Energy, Office of Nuclear Energy, Nuclear Energy University Program, Grant DE-NE0008985 and INL Laboratory Directed Research & Development (LDRD) Program under DOE Idaho Operations Office Contract DE-AC07-05ID14517.

#### **CONTRIBUTIONS**

Conceptualization: RS, WD, RG, Writing – Original Draft: WD, RG, Writing – Review & Editing: RS, SM, MA, MK, Formal Analysis: WD, Data Curation: WD, RS, Visualization: WD, SM, RS, Resources: RS, Funding Acquisition: RS, MK, MA, Supervision: RS, MA, MK, Project Administration: RS, MK.

## REFERENCES

- [1] J. Serp, M. Allibert, et al., 'The molten salt reactor (MSR) in generation IV: Overview and perspectives', Prog. Nucl. Energy, vol. 77, pp. 308–319, (2014).
- [2] E. S. Bettis, W. B. Cottrell, et al., 'The Aircraft Reactor Experiment Operation', Nucl. Sci. Eng., vol. 2, no. 6, pp. 841–853, (1957).
- [3] P. N. Haubenreich and J. R. Engel, 'Experience With Molten-Salt Reactor Experiment', Nucl. Appl. Technol., vol. 8, no. 2, pp. 118–136, (1970).
- [4] W. R. Grimes, 'Molten-Salt Reactor Chemistry', Nucl. Appl. Technol., vol. 8, no. 2, pp. 137–155, (1970).

- [5] E. S. Bettis and R. C. Robertson, 'The deisgn and performance features of a single-fluid moltensalt breeder reactor', Nucl Appl Technol, vol. 8, no. 2, pp. 190–207, (1970).
- [6] R. O. Scarlat, M. R. Laufer, et al., 'Design and licensing strategies for the fluoride-salt-cooled, high-temperature reactor (FHR) technology', Prog. Nucl. Energy, vol. 77, pp. 406–420, (2014).
- [7] N. Zweibaum, G. Cao, et al., 'Phenomenology, methods and experimental program for fluoride-salt-cooled, high-temperature reactors (FHRs)', Prog. Nucl. Energy, vol. 77, pp. 390–405, (2014).
- [8] C. Forsberg, G. Zheng, et al., 'Fusion Blankets and Fluoride-Salt-Cooled High-Temperature Reactors with Flibe Salt Coolant: Common Challenges, Tritium Control, and Opportunities for Synergistic Development Strategies Between Fission, Fusion, and Solar Salt Technologies', Nucl. Technol., vol. 206, no. 11, pp. 1778–1801, (2020).
- [9] E. S. Chaleff, T. Blue, et al., 'Radiation Heat Transfer in the Molten Salt FLiNaK', Nucl. Technol., vol. 196, no. 1, pp. 53–60, (2016).
- [10] M. Abou Dbai, R. O. Scarlat, et al., 'Radiative heat transfer in FLiBe molten salt participating medium in a vertical heated tube under forced and mixed convection laminar flows', Nucl. Eng. Des., vol. 368, p. 110775, (2020).
- [11] J. Ambrosek, M. Anderson, et al., 'Current Status of Knowledge of the Fluoride Salt (FLiNaK) Heat Transfer', Nucl. Technol., vol. 165, no. 2, pp. 166–173, (2009).
- [12] S. Zhang and X. Sun, 'Convective and Radiative Heat Transfer in Molten Salts', Nucl. Technol., vol. 206, no. 11, pp. 1721–1739, (2020).
- [13] C. Coyle, E. Baglietto, et al., 'Advancing Radiative Heat Transfer Modeling in High-Temperature Liquid Salts', Nucl. Sci. Eng., vol. 194, no. 8–9, pp. 782–792, (2020).
- [14] L. M. Toth, 'Coordination Effects on the Spectrum of Uranium (IV) in Molten Fluorides', J. Phys. Chem., vol. 75, no. 5, pp. 631–636, (1971).
- [15] A. L. Rollet and M. Salanne, 'Studies of the local structures of molten metal halides', Annu. Reports Prog. Chem. Sect. C, vol. 107, pp. 88–123, (2011).
- [16] D. M. Gruen, 'Fused-salt Spectrophotometry', Q. Rev. Chem. Soc., vol. 19, pp. 349–368, (1965).
- [17] R. E. Hester, 'Vibrational Aspects of Molten Salts', in Advances in Molten Salt Ch, (1971)., pp. 1–61.
- [18] T. R. Griffiths, 'Molten Salt Spectroscopy', in Molten Salt Techniques, Volume 2, (1984)., pp. 79–135.
- [19] L. M. Toth, 'Containers for Molten flouride Spectroscopy', ORNL-TM-2047, (1967).
- [20] T. G. Mayerhöfer and J. Popp, 'Beer's law derived from electromagnetic theory', Spectrochim. Acta Part A Mol. Biomol. Spectrosc., vol. 215, pp. 345–347, (2019).
- [21] E. Sani and A. Dell'Oro, 'Optical constants of ethylene glycol over an extremely wide spectral

- range', Opt. Mater. (Amst)., vol. 37, pp. 36-41, (2014).
- [22] E. Sani and A. Dell'Oro, 'Spectral optical constants of ethanol and isopropanol from ultraviolet to far infrared', Opt. Mater. (Amst)., vol. 60, pp. 137–141, (2016).
- [23] J. P. Young and J. C. White, 'A High-Temperature Cell Assembly for Spectrophotometric Studies of Molten Fluoride Salts', Anal. Chem., vol. 31, no. 11, pp. 1892–1895, (1959).
- [24] J. P. Young and J. C. White, 'Absorption Spectra of Molten Fluoride Salts', Anal. Chem., vol. 32, no. 7, pp. 799–802, (1960).
- [25] J. P. Young, 'Windowless Spectrophotometric Cell for Use with Corrosive Liquids', Anal. Chem., vol. 36, no. 2, pp. 390–392, (1964).
- [26] J. P. Young and G. P. Smith, 'Coordination of Fluoride Ions About Nickel (II) Ions in the Molten LiF-NaF-KF Eutectic', J. Chem. Phys., vol. 40, pp. 913–914, (1964).
- [27] J. P. Young, 'Spectra of Uranium(IV) and Uranium(III) in Molten Fluoride Solvents', Inorg. Chem., vol. 6, no. 8, pp. 1486–1488, (1967).
- [28] J. P. Young, 'Analytical Chemistry Division Annual Progress Report for Period Ending November 15, 1963', Tech. Rep. ORNL-3537, p. 26, (1963).
- [29] J. P. Young, 'Absorption spectra of several 3d transition metal ions in molten fluoride solution', Inorg. Chem., vol. 8, no. 4, pp. 825–827, (1969).
- [30] J. P. Young, 'Molten-Salt Reactor Program Semiannual Progress Report for Period Ending February 28, 1969', Tech. Rep. ORNL-4396, pp. 202–204, (1969).
- [31] J. P. Young, C. E. Bamberger, et al., 'Spectral studies of f-d and f-f transitions of Pa(IV) in molten LiF-BeF<sub>2</sub>-ThF<sub>4</sub>', J. Inorg. Nucl. Chem., vol. 36, no. 11, pp. 2630–2632, (1974).
- [32] C. E. Bamberger, R. G. Ross, et al., 'Absence of an effect of oxide on the solubility and the absorption spectra of PuF<sub>3</sub> in molten LiF-BeF<sub>2</sub>-ThF<sub>4</sub> and the instability of plutonium(III) oxyfluorides', J. Inorg. Nucl. Chem., vol. 33, no. 10, pp. 3591–3594, (1971).
- [33] J. P. Young, J. B. Bates, et al., 'Molten-Salt Reactor Program Semiannual Progress Report Period Ending February 29, 1972', Tech. Rep. ORNL-4782, p. 59, (1972).
- [34] J. B. Bates, J. P. Young, et al., 'Molten-Salt Reactor Program Semiannual Progress Report Period Ending February 29, 1972', Tech. Rep. ORNL-4782, pp. 59–62, (1972).
- [35] F. L. Whiting, G. Mamantov, et al., 'Electrochemical Generation and Spectrophotometric Study of Solute Species in Molten Fluoride Media', J. Inorg. Nucl. Chem., vol. 35, no. 5, pp. 1553–1563, (1973).
- [36] J. P. Young, G. Mamontov, et al., 'Simultaneous Voltammetric Generation of U(III) and Spectrophotometric Observation of the U(III)-U(IV) System in Molten Lithium Fluoride-Beryllium Fluoride-Zirconium Fluoride', J. Phys. Chem., vol. 71, no. 3, pp. 782–783, (1967).

- [37] C. E. Bamberger, C. F. Baes, et al., 'Containment of molten fluorides in silica; effect of temperature on the spectrum of U<sup>4+</sup> in molten LiF-BeF<sub>2</sub> mixtures', J. Inorg. Nucl. Chem., vol. 30, no. 7, pp. 1979–1981, (1968).
- [38] C. E. Bamberger, J. P. Young, et al., 'The chemistry of tellurium in molten Li<sub>2</sub>BeF<sub>4</sub>', J. Inorg. Nucl. Chem., vol. 36, no. 5, pp. 1158–1160, (1974).
- [39] F. L. Whiting, G. Mamontov, et al., 'Spectral Studies of O2<sup>-</sup>, NO<sub>2</sub><sup>-</sup> and CrO<sub>4</sub><sup>2-</sup> in Molten LiF-NaF-KF and of O<sub>2</sub><sup>-</sup> in Liquid Ammonia', J. Inorg. Nucl. Chem., vol. 34, no. 8, pp. 2475–2481, (1972).
- [40] F. L. Whiting, G. Mamantov, et al., 'Spectral Evidence for the Existence of the Superoxide Ion in Molten LiF-NaF-KF', J. Am. Chem. Soc., vol. 91, no. 23, pp. 6531–6532, (1969).
- [41] J. B. Bates, J. P. Young, et al., 'Stability of BF<sub>3</sub>OH' ion in molten and solid NaBF<sub>4</sub> and NaF-NaBF<sub>4</sub> eutectics', J. Inorg. Nucl. Chem., vol. 34, no. 9, pp. 2721–2727, (1972).
- [42] L. M. Toth, J. P. Young, et al., 'Diamond-Windowed Cell for Spectrophotometry of Molten Fluoride Salts', Anal. Chem., vol. 41, no. 4, pp. 683–685, (1969).
- [43] L. M. Toth and L. O. Gilpatrick, 'Equilibria of uranium carbides in the molten fluoride solutions of UF<sub>3</sub> and UF<sub>4</sub> contained in graphite at 850°K', J. Inorg. Nucl. Chem., vol. 35, no. 2, pp. 1509–1513, (1973).
- [44] L. M. Toth and L. O. Gilpatrick, 'Temperature and solvent effects on the equilibrium of dilute uranium trifluoride solutions contained in graphite', J. Phys. Chem., vol. 77, no. 23, pp. 2799–2803, (1973).
- [45] L. M. Toth and L. O. Gilpatrick, 'The Equlibrium of Dilute UF<sub>3</sub> Solutions Contained in Graphite', Tech. Rep. ORNL-TM-4056, (1972).
- [46] L. O. Gilpatrick and L. M. Toth, 'The Hydrogen Reduction of Uranium Tetrafluoride in Molten Fluoride Solutions', J. Inorg. Nucl. Chem., vol. 39, no. 10, pp. 1817–1822, (1977).
- [47] L. M. Toth and L. O. Gilpatrick, 'The Ligand-Field Spectrum of Niobium(IV) in Fluoride Melts', Inorg. Chem., vol. 15, no. 1, pp. 243–244, (1976).
- [48] L. M. Toth and B. F. Hitch, 'Telluride ion chemistry in molten salts', Inorg. Chem., vol. 17, no. 8, pp. 2207–2211, (1978).
- [49] G. B. Varlamov, G. N. Vasil'chenko, et al., 'Thermophysical and optical properties of fluoride crystals and melts', High Temp. Press., vol. 21, no. 6, pp. 647–656, (1989).
- [50] S. Liu, T. Su, et al., 'Investigation on molecular structure of molten Li<sub>2</sub>BeF<sub>4</sub> (FLiBe) salt by infrared absorption spectra and density functional theory (DFT)', J. Mol. Liq., vol. 242, pp. 1052–1057, (2017).
- [51] H. Liu, Y. Liu, et al., 'An instrument established for the high temperature measurement of ultraviolet-visible absorption spectra of molten fluoride salt behaving as coolant in the molten salt

- reactor', Int. Conf. Nucl. Eng. Proceedings, ICONE, (2018).
- [52] Y. Liu, Y. Song, et al., 'Corrosion of Cr in molten salts with different fluoroacidity in the presence of CrF<sub>3</sub>', Corros. Sci., vol. 169, p. 108636, (2020).
- [53] G. Zong, Z. B. Zhang, et al., 'Preparation of high-purity molten FLiNaK salt by the hydrofluorination process', J. Fluor. Chem., vol. 197, pp. 134–141, (2017).
- [54] K. B. Andersen, E. Christensen, et al., 'Infrared and Raman spectroscopic investigations of the Nb(V) fluoro and oxofluoro complexes in the LiF-NaF-KF eutectic melt with development of a diamond IR cell', Inorg. Chem., vol. 39, no. 16, pp. 3449–3454, (2000).
- [55] R. S. Sussman, C. S. J. Pickles, et al., 'CVD diamond windows for infrared synchrotron applications', Nuovo Cim. D, vol. 20, no. 4, pp. 503–525, (1998).
- [56] R. Kitamura, L. Pilon, et al., 'Optical constants of silica glass from extreme ultraviolet to far infrared at near room temperature', Appl. Opt., vol. 46, no. 33, pp. 8188–8133, (2020).
- [57] A. K. Harman, S. Ninomiya, et al., 'Optical constants of sapphire (α-Al<sub>2</sub>O<sub>3</sub>) single crystals', J. Appl. Phys., vol. 76, no. 12, pp. 8032–8036, (1994).
- [58] M. E. Thomas, 'Vacuum-ultraviolet characterization of sapphire, ALON, and spinel near the band gap', Opt. Eng., vol. 32, no. 6, p. 1340, (1993).
- [59] M. R. Querry, 'Optical Constants, Report No. AD-A158 623, CRDC-CR-85034', (1985).
- [60] T. F. Deutsch, 'Absorption coefficient of infrared laser window materials', J. Phys. Chem. Solids, vol. 34, no. 12, pp. 2091–2104, (1973).
- [61] D. M. Roessler and D. R. Huffman, 'Magnesium Oxide (MgO)', in Handbook of Optical Constants of Solids II, (1991)., pp. 919–955.
- [62] W. C. Phillips, R. Gakhar, et al., 'Design and performance of high-temperature furnace and cell holder for in situ spectroscopic, electrochemical, and radiolytic investigations of molten salts', Rev. Sci. Instrum., vol. 91, no. 8, (2020).
- [63] Y. Xiao, C. Wan, et al., 'Precision Measurements of Temperature-Dependent and Nonequilibrium Thermal Emitters', Laser Photonics Rev., vol. 14, no. 8, p. 1900443, (2020).
- [64] H. J. Bowlden and J. K. Wilmshurst, 'Evaluation of the One-Angle Reflection Technique for the Determination of Optical Constants', J. Opt. Soc. Am., vol. 53, no. 9, pp. 1073–1078, (1963).
- [65] J. R. Jasperse, A. Kahan, et al., 'Temperature dependence of infrared dispersion in ionic crystals LiF and MgO', Phys. Rev., vol. 146, no. 2, pp. 526–542, (1966).
- [66] D. G. Mead, 'Comparison of the Optical and Dielectric Properties of Crystalline and Molten Lithium Fluoride', J. Phys. C Solid State Phys., vol. 7, pp. 445–453, (1973).
- [67] A. S. Quist, J. B. Bates, et al., 'Raman spectra of tetrafluoroberyllate ion in molten sodium fluoride and lithium fluoride to 686 C', J. Phys. Chem., vol. 76, no. 1, pp. 78–83, (1972).

- [68] L. M. Toth, J. Bates, et al., 'Raman Spectra of Be<sub>2</sub>F<sub>7</sub><sup>3-</sup> and Higher Polymers of Beryllium Fluorides in the Crystalline and Molten State', J. Phys. Chem., vol. 77, no. 2, pp. 216–221, (1973).
- [69] A. J. Barker, 'A compact, windowless reflectance furnace for infrared studies of corrosive melts', J. Phys. E., vol. 6, no. 3, pp. 241–244, (1973).
- [70] I. B. Polovov, V. A. Volkovich, et al., 'Chemistry of Vanadium Chlorides in Molten Salts: An Electronic Absorption Spectroscopy Study', J. Mol. Liq., vol. 103–104, pp. 387–394, (2003).
- [71] Z. Y. Zhang, M. F. Modest, et al., 'Measurement of infrared absorption coefficients of molten glasses', Exp. Heat Transf., vol. 14, no. 3, pp. 145–156, (2001).
- [72] J. K. Wilmshurst and S. Senderoff, 'Vibrational spectra of inorganic molecules. II. Infrared reflection spectra of liquid lithium, sodium, potassium, and silver nitrates', J. Chem. Phys., vol. 35, no. 3, pp. 1078–1084, (1961).
- [73] J. K. Wilmshurst, 'Infrared Spectra of Highly Associated Liquids and the Question of Complex Ions in Fused Salts', J. Chem. Phys., vol. 39, no. 7, pp. 1779–1788, (1963).
- [74] J. K. Wilmshurst, 'Infrared spectra of molten salts', J. Chem. Phys., vol. 39, no. 10, pp. 2545–2548, (1963).
- [75] J. S. Fordyce and R. L. Baum, 'Infrared-Reflection Spectra of Molten Fluoride Solutions: Tantalum (V) in Alkali Fluorides', J. Chem. Phys., vol. 44, no. 3, pp. 1159–1165, (1966).
- [76] J. S. Fordyce and R. L. Baum, 'Infrared-Reflection Spectra of Molten Fluoride Solutions: Nb (V) in KF:LiF', J. Chem. Phys., vol. 44, no. 3, p. 1159, (1966).
- [77] J. S. Fordyce and R. L. Baum, 'Infrared reflection spectra of molten fluoride solutions. Hydrolysis of tantalum (V) in potassium fluoride-lithium fluoride', J. Phys. Chem., vol. 69, no. 12, pp. 4335–4337, (1965).
- [78] A. J. Barker, 'Effect of Melting on Multiphonon Infrared-Absorption Spectra of KBr, NaCl and LiF', J. Phys. Part C Solid State Phys., vol. 5, no. 16, pp. 2276–2282, (1972).
- [79] D. G. Mead and G. R. Wilkinson, 'Far Infrared Emission of Alkali Halide Crystals and Melts', Proc. R. Soc. Lond. A. Math. Phys. Sci., vol. 354, no. 1678, pp. 349–366, (1977).
- [80] A. A. Khokhryakov, A. S. Paivin, et al., 'Spectral-analytical system for recording the electronic spectra of high-temperature melts and its technical frontier', Russ. Metall., vol. 2014, no. 2, pp. 166–171, (2014).
- [81] A. A. Khokhryakov and A. M. Khokhlova, 'Electronic absorption spectra of the Ce<sup>3+</sup> ions in halide melts', Radiochemistry, vol. 45, no. 6, pp. 559–561, (2003).
- [82] A. A. Khokhryakov, A. O. Vershinin, et al., 'Electronic spectra of praseodymium trifluoride solutions in molten alkali metal fluorides', Russ. J. Inorg. Chem., vol. 60, no. 12, pp. 1573–1577, (2015).

- [83] A. A. Khokhryakov, A. S. Paivin, et al., 'Optical Spectra of Gadolinium(III) Ions in Melts of Alkali Metal Fluorides', Russ. J. Inorg. Chem., vol. 64, no. 6, pp. 798–800, (2019).
- [84] A. A. Khokhryakov, 'Reflection absorption electron spectroscopy of high temperature melts', Rasplavy, vol. 4, pp. 84–88, (1994).
- [85] C. Yao, H. Mei, et al., 'Correcting thermal-emission-induced detector saturation in infrared spectroscopy', arXiv:2012.14987 [physics.optics], (2021).
- [86] C. P. Coyle, 'Advancing Radiative Heat Transfer Modeling in High-Temperature Liquid Salts', Massachusetts Institute of Technology, (2020).
- [87] M. C. C. Ribeiro, 'Chemla effect in molten LiCl/KCl and LiF/KF mixtures', J. Phys. Chem. B, vol. 107, no. 18, pp. 4392–4402, (2003).
- [88] N. Winner, H. Williams, et al., 'Ab-initio simulation studies of chromium solvation in molten fluoride salts', J. Mol. Liq., vol. 335, p. 116351, (2021).
- [89] M. Salanne, C. Simon, et al., 'A first-principles description of liquid BeF<sub>2</sub> and its mixtures with LiF: 2. Network formation in LiF-BeF<sub>2</sub>', J. Phys. Chem. B, vol. 110, no. 23, pp. 11461–11467, (2006).
- [90] C. F. Baes, 'A polymer model for BeF<sub>2</sub> and SiO<sub>2</sub> melts', J. Solid State Chem., vol. 1, no. 2, pp. 159–169, (1970).
- [91] V. Dracopoulos and G. N. Papatheodorou, 'Isotropic and anisotropic Raman scattering from molten alkali-metal fluorides', Phys. Chem. Chem. Phys., vol. 2, no. 9, pp. 2021–2025, (2000).
- [92] M. Salanne, C. Simon, et al., 'Intermediate range chemical ordering of cations in simple molten alkali halides', J. Phys. Condens. Matter, vol. 20, p. 332101, (2008).
- [93] V. Sarou-Kanian, A. L. Rollet, et al., 'Diffusion coefficients and local structure in basic molten fluorides: in situ NMR measurements and molecular dynamics simulations', Phys. Chem. Chem. Phys., vol. 11, no. 48, pp. 11501–11506, (2009).
- [94] H. O. Nam and D. Morgan, 'Redox condition in molten salts and solute behavior: A first-principles molecular dynamics study', J. Nucl. Mater., vol. 465, pp. 224–235, (2015).
- [95] K. Igarashi, Y. Okamoto, et al., 'X-ray diffraction study of molten eutectic LiF-NaF-KF mixture', J. Chem. Soc. Faraday Trans. 1 Phys. Chem. Condens. Phases, vol. 84, no. 12, pp. 4407–4415, (1988).
- [96] B. A. Frandsen, S. D. Nickerson, et al., 'The structure of molten FLiNaK', J. Nucl. Mater., vol. 537, p. 152219, (2020).
- [97] O. Pauvert, D. Zanghi, et al., 'In situ experimental evidence for a nonmonotonous structural evolution with composition in the molten LiF-ZrF<sub>4</sub> system', J. Phys. Chem. B, vol. 114, no. 19, pp. 6472–6479, (2010).

- [98] H. O. Nam, A. Bengtson, et al., 'First-principles molecular dynamics modeling of the molten fluoride salt with Cr solute', J. Nucl. Mater., vol. 449, no. 1–3, pp. 148–157, (2014).
- [99] F. Vaslow and A. H. Narten, 'Diffraction pattern and structure of molten BeF<sub>2</sub>-LiF solutions', J. Chem. Phys., vol. 59, no. 9, pp. 4949–4954, (1973).
- [100] Y. Y. Kharitonov and Y. A. Buslaev, 'Infrared Absorption Spectra of Oxyfluorides of some Metals of the Fourth and Fifth Groups of the Periodic Table', Izv. Akad. Nauk SSSR, Otd. Khim. Nauk, vol. 3, pp. 393–401, (1962).
- [101] A. F. Vik, V. Dracopoulos, et al., 'Solubility and Raman spectra of Ta(v) in LiF-NaF-KF-Na<sub>2</sub>O melts', J. Chem. Soc. Dalt. Trans., no. 14, pp. 2164–2172, (2001).
- [102] X. Liu, B. Wang, et al., 'Raman spectroscopic and theoretical studies on the structure of Ta (V) fluoro and oxofluoro complexes in molten FLiNaK', J. Mol. Liq., vol. 337, p. 116409, (2021).
- [103] J. H. Von Barner, E. Christensen, et al., 'Vibrational spectra of niobium(V) fluoro and oxo fluoro complexes formed in alkali-metal fluoride melts', Inorg. Chem., vol. 30, no. 3, pp. 561–566, (1991).
- [104] D. M. Gruen and R. L. McBeth, 'The coordination chemistry of 3d transition metal ions in fused salt solutions', Pure Appl. Chem., vol. 6, no. 1, pp. 23–48, (1963).
- [105] H. Ai, Y. Liu, et al., 'Dissolved valence state of iron fluorides and their effect on Ni-based alloy in FLiNaK salt', Corros. Sci., vol. 192, no. August, p. 109794, (2021).
- [106] Y. Tanabe and S. Sugano, 'On the Absorption Spectra of Complex Ions. I', J. Phys. Soc. Japan, vol. 9, no. 5, pp. 753–766, (1954).
- [107] Y. Tanabe and S. Sugano, 'On the Absorption Spectra of Complex Ions II', J. Phys. Soc. Japan, vol. 9, no. 5, pp. 766–779, (1954).
- [108] J. R. Keiser, 'Status of Tellurium-Hastelloy N Studies in Molten Fluoride Salts', Tech. Rep. ORNL/TM-6002, (1977).
- [109] V. Dracopoulos, B. Gilbert, et al., 'Vibrational modes and structure of lanthanide fluoride potassium fluoride binary melts LnF<sub>3</sub>-KF (Ln = La, Ce, Nd, Sm, Dy, Yb)', J. Chem. Soc., Farady Trans., vol. 94, no. 17, pp. 2601–2604, (1998).
- [110] V. Dracopoulos, B. Gilbert, et al., 'Vibrational modes and structure of rare earth halide alkali halide binary melts YBr<sub>3</sub>-ABr (A = Li, K, Cs) and YF<sub>3</sub>-KF', J. Chem. Soc., Farady Trans., vol. 93, no. 17, pp. 3081–3088, (1997).
- [111] G. M. Photiadis, B. Borresen, et al., 'Vibrational modes and structures of lanthanide halide alkali halide binary melts LnBr<sub>3</sub>-KBr (Ln = La, Nd, Gd) and NdCl<sub>3</sub>-ACl (A = Li, Na, K, Cs)', J. Chem. Soc., Farady Trans., vol. 94, no. 17, pp. 2605–2613, (1998).
- [112] G. N. Papatheodorou, 'Raman spectroscopic studies of yttrium (III) chloride–alkali metal chloride melts and of Cs<sub>2</sub>NaYCl<sub>6</sub>6 and YCl<sub>3</sub> solid compounds', J. Chem. Phys., vol. 66, no. 7, pp. 2893–

- 2900, (1977).
- [113] A. L. Rollet, S. Godier, et al., 'High temperature NMR study of the local structure of molten LaF<sub>3</sub>-AF (A = Li, Na, K and Rb) mixtures', Phys. Chem. Chem. Phys., vol. 10, no. 22, pp. 3222–3228, (2008).
- [114] R. Cui and C. Wang, 'In situ high temperature Raman and DFT analysis of cerium fluoride and oxyfluoride structures in molten FLiNaK', J. Raman Spectrosc., vol. 52, no. 6, pp. 1148–1154, (2021).
- [115] X. Liu, Y. Li, et al., 'Raman and density functional theory studies of lutecium fluoride and oxyfluoride structures in molten FLiNaK', Spectrochim. Acta Part A Mol. Biomol. Spectrosc., vol. 251, p. 119435, (2021).
- [116] L. B. Asprey, F. H. Kruse, et al., 'Alkali Fluoride Complexes of Tetravalent Protactinium', Inorg. Chem., vol. 6, no. 3, pp. 544–548, (1967).
- [117] D. Cohen and W. T. Carnall, 'Absorption spectra of uranium(III) and uranium(IV) in DClO<sub>4</sub> solution', J. Phys. Chem., vol. 64, no. 12, pp. 1933–1936, (1960).
- [118] C. K. Jorgensen, 'Absorption Spectra of Red Uranium (III) Chloro Complexes in Strong Hydrochloric Acid', Acta Chem Scand, vol. 10, no. 9, pp. 1503–15005, (1956).
- [119] C. Bessada, D. Zanghi, et al., 'Investigation of ionic local structure in molten salt fast reactor LiF-ThF<sub>4</sub>-UF<sub>4</sub> fuel by EXAFS experiments and molecular dynamics simulations', J. Mol. Liq., vol. 307, p. 112927, (2020).
- [120] J. A. Ocádiz-Flores, A. E. Gheribi, et al., 'Examination of the short-range structure of molten salts: ThF<sub>4</sub>, UF<sub>4</sub>, and related alkali actinide fluoride systems', Phys. Chem. Chem. Phys., vol. 23, no. 18, pp. 11091–11103, (2021).
- [121] B. Gilbert and T. Materne, 'Reinvestigation of Molten Fluoroaluminate Raman Spectra: The Question of the Existence of AlF<sub>5</sub><sup>2</sup>- Ions', Appl. Spectrosc., vol. 44, no. 2, pp. 299–305, (1990).
- [122] C. T. Ewing, J. R. Spann, et al., 'Radiant Transfer of Heat in Molten Inorganic Compounds at High Temperatures', J. Chem. Eng. Data, vol. 7, no. 2, pp. 246–250, (1962).
- [123] E. S. Chaleff, N. Antolin, et al., 'Ab-Initio Calculation of Spectral Absorption Coefficients in Molten Fluoride Salts with Metal Impurities', Nucl. Technol., vol. 204, no. 1, pp. 59–65, (2018).
- [124] H. H. Li, 'The Infrared Absorption Coefficient of Alkali Halides', Int. J. Thermophys., vol. 1, no. 1, pp. 97–134, (1980).
- [125] R. P. Lowndes and D. H. Martin, 'Dielectric dispersion and the structures of ionic lattices', Proc. R. Soc. London. Ser. A. Math. Phys. Sci., vol. 308, no. 1495, pp. 473–496, (1969).
- [126] M. Tetreault-Friend, L. A. Gray, et al., 'Optical properties of high temperature molten salt mixtures for volumetrically absorbing solar thermal receiver applications', Sol. Energy, vol. 153, pp. 238–

- 248, (2017).
- [127] C. A. Schroll, A. M. Lines, et al., 'Absorption spectroscopy for the quantitative prediction of lanthanide concentrations in the 3LiCl-2CsCl eutectic at 723 K', Anal. Methods, vol. 8, no. 43, pp. 7731–7738, (2016).
- [128] A. J. Bruce and J. A. Duffy, 'Ultraviolet spectra of Tl<sup>+</sup>, Pb<sup>2+</sup>, and Bi<sup>3+</sup> probe ions in molten fluoride media', J. Chem. Soc. Faraday Trans. 1 Phys. Chem. Condens. Phases, vol. 78, no. 3, pp. 907–914, (1982).